TRANSIENT MODELING TECHNIQUES FOR THE ANALYSIS OF ELECTROMAGNETIC LAUNCHERS

A THESIS SUBMITTED TO
THE GRADUATE SCHOOL OF NATURAL AND APPLIED SCIENCES
OF
MIDDLE EAST TECHNICAL UNIVERSITY

BY

NAIL TOSUN

IN PARTIAL FULFILLMENT OF THE REQUIREMENTS
FOR
THE DEGREE OF MASTER OF SCIENCE
IN
ELECTRICAL AND ELECTRONICS ENGINEERING

SEPTEMBER 2021

Approval of the thesis:

TRANSIENT MODELING TECHNIQUES FOR THE ANALYSIS OF ELECTROMAGNETIC LAUNCHERS

submitted by **NAIL TOSUN** in partial fulfillment of the requirements for the degree of **Master of Science in Electrical and Electronics Engineering Department, Middle East Technical University** by,

Prof. Dr. Halil Kalıpçılar
Dean, Graduate School of **Natural and Applied Sciences** _____

Prof. Dr. İlkay Ulusoy
Head of Department, **Electrical and Electronics Engineering** _____

Assoc. Prof. Dr. Ozan Keysan
Supervisor, **Electrical and Electronics Engineering Dept., METU** _____

Examining Committee Members:

Assist. Prof. Dr. Emine Bostancı Özkan
Electrical and Electronics Engineering Dept., METU _____

Assoc. Prof. Dr. Ozan Keysan
Electrical and Electronics Engineering Dept., METU _____

Prof. Dr. Muammer Ermiş
Electrical and Electronics Engineering Dept., METU _____

Assist. Prof. Dr. Ahmet Cemal Durgun
Electrical and Electronics Engineering Dept., METU _____

Prof. Dr. Timur Aydemir
Electrical and Electronics Engineering Dept., Kadir Has University _____

Date: _____

I hereby declare that all information in this document has been obtained and presented in accordance with academic rules and ethical conduct. I also declare that, as required by these rules and conduct, I have fully cited and referenced all material and results that are not original to this work.

Name, Last Name: NAIL TOSUN

Signature :

ABSTRACT

TRANSIENT MODELING TECHNIQUES FOR THE ANALYSIS OF ELECTROMAGNETIC LAUNCHERS

Tosun, Nail
M.S., Department of Electrical and Electronics Engineering
Supervisor : Assoc. Prof. Dr. Ozan Keysan

September 2021, 119 pages

Although electromagnetic launchers (EMLs) are better than gun-powder-based launchers, they have to endure severe electrical and mechanical conditions. Therefore, the optimal design and accurate simulations of these devices are essential. The inductance and electromotive force (EMF) variations in the transient, which significantly impact the launch process, are modeled. Moreover, velocity skin effect (VSE) is added to the EML calculations in an effective way. Commercial finite element software cannot solve the electromagnetic aspects of such a high-speed application with a transient solver in 3-D. Although 2-D approximations can be used, such an approximation overestimates VSE resistance due to geometry simplifications. In this thesis, a novel quasi-transient 3-D Finite Element Method (FEM) model where the air-armature region's conductivity is varied to emulate the high-speed motion of the armature is proposed. These propositions are compared for experimental results with different EMLs, EMFY-1, and EMFY-2 and showed good agreement.

Keywords: Electromagnetic launchers, electromotive force, finite element method, pulse power supplies, transient inductance, velocity skin effect.

ÖZ

ELEKTROMANYETİK FIRLATICILARININ GEÇİÇİ ETKİLERİNİ MODELLEME TEKNİKLERİ

Tosun, Nail
Yüksek Lisans, Elektrik ve Elektronik Mühendisliği Bölümü
Tez Yöneticisi : Doç. Dr. Ozan Keysan

Eylül 2021 , 119 sayfa

Elektromanyetik fırlatıcılar, barut tabanlı fırlatıcılardan daha iyi olsalar da, ağır elektriksel ve mekanik koşullara dayanmaları gerekir. Bu nedenle, bu cihazların optimum tasarımı ve doğru simülasyonları çok önemlidir. Atış sürecini önemli ölçüde etkileyen geçici olaydaki endüktans ve elektromotor kuvvet (EMF) varyasyonları modellenmiştir. Ayrıca, bu hesaplamalarına etkili bir şekilde hız deri etkisi (HDE) eklenmiştir. Ticari sonlu eleman yazılımı, bu kadar yüksek hızlı bir uygulamanın elektromanyetik yönlerini 3 boyutlu olarak bir geçici çözücü ile çözemez. 2-D yaklaşımları kullanılabilmesine rağmen, böyle bir yaklaşım, geometri basitleştirmelerinden dolayı, VSE direncini olduğundan fazla tahmin etmektedir. Bu tezde, armatürün yüksek hızlı hareketini taklit etmek için hava-armatür bölgesinin iletkenliğinin değiştirildiği yeni bir yarı-geçici 3-D Sonlu Eleman Yöntemi (SEY) modeli önerilmiştir. Bu model, farklı elektromanyetik fırlatıcılarla, EMFY-1 ve EMFY-2 ile, deneysel sonuçlar karşılaştırıldı ve iyi bir uyum gösterdiği görüldü.

Anahtar Kelimeler: Elektromanyetik fırlatıcılar, elektrik hareket gücü, geçici endüktans, sonlu eleman analizi, darbe güç kaynakları, hız deri etkisi.

Definitely, not for Goethe.

ACKNOWLEDGMENTS

Throughout the writing of this dissertation, I have received a great deal of support and assistance.

First, and most of all, I would like to convey my gratefulness to Assist. Prof. Dr. Ozan Keysan for providing me an opportunity to complete this study. Without his expertise, support, supervision, and motivation, this thesis would not have been possible. You provided me with the tools that I needed to choose the right direction and successfully complete my dissertation. I feel fortunate to be one of his graduate students and a part of his research group called METU Power Lab. I will carry these memories, and learnings throughout my academic life.

I want to extend my sincere appreciation to ASELSAN Inc. for its precious support throughout my graduate studies. I would like to give special thanks to Mustafa Karagöz, Dr. Baran Yıldırım, and Ferhat Yurdakonar, who helped me a lot during this project.

I wish to express my deepest gratitude Enes Ayaz, who provided stimulating discussions as well as happy (and long) distractions to rest my mind outside of my research. I will remember each theory we made about every details of the universe.

I would like to acknowledge my co-authors from METU Power Lab, Hakan Polat, Doğa Ceylan, and Enes Ayaz (again!), for their wonderful collaboration.

I would like to pay my special regards to Nadir Meral who has great influence on my career choice. Moreover, I also want to thank all the negativity around me. Without them, I can not have the desire to finish this thesis.

I am thankful to TUBİTAK, the Scientific and Technological Research Council of Turkey, for granting me their M.S. studies scholarship, BİDEB 2210.

To my parents and my siblings: I am forever grateful for your patience and understanding. I would like to thank them for their wise guidance and loving ear. You are always there for me.

TABLE OF CONTENTS

ABSTRACT v

ÖZ vi

ACKNOWLEDGMENTS viii

TABLE OF CONTENTS ix

LIST OF TABLES xiii

LIST OF FIGURES xiv

LIST OF ABBREVIATIONS xx

CHAPTERS

1 INTRODUCTION TO ELECTROMAGNETIC LAUNCHERS 1

1.1 Working Principles 3

1.2 History of Electromagnetic Launchers 6

1.2.1 Early Attempts 6

1.2.2 TUFAN 9

1.3 Research Goals and Objectives 11

2 MODELING STRATEGIES AND GOVERNING EQUATIONS . . . 15

2.1 Modeling Strategies 15

2.1.1 Inductance Gradient 15
2.1.2 Kine-mechanical Equations 17
2.1.3 Analytical Calculations 19
2.1.3.1 Kerrisk's Formula 19
2.1.3.2 Löffler Formula 24
2.2 Governing Equations and Limitations 27
2.2.1 Boundary and Symmetry Conditions 28
2.2.2 Limitations with 3-D FEM formulations 31
2.2.3 The 2-D Formulation 33
2.2.3.1 Out-of-plane Vector Potential 34
2.2.3.2 In-plane Vector Potential 34
2.2.3.3 Three-component Vector Potential . . 35
2.3 Conclusion 36
3 VELOCITY SKIN EFFECT MODELLING USING 2-D TRANSIENT AND 3D QUASI-TRANSIENT FINITE ELEMENT METHODS . . . 39
3.1 Models 42
3.1.1 2-D Transient FEM 42
3.1.2 2-D Quasi-Transient FEM 45
3.1.3 3-D Quasi-Transient FEM 45
3.1.4 3-D Hybrid FEM 49
3.2 Methodology of the conducted work 53
3.2.1 Analysis 53

3.2.2 Validation 54

3.3 Results 54

3.4 Conclusion 56

4 TRANSIENT INDUCTANCE AND BACK-EMF CALCULATIONS OF ELECTROMAGNETIC LAUNCHERS 61

4.1 EMF calculation 62

4.2 Velocity skin effect modeling, R_{vse} 71

4.3 Results 73

4.4 Conclusion 79

5 TRIGGERING TIME OPTIMIZATION OF PULSE POWER SUPPLIES 81

5.1 Triggering time determination 84

5.1.1 Optimizing the Triggering Times to Obtain the Maximum Muzzle Velocity 84

5.1.2 Optimizing the Triggering Times to Ensure Desired Muzzle Velocity 86

5.2 The Simulation Model 87

5.3 Multi-level Fast Triggering Time Algorithm (MFTTA) 92

5.3.1 Pulse Current Shape with Hysteresis Control (PCSHC) 93

5.3.2 Determination of the Required I_{ref} for Desired Exit Velocity 96

5.4 Results 98

5.5 Discussion 105

5.6 Conclusion 106

6 CONCLUSION 109

6.1 Summary of Contribution to Literature and Novelties 110

6.1.1 VSE calculations 110

6.1.2 Back-EMF calculations 110

6.1.3 Triggering Time Optimization 111

6.2 Practical Application Considerations 111

6.3 Possible Improvements 111

6.4 Comparison with Conventional Guns 112

6.5 Future Works 112

REFERENCES 115

APPENDICES

LIST OF TABLES

TABLES

Table 1.1 Some parameters of the EMFY launchers. 10

Table 1.2 Parameters of a 200 kJ capacitive-PPS [1]. 12

Table 2.1 Kerrisk formula's coefficients. 20

Table 3.1 Geometric Parameters of Launchers 42

Table 3.2 Properties of simulations models used. 43

Table 3.3 Parameters of EMFY-1 and EMFY-2 Experiments 55

Table 4.1 Parameters of EMFY-1 and EMFY-2 Experiments 74

Table 4.2 Error analysis[1] of Rail Current Waveform 78

Table 4.3 Some Critical Outputs of the EMFY-1 and EMFY-2 Experiments and Simulations with the control and proposed methods 78

Table 5.1 EML Design Parameters and Limitations. 84

Table 5.2 Literature Survey on Triggering Time Algorithms. 87

Table 5.3 The parameters of RCGA 100

Table 5.4 The parameters of PSO 101

Table 5.5 The Performance Comparison of the Methods 101

LIST OF FIGURES

FIGURES

Figure 1.5 Birkelands coilgun which is housed in Norwegian Technical Museum.[2] 7

Figure 1.6 Kennys 100-Mile Electromagnetic Gun [3]. 8

Figure 1.7 Fauchon-Villeplees rail-mounted railgun [3]. 8

Figure 1.8 EMFY-2 Launcher 9

Figure 1.9 EMFY-2 Launcher Lab. view 10

Figure 1.10 Launch package for 50 mm x 50 mm square bore EMFY-2 launcher. 11

Figure 1.11 The capacitive-based PPS module model. 12

Figure 2.1 Geometric parameters of the EML. 20

Figure 2.2 L' values respect to various rail separations and rail heights. w = 0.02 m (left), w = 0.04 m (right). 21

Figure 2.3 L' values respect to various rail separations and rail heights. w = 0.06 m (left), w = 0.08 m (right). 22

Figure 2.4 L' values respect to various rail separations and rail heights. w = 0.10 m (left), w = 0.12 m (right). 22

Figure 2.5 The effect of the increase in rail separation on field distributions. Black vectors represent magnetic field density. h = 0.05 m, w = 0.03 m, s = 0.05 m (left), s = 0.075 m (right) 23

Figure 2.6 The effect of the increase in rail separation on field distributions. Black vectors represent magnetic field density. s = 0.05 m, w = 0.03 m, h = 0.05 m (left), h = 0.09 m (right) 23

Figure 2.7 The effect of the increase in rail separation on field distributions. Black vectors represent magnetic field density. s = 0.05 m, h = 0.05 m, w = 0.03 m (left), w = 0.05 m (right) 24

Figure 2.8 The intensity of the magnetic field around a conductor (left), the force between conductors dispersing current in the same direction. (right) . 24

Figure 2.9 Geometric parameters used in the Löffler formula. 25

Figure 2.10 Rail pressure with respect to rail separation and rail height. $I_r = 0.5MA$ (left), $I_r = 1MA$ (right). 26

Figure 2.11 Rail pressure with respect to rail separation and rail height. $I_r = 1.5MA$ (left), $I_r = 2MA$ (right). 26

Figure 2.12 Boundary conditions that have symmetry feature. 29

Figure 2.13 Boundary conditions that have symmetry feature. 30

Figure 2.14 Boundary conditions that have symmetry feature. 30

Figure 2.15 3-D geometry of the model. 31

Figure 2.16 3-D geometry of the model. 31

Figure 2.17 2-D symmetry plane where out-of-plane vector potential usage is useful. 34

Figure 2.18 The current distribution in the rails and magnetic field density vectors in 2-D. The Rail current is 1.5 MA DC. 35

Figure 2.19 2-D symmetry plane where in-plane vector potential usage is useful. 36

Figure 3.1 2-D transient FEM results with stationary and moving armature. Colours represent the current density distribution, and it has unit $\frac{A}{m^2}$. . . . 40

Figure 3.2 2-D transient model geometry 44

Figure 3.3 Computational regions 44

Figure 3.4 The armature's time-position dependent electrical conductivity function. 46

Figure 3.5 Mesh structures of the simulation models. 47

Figure 3.6 Comparisons of 2-D Q-T model and 2-D transient model in terms of rail current density distribution at $v = 500$ m/s, $v = 1000$ m/s and $v = 2000$ m/s. Mean absolute error is utilized for error calculations. 48

Figure 3.7 The current density distribution in the middle surface of the rail when the armature has 1200 m/s speed. The color legend is for the current density only and its unit is $\mathrm{A/m^2}$. 49

Figure 3.8 Current density distribution in rails with various rail cross-sections. The color legend is for the current density only and its unit is $\mathrm{A/m^2}$. Small letters represent the cross-section points demonstrated in Fig. 3.7. 50

Figure 3.9 Hybrid FEM model used to simulate EMLs. 51

Figure 3.10 The current density distribution ($\mathrm{A/m^2}$) in rail 3-D Q-T simulation (left) and static armature simulation (right). The Q-T analysis is made with an armature which has 1000 m/s velocity. 51

Figure 3.11 The methodology used to investigate the accuracy of 2-D approximation on VSE resistance. 53

Figure 3.12 2-D transient simulation results for VSE resistance with respect to armature position graph for armature velocities from 100 m/s to 1000 m/s. 55

Figure 3.13 3-D Q-T simulation results for VSE resistance with respect to armature position graph for armature velocities from 300 m/s to 2300 m/s. 56

Figure 3.14 Simulation and experimental results for the rail current of the experiment-A with EMFY-1 57

Figure 3.15 Simulation and experimental results for the rail current of the experiment-B with EMFY-1 57

Figure 3.16 Simulation and experimental results for the rail current of the experiment-C with EMFY-2 58

Figure 3.17 Simulation and experimental results for the rail current of the experiment-D with EMFY-2 58

Figure 3.18 The circuit schematic of the last stage of the launch. Disconnected units are demonstrated using gray color. $\mathrm{R_{PPC}}$ and $\mathrm{L_{PPC}}$ represent the PPS resistance and inductance, respectively. $\mathrm{R_c}$ and $\mathrm{L_c}$ represent cable resistances and inductances. 59

Figure 3.19 The current density distribution ($\mathrm{A/m^2}$) in the rail with 3-D Q-T model. The armature modelled as rectangular prism. 60

Figure 4.1 The geometry which is used for 3D FEM analysis of EMFY-2. Half symmetry is used for all FEM simulations. The integration boundary for $\mathrm{L_{ext}}$ is demonstrated. However, the armature is modeled as whole for visual purposes. 62

Figure 4.3 Coil deformation analogy. Transition from highly transient rail current to DC state can be considered as lateral deformation of a coil. Changing in the rail current path creates a transient inductance change which is also a source of EMF. The color legend is for the current density only and its unit is $\mathrm{A/m^2}$. 65

Figure 4.4 Comparisons of the two calculation methods of EMF resistance on EMFY-1 (a) and EMFY-2 (b). Spikes at the EMF resistance where transient rail inductance included comes from the discrete derivative operator in (4.12). 66

Figure 4.5 The comparison of L_{int}. EMFY-2 simulation model used in this calculations. Difference between two model increases especially at the down-slope rail current region. 68

Figure 4.6 Rail current distribution and magnetic flux density vectors throughout the launch. The color legend is for the current density only and its unit is $\mathrm{A/m^2}$. The rail current waveform is demonstrated in Fig. 4.5. a) 0.5 ms, b) 1.5 ms and c) 4.75 ms 70

Figure 4.7 Definitions of the interior and exterior boundaries, outer air domains and the symmetry axis. The color legend is for the current density only and its unit is $\mathrm{A/m^2}$. There is a significant amount magnetic flux density around the outer air domain which is taken into account when the inductance are calculated. 71

Figure 4.8 Comparison of L'_{ext} calculation methods. Control method found inductance gradient $\%12$ higher since the domain includes armature rail interaction region. Integration boundaries which are used in the control method and the proposed method can be seen in Fig. 4.2 and Fig. 4.9 respectively. 72

Figure 4.9 The new integration boundary for lumped inductance calculations. 72

Figure 4.10 Simulated and experimental rail currents of the experiment-A. EMFY-1 launcher is used in this experiment. 74

Figure 4.11 Simulated and experimental rail currents of the experiment-B. EMFY-1 launcher is used in this experiment. 75

Figure 4.12 Simulated and experimental rail currents of the experiment-C with EMFY-2 launcher. 76

Figure 4.13 Simulated and experimental rail currents of the experiment-D with EMFY-2 launcher. 77

Figure 5.1 The connection of pulse power supplies to EML. In this study 32 capacitive based PPS module connected parallel to EML. 82

Figure 5.2 Optimized pulse-shaped rail current, and non-optimized one. 82

Figure 5.5 Integration boundary and $\mathrm{x_o}$. 89

Figure 5.6 Concentrated coil approach, breech to muzzle cross-section. 91

Figure 5.7 Current excitation on the rails, resultant transient inductance gradients and non-optimized current waveform. 91

Figure 5.8 Pseudo-code of the algorithm. 93

Figure 5.9 PCSHC. The algorithm takes input as I_{ref} and give N amount triggering time which associated with a unique ν_{exit}. The algorithm spend $N - M$ circuit simulation time for all obtaining triggering times. 94

Figure 5.10 Intermediate results of the pulse current algorithm. The algorithm search for trigger time which is defined as moment that rail current decreased from I_{ref}. Then, it restart the simulation with a new triggering time, and search for next. While iterations continue, the rail current becomes pulse shape current with increasing width. 94

Figure 5.11 Peak current vs. number of modules triggered at t=0 ms. The dashed current lines exceeds the maximum current density in Table 5.1. . . 95

Figure 5.12 The results pulse current algorithm respect to different I_{ref}. N denoted as module number is taken 32. The capacitor voltage of the module are identical at 6500 V. 96

Figure 5.13 The results pulse current algorithm respect to different I_{ref}. N denoted as module number is taken 32. The capacitor voltage of the module are identical at 6500 V. 97

Figure 5.14 Exit velocity vs amplitude of pulse current graph at $V_c = 6500\ V$. This graph indicates that there exist a unique pulse shape current for all exit velocities. 98

Figure 5.15 Same steps of the golden search algorithm. 99

Figure 5.16 The performance of golden section line search algorithm. Noted that the golden section line search algorithm uses only one function evaluation at all iterations except the initial one. Considering that one function evaluation takes 10 to 18 circuit simulations, the proposed algorithm requires a few tens of iterations for 1% relative error and one or two hundred iterations for 0.1% relative error. 100

Figure 5.17 Individuals of each generation and their cost values with RCGA with constraints. The population size looks like decrease after generations due to maximum current constraint. 102

Figure 5.18 Individuals of each generation and their cost values with RCGA. No constraint applied. The purpose of this study is understanding of behaviour of system with respect to triggering times. After various iterations the maximum v_{exit} is 2723 m/s which corresponding to all triggering times are 0 s. However this result violate the maximum rail current constraint. . 103

Figure 5.19 Initial intermediate and final steps of RCGA without constraint. It showed that the firing sequence converged to zero vector (indicating that all PPS modules triggered initial time step). However, this condition violate the maximum rail current constraint 104

Figure 5.20 Initial intermediate and final steps of RCGA with constraint. The study showed that rail current becomes pulse current that have magnitude I_{max} to have maximum v_{exit} and maximum efficiency η. 105

Figure 5.21 The result of Particle Swarm Optimization. The result are consistent with RCGA 106

Figure 5.22 Variation of peak current and projectile to input power efficiency vs. projectile speed for different capacitor charge voltages. 107

LIST OF ABBREVIATIONS

2D-QT	2-D Quasi-Transient
2D-T	2-D Transient
3D-QT	3-D Quasi-Transient
AC	Alternating Current
DC	Direct Current
EMF	Electro-motive Force
EML	Electromagnetic Launcher
FEA	Finite Element Analysis
FEM	Finite Element Method
GA	Genetic Algorithm
IAT	Institute for Advanced Technology
IR	Improvement Ratio
MAE	Mean Absolute Error
MFTTA	Multi-level Fast Triggering Time Algorithm
PCSHC	Pulse Current Shape with Hysteresis Control
PPS	Pulse Power Supply
PSO	Particle Swarm Optimization
Q-T	Quasi-Transient
RCGA	Real-Coded Genetic Algorithm
RMSE	Root-Mean Squared Error
TTOP	Triggering Time Optimization Problem
VSE	Velocity Skin Effect

CHAPTER 1

INTRODUCTION TO ELECTROMAGNETIC LAUNCHERS

Electromagnetic launchers (EMLs) are electromechanical energy conversion devices that convert electrical energy into mechanical energy. Unlike rotational machines, i.e., induction motors and DC machines, energy conversion in the EML happens between electrical energy and linear mechanical energy. Rotational, and linear electromechanical energy conversion devices are illustrated in Fig. 1.1.

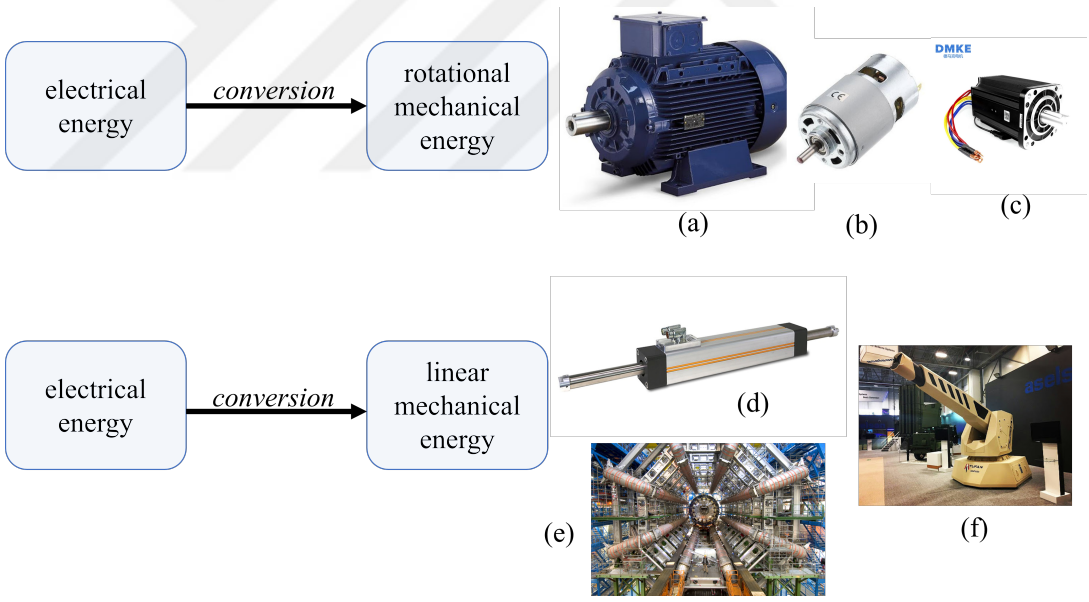

Figure 1.1: Rotational vs. linear electromechanical energy conversion devices. (a) Induction machine, (b) DC Motor, (c) BL-DC motor, (d) tubular linear motor, (e) particle accelerator, (f) railgun.

EMLs accelerate projectiles from several grams to kilograms to hypersonic velocities without any explosive chemicals. Gun-powdered launchers use stored chemical energy inside the material as a primary energy source. Explosion due to ignition cre-

ates excessive pressure inside the barrel, and that pressure accelerates the projectile. However, the generated force is peaky, meaning that it loses its magnitude through acceleration since the volume of the medium where the explosion happens increases while the projectile is moving. Thus, it can be considered as the acceleration is limited *theoretically*, since the linear increase in the gun-powder (so-called source) does not result in a linear rise in the projectile action. It has a diminishing return.

Moreover, excessive field gradients due to the ignition can generate stability issues; thus, the velocity control of the projectile is often challenging. EMLs have answers to such limitations. Firstly, the propulsive force is dependent only on the EML geometry and the excitation current. There is no diminishing return pattern; the propulsive force exists without any loss mechanism as long as the EML is excited. Therefore, they exceed the projectile's velocity limits (2-3 km/s). Two different acceleration curves regarding the excitation are shown in Fig. 1.2. The peaky acceleration is belonged to an explosive source, whereas the pulse-shaped acceleration belongs to the EML excitation. It should be noted that the pulse-width of the pulse acceleration can be further increased by adding a parallel electrical source, whereas there is no such an option in the peaky acceleration case.

Since the only limiting factor is the rail length and power sources' capabilities, their maximum projectile velocity is considered much more massive than in gun-powders-based. Although they are primarily considered for military purposes, some studies in the literature investigate the feasibility of space launcher for civil applications [4]. The first objective is accelerating microsatellite payloads (which have 1-10 kg mass) to 7 km/s [5]. Institute for Advanced Technology (IAT) achieve 7km/s velocities with 7 g projectile and addressed the challenges of the space-launch in 2007 [6]. Lehmann *et. al* examined the suborbital application and have confirmed that the EML seems feasible; it is based on todays knowledge, and the existing technology [7]. An artistic view of an EML system designed for suborbital applications is shown in Fig. 1.3.

Secondly, the propulsion mechanism is not explosive; fields are more stable, observable, and easier to control. Moreover, the propulsive force is applied along the entire armature volume and not only its base, which creates some mechanical advantages. The recoil during the launch is less than the conventional ones since no gun-powder

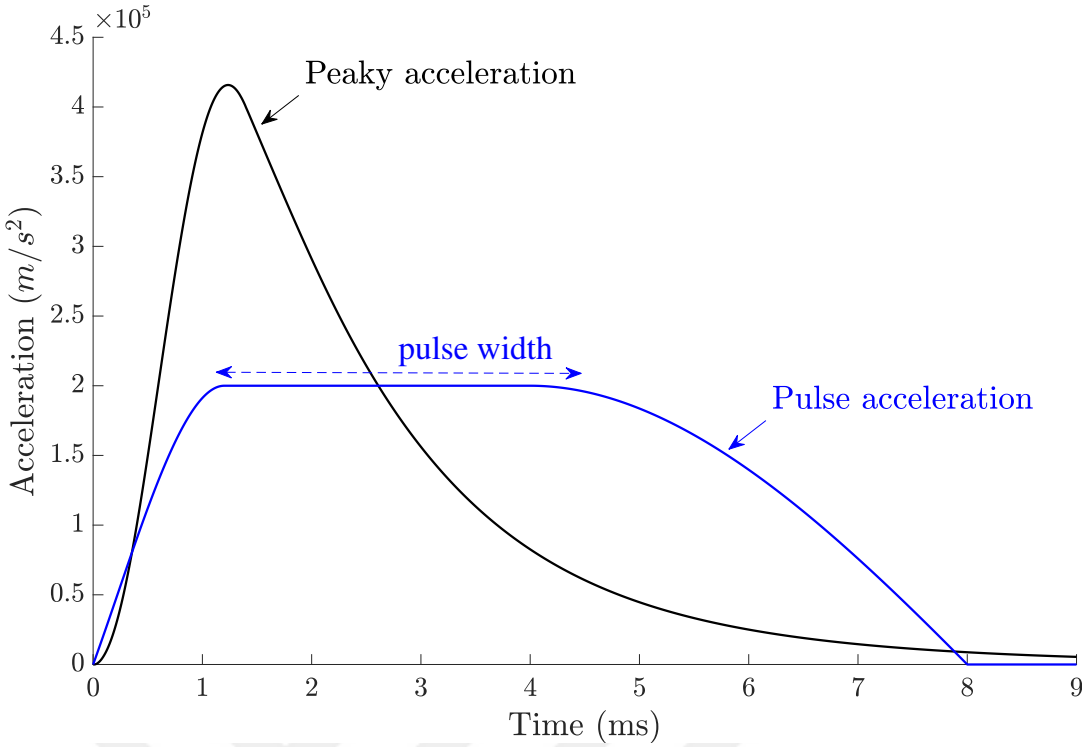

Figure 1.2: Two different acceleration curves.

gases are ejected.

Considering the advantages of the EML system over classical launchers, EMLs will be investigated through different applications, objectives, and fields such as electrical engineering, mechanical engineering, material science, aerodynamics, plasma science, etc. In this thesis, challenges are covered with electromagnetic computations. These difficulties can appear due to the nature of EML structure, simulation methods, or the degree of accuracy that is wanted to increase. All of them are discussed briefly. Experimental results built a basis to create a figure of merit between the modeling ideas. However, before going into the technical content about the thesis's main novelty, the working principles of the EML, and historical developments are introduced in this chapter.

1.1 Working Principles

Conventional EMLs have two conducting rails that are responsible for carrying large currents. Rails are mostly made of copper alloys (i.e. CuCr) considering high electri-

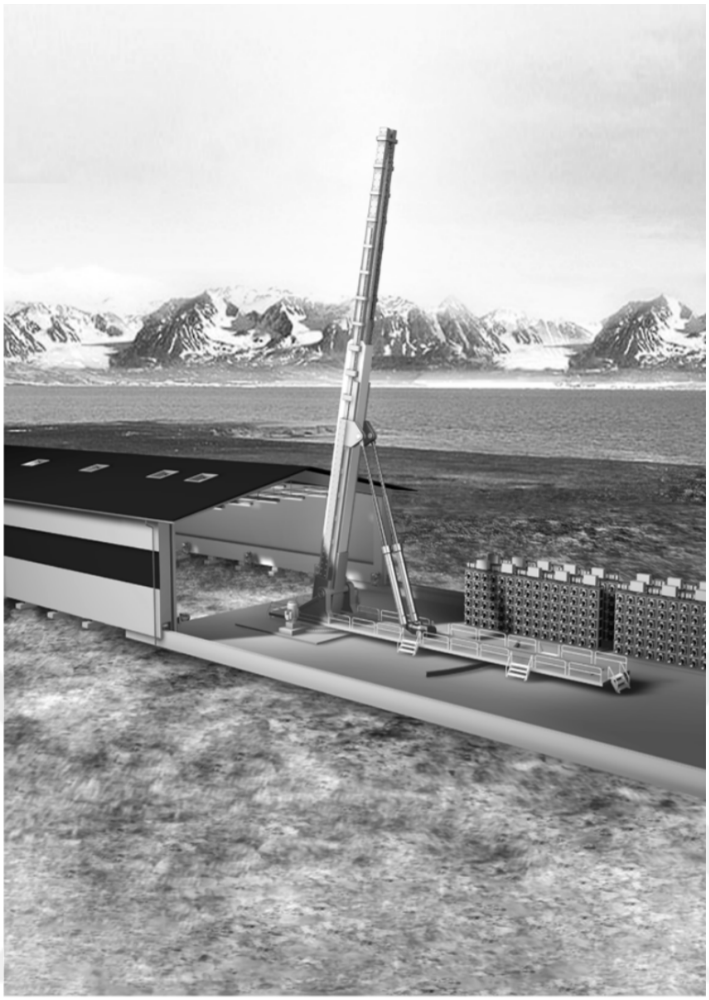

Figure 1.3: Artistic view of a EML system designed for suborbital applications. Figure taken from [7].

cal conductivity and mechanical performance under significant stresses, service life, and reliability [8]. An armature is required to ensure electrical connection between rails. As the electromechanical conversion occurs in this component, it is stated as the armature. Armature materials are aluminum alloys; primarily, their density is lower than other highly conductive metals. Since rails are short-circuited with the armature, the supplied current creates its magnetic field. In that sense, EMLs are self-excited electrical machines. Perpendicular components of the current density and the magnetic field make Lorentz force in the armature body. Lorentz force on the armature can be calculated using a volume integration as in the (1.1). In Fig. 1.4, magnetic field, current, and the thrust directions are illustrated. Moreover, the breech and muzzle sides of the rails are indicated with green and blue rectangles. Breech is the place

where the rails are connected to the PPS. On the other hand, muzzle is the opposite of the rails.

$$\vec{F} = \iiint_V \vec{J} \times \vec{B}\, dV \tag{1.1}$$

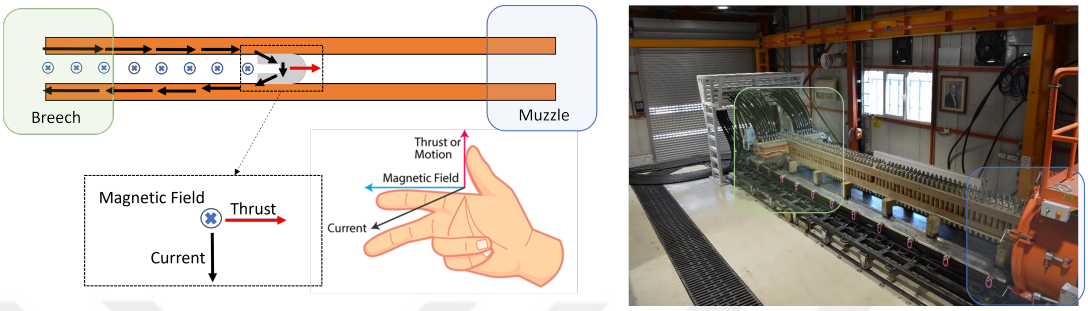

Figure 1.4: Current, magnetic field, and the thrust directions in the EML. Breech, and muzzle sides are also indicated.

According to the principle of virtual work, the related equation of energy balance is in (1.2), if the mechanical motion is in the z-direction[1] only;

$$dW_z = dW_s - dW_m - dW_f \tag{1.2}$$

where dW_z is the work done by Lorentz force, dW_s is the energy supplied by the circuit system; dW_m is the increase in the magnetic energy; dW_f is the energy leaves from field domain. As the Lorentz force, denoted as F_z creates the mechanical motion, it can be expressed as in (1.3).

$$F_z = \frac{dW_z}{dz} \tag{1.3}$$

Suppose that the electrical system does not supply energy to the magnetic field during virtual displacement, which implies $dW_s = 0$. If solution domain is inferior field then $dW_f = 0$ [9]. Then (1.3) becomes as in (1.4).

$$F_z = -\frac{dW_m}{dz} \tag{1.4}$$

[1] The z-direction is described as the direction where armature move.

W_m is the magnetic energy which originates from the inductance as in (1.5) where I is the rail current.

$$W_m = \frac{1}{2} L I^2 \tag{1.5}$$

Then, the Lorentz force becomes as in (1.6).

$$F_z = -\frac{1}{2} \frac{dL}{dz} I^2 \tag{1.6}$$

The $\frac{dL}{dz}$ term is called as the inductance gradient, or L', which is one of the important parameter for an EML. L' is closely related with EML's performance and efficiency.

1.2 History of Electromagnetic Launchers

In this section, an introduction to a brief history of EML is presented. Firstly, the early attempts from 20$^{\text{th}}$ century are given. Then, the three consequent generations of the ASELSAN's launchers (TUFAN) are presented.

1.2.1 Early Attempts

The history of the EML is considered 176 years old if the the advertisement that appeared in 1844 is to be believed [3].

"On Monday next, October 14, 1844, from 1 to 3 oclock, in the Cattle Market, Minden Place, Mr. Benningfield will exhibit his newly invented Electric Gun

SIVA, or THE DESTROYER,

with some striking improvements. (...)

Although there were some pretentious claims about SIVA in the advertisement, there is no scientific proposition about how this machine worked. Since it was not fulfill the promises, it did not replaced with conventional guns. The first scientific evidence came out by Dr. Charles G. Page, M.D., in 1845. Using the helical coils and the batteries, iron bars were accelerated to be projected forty to fifty feet. After that, the EML concept was reinvented through different times and countries. The first

efforts were started in Norway by Birkeland in 1901. He is the founder of the first EML company, Firearm Company. He made a small coilgun and represented it to Norwegian Academy in 1902. Then he made a larger coilgun to pitching the potential shareholders in Oslo in 1903 [10]. Birkeland's coilgun, illustrated in Fig. 1.5 is housed in Norwegian Technical Museum today. Building on Birkelands ideas, an American engineer Paul Kenny, created a concept for a long-range artillery gun shown in Fig. 1.6. Birkeland, the pioneer of research in Norway, is reviewed by Egeland [11]. More details about Birkeland's work can be examined those.

Figure 1.5: Birkelands coilgun which is housed in Norwegian Technical Museum.[2]

Then the subsequent significant spikes were made with French contribution during World War I. Fauchon-Villeplee was the invertor of the EML. The studies that were conducted so far were based on induction rather than the Lorentz force. Therefore, the armature was needed to create a medium for the current. Iron magnets created the magnetic field. With a 2-m-long railgun powered by a Gramme dynamo that produced 600 A at 60 V, he successfully launched 270-mm-long projectiles with fins of 70 mm that penetrated 80-mm-thick wooden targets at 25 m [10]. In 1918, he proposed a 128-MJ EML with a 30-meter length, almost 3.5 MA current excitation. The proposed model is illustrated in Fig. 1.7. These specifications are not met even

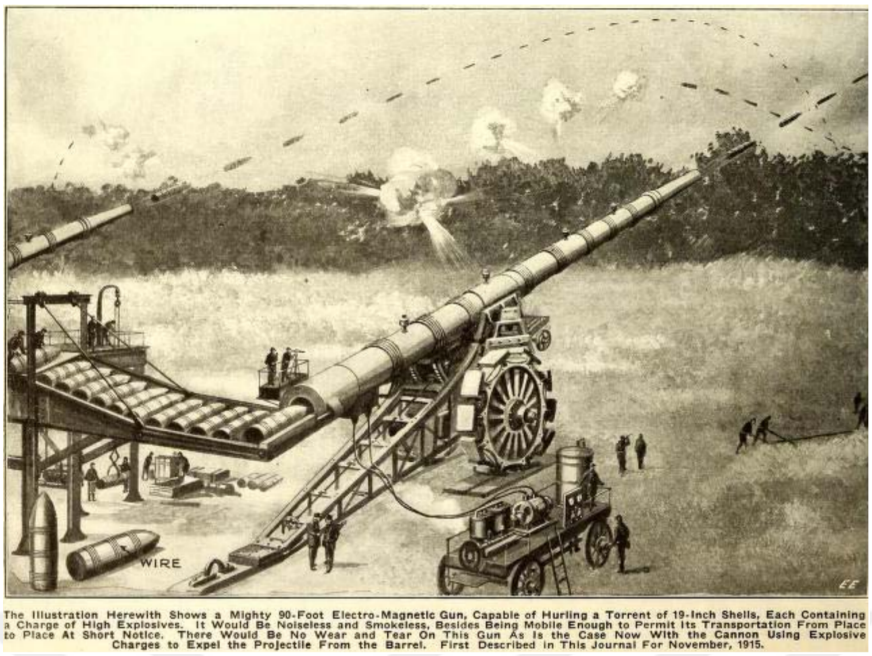

Figure 1.6: Kennys 100-Mile Electromagnetic Gun [3].

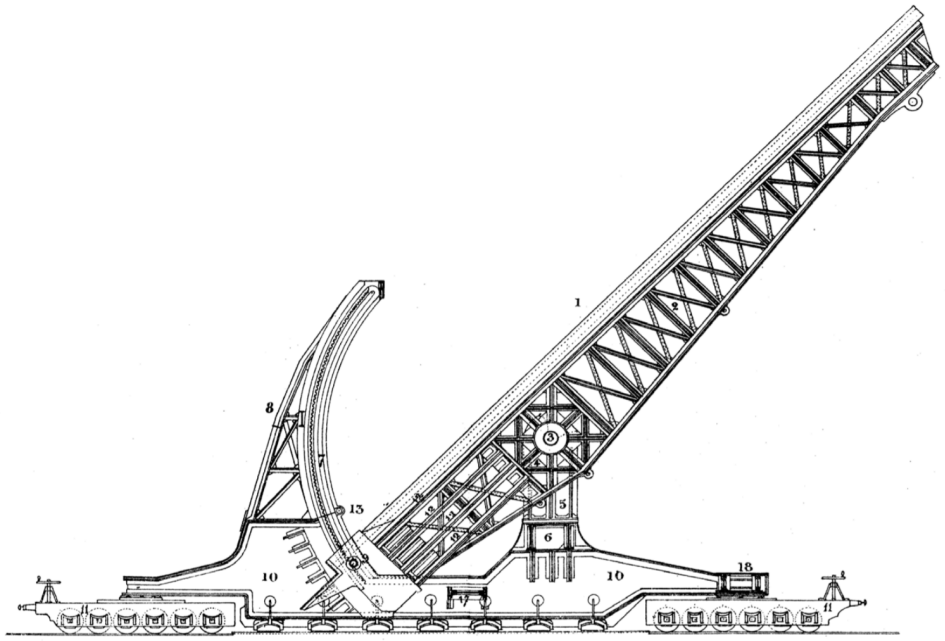

Figure 1.7: Fauchon-Villeplees rail-mounted railgun [3].

with today's technology. German and Japanese researches are conducted in World War II. These early EML research is greatly reviewed by Ian R. McNab [3], interested readers can check his work.

1.2.2 TUFAN

ASELSAN Inc. has been conducting experimental research on EML technologies since 2014. First-generation 1-MJ and second-generation 3.25-MJ pulse power supplies (PPSs) were built and tested with 25 mm x 25 mm bore EMFY-1 Launcher at an open area test range by ASELSAN. Muzzle energies upto 100 kJ was obtained through these tests. The muzzle energy is defined as the kinetic energy of the projectile at the end of the rail which is demonstrated in (1.7) where m_p is the mass of the projectile, and v_m is the exit velocity of the muzzle velocity. Efficiencies of these launches are around 13%, varying test to test, but the deviation is not that much, around 2-3% Muzzle efficiency which is defined as in (1.8).

$$E_m = \frac{1}{2} m_p v_m^2 \tag{1.7}$$

$$\eta = \frac{E_m}{E_{PPS}} = \frac{\frac{1}{2}mv^2}{\frac{1}{2}CV^2} = \frac{mv^2}{CV^2} \tag{1.8}$$

In 2018, ASELSAN built an EM launch laboratory to perform experiments up to 2-

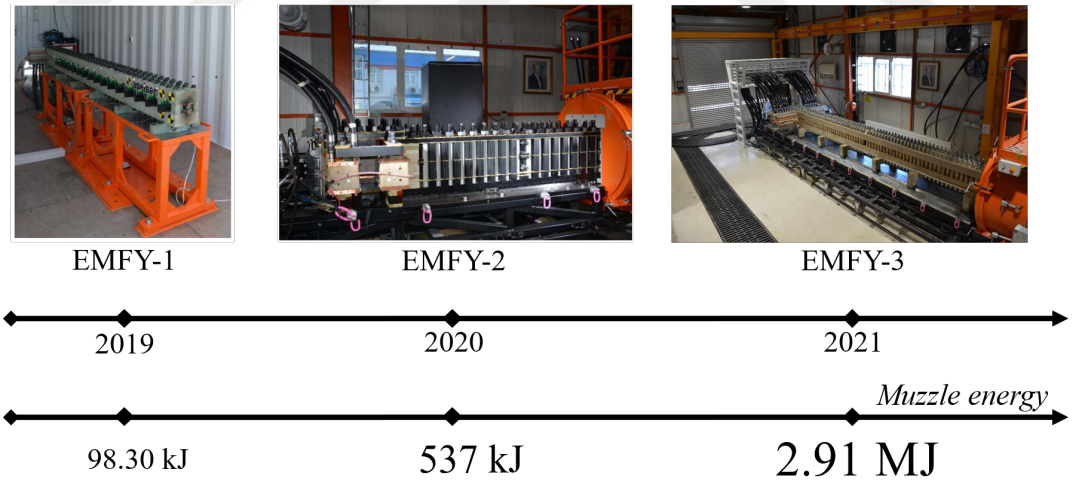

Figure 1.8: EMFY-2 Launcher

MJ muzzle energy. The second and the third generation EMLs were built and tested in the indoor laboratory. The laboratory is shown in Fig. 1.9.

EMFY-2, the second generation EML, has a 50 mm x 50 mm square bore. It has

Figure 1.9: EMFY-2 Launcher Lab. view

a 3-m length rail. In Fig. 1.10, one of the research armatures is designed for the EMFY-2 launcher is shown. Muzzle energy is increased five times, from 100 kJ to 537 kJ, regarding EMFY-1, although the rail size is still the same. Launch efficiencies increased roughly by 5%.

EMFY-3, the third generation EML, has 50 mm x 75 mm bore, 6.1 m rail length. PPS capacity is increased to 8 MJ, and 2.91 MJ muzzle energy is obtained. The muzzle efficiency is doubled considering the EMFY-2. Geometric parameters, muzzle energies, multipliers and efficiencies are given in Table 1.1.

Table 1.1: Some parameters of the EMFY launchers.

	EMFY-1	**EMFY-2**	**EMFY-3**
Rail length	3 m	3 m	6.1 m
Rail seperation	25 mm	50 mm	75 mm
Rail height	25 mm	60 mm	50 mm
Rail width	20 mm	60 mm	50 mm
Muzzle energy	98.30 kJ	537 kJ	2.91 MJ
Multiplier	-	5.46	5.43
Efficiency	13.11 %	18.08 %	36.38 %

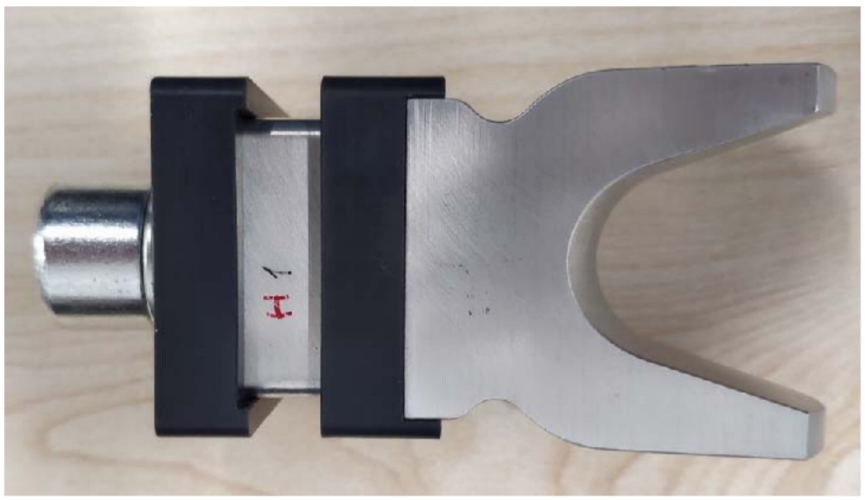

Figure 1.10: Launch package for 50 mm x 50 mm square bore EMFY-2 launcher.

Pulse power supplies (PPSs) are used to excite EMLs. To meet the power demand of the EML, several modules are needed to connect in parallel. These modules should be triggered carefully to construct the desired rail current shape. The ideal rail current has a pulse shape to create a constant acceleration and minimize eddy losses. These modules are mostly capacitive-based even though inductive topologies have larger power densities. The reason behind it, capacitive modules have mature technology, better operational reliability, and feasible financial condition. [12]. An example of a capacitive-based PPS is illustrated in Fig. 1.11 where R_c, L_c represent ESR and ESL of the capacitor, R_T, and R_D represent ON resistance of the thyristor, and diode respectively. To smooth the module currents, a pulse-shaper inductor is used, which are donated as L_{PPS}. Its ESR modeled as R_{PPS}. One module withstands currents of several hundred kA; thus, several thyristors are stacked as series and parallel. Paralleling capacitor banks can further increase the module energy capacity. In order to give a reference for these parameters, a 200 kJ capacitive-based PPS [1] is used. Values are listed in Table 1.2.

1.3 Research Goals and Objectives

In this thesis, the proposed models are built to enhance the correlation between simulations and experimental findings. Ceylan's master thesis influences the base features of the constructed model. Moreover, modeling assumptions, i.e., velocity skin effect

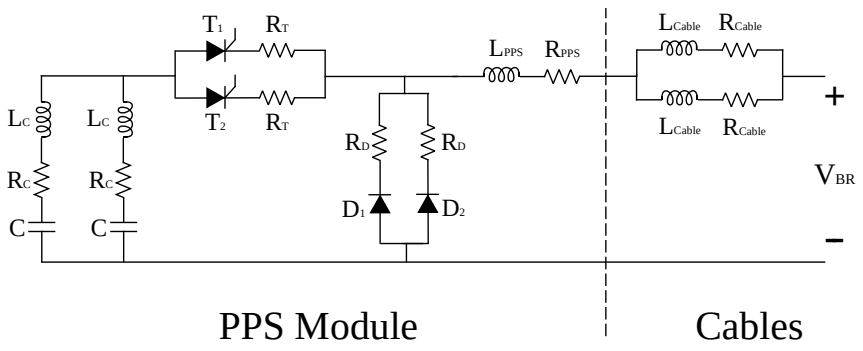

Figure 1.11: The capacitive-based PPS module model.

Table 1.2: Parameters of a 200 kJ capacitive-PPS [1].

	Description	**Value**
C	Capacitance of the capacitor bank	4 mF
R_C	ESR of the capacitor bank	0.25 mΩ
L_C	ESL of the capacitor bank	0.1 μH
R_D	ON resistance of the crossbar diode stack	0.6 mΩ
L_{PPS}	Inductance of the pulse shaping inductor	20 μH
R_{PPS}	ESR of the pulse shaping inductor	0.1 mΩ
R_T	ON Resistance of the thyristor stack	0.1 mΩ
R_{Cable}	Cable resistance	0.9 mΩ
L_{Cable}	ESL of the cable	0.44 μH

calculations and distinct phenomena like the new back-emf calculations, are proposed to improve the accuracy. It should be noted that these modeling techniques can also be applied to other low-frequency electromagnetic computation problems where large conductors are utilized.

In Chapter 2, modeling strategies and governing equations are introduced. A literature survey is shared first. Then, kine-mechanical equations are given, which are embedded in the primary model later. Moreover, some analytical formulas provided by the literature are explained considering two reasons; they are practical to use and give intuitions about EML parameters and their performances. The governing equations are aimed to provide clear perceptive about capabilities and assumptions of the simulation method. Thus, this chapter promises to be a starting point for the EML research, particularly in the analysis parts.

In Chapter 3, the primary intention is to compare VSE resistances with 2-D and 3-D

FEM methods. 3-D modeling is limited as conductors moved with significant velocities (up to 2500 m/s) with the utilized FEM package, so a different approach is shared. Rather than a mesh movement, material properties are swept to investigate VSE. This strategy is verified in 2-D. Then, the method is utilized in 3-D to understand the difference in 2-D and 3-D modeling of VSE. Empirical findings are compared with the calculations to verify the proposed enhancement. This study is summarized in the article named "A Comparison of Velocity Skin Effect Modeling with 2-D Transient and 3-D Quasi-transient Finite Element Methods".

In Chapter 4, a new technique to calculate back-EMF in the EMLs is explained. This particular technique is helpful, especially when the rail dimensions become larger considering the rail separation. Assumptions made by previous studies are presented first. Then the new EMF concept is shared. The proposed model regards the changes. Furthermore, a control method is built, which disregards the changes. These two models' results are compared with experiments to validate the claims. This study is reviewed in the article "A Hybrid Simulation Model for Electromagnetic Launchers Including the Transient Inductance and Electromotive Force".

In Chapter 5, a multi-level, fast algorithm is proposed to solve the triggering time optimization problem of the EMLs. As multiple modules are utilized considering the EML energy requirement, module excitation times should be determined accordingly. The proposed method uses a simplification with an internal hysteresis control, which reduces optimization space significantly. This strategy is compared with existing methods, such as genetic algorithm, or particle swarm optimization to show effectiveness.

CHAPTER 2

MODELING STRATEGIES AND GOVERNING EQUATIONS

In this chapter, a brief overview of the modeling strategies of EML simulations is exhibited. Firstly, serious attention is given to inductance gradient, the most crucial parameter determining the EML performance. Then, kine-mechanical equations, which are essential for the launch simulations, are explained. Finally, analytical formulas that are useful in EML research are shared.

Moreover, the governing equations of the FEM formulation, its limitations are explained in detail. Symmetry planes that are used in the simulation are shown with their examples. This section can be introductory material to researchers who starts EML research in electromagnetic aspects.

2.1 Modeling Strategies

2.1.1 Inductance Gradient

L' is the most crucial parameter that affects an EML's efficiency. The reason is that it is directly related to the propulsive force on the armature. Therefore, it should be calculated correctly in the design procedure. However, there is no single agreement in the literature on which calculation methods should be used. The reason is that there is no rigorously correct model. Whether it is an analytical model or a numerical tool, all the calculations have some degree of assumption due to the trade off between computational load and the accuracy. Therefore, methods that require less computational burden, and more accurate models are still targeted in the literature.

Early EML research (the '80s) is based on analytical models rather than complete numerical tools. The apparent reason is the lack of well-defined numerical methods in low-frequency electromagnetism or the relatively low computational power. Kerrisk proposed an analytical L' formula based on the field calculations in 2-D geometry in 1981 [13]. The rails are assumed as rectangular, although they can be convex or concave shapes, and the excitation is in the high-frequency regime. Parker *et. al* reported that Kerrisk's formula does not include the loss in propulsive force/L' when the metal containment is used [14]. Therefore, it should be noted that Kerrisk's formula will overshoot when the containment is metal rather than fiberglass epoxy composite or any other non-conductive material. Kerrisk extent his work through building a lumped EML circuit model with his L' formula in [15], and he obtained experimental verification. Lie *et. al* built an analytical formulation [16] and compared it with existing formulas such as Kerrisk's, Garber's [17], and Battah's [18]. If the reader is interested in analytical L' formulation, Liu's article is a great starting point. Moreover, these formulations are limited to rectangular rails. There is no analytical L' formulations in the literature that cover the effect of convexity/concavity of the rails.

The proposition of more than one kinds of inductance gradients are a popular modeling technique among studies. For example, Parker *et. al* defined the conventional rail inductance gradient, L'_{R}, which represents the incremental inductance in rail due to the armature motion [14]. The second definition is the propulsive inductance gradient L'_{P}, which is determined from the force calculations on the armature in the direction of motion. There are two reasons for such separate definitions. Firstly, the propulsion is related to the armature fields, whereas the incremental inductance at the breech is associated with rails. Therefore, these parameters can differ significantly. Secondly, L'_{R} is used as a parameter of a lumped circuit element, whereas L'_{P} is utilized in kine-mechanical equations. On top of that, these values have transients in time [19, 20, 21] which contradicts the common sense that L' is constant throughout launch.

Since the numerical tools' computational capacities are increased through the decades, the trade-off between accuracy and computational load is swept on the accuracy side. The study's objective is not to obtain the ultimate simulation model, but some transient phenomena are still worth investigating. These are transients due to the inductance gradient variations in the electromotive force (EMF) calculations and VSE

calculations.

2.1.2 Kine-mechanical Equations

The kine-mechanical model of EML system is explained in this section. Using the virtual work principal and conservation of energy, the force acting on the armature is given in (2.1).

$$\vec{F}_{pr} = \frac{L' I_{rail}^2}{2} \quad L' = \frac{\partial L}{\partial x} \tag{2.1}$$

$\vec{F}_{pr}$ is the propulsive force, and L' is the propulsive inductance gradient. I_{rail} is the rail current. However, the only force that acts on the armature is not propulsive Lorentz force. Friction and drag forces denoted as $\vec{F}_{fric}$ and $\vec{F}_{drag}$ have opposite direction to the propulsion. Then the net force denoted as $\vec{F}_{net}$ acting on the armature is given in (2.2) which implies that the sum of those forces can not be negative.

$$\vec{F}_{net} = max(0, \vec{F}_{pr} - \vec{F}_{fric} - \vec{F}_{drag}) \tag{2.2}$$

The Newton's second law indicates (2.3). The rest is the mechanical state transformations.

$$\vec{F}_{net} = m_{lp}\vec{a}_{lp} \tag{2.3}$$

$$\vec{a}_{lp} = \frac{L' I_{rail}^2}{2m_{la}} \tag{2.4}$$

$$\vec{v}_{arm} = \int_0^{T_{exit}} \frac{L' I_{rail}^2}{2m_{la}} dt \tag{2.5}$$

$$\vec{x}_{arm} = \int_0^{T_{exit}} \int_0^{T_{exit}} \frac{L' I_{rail}^2}{2m_{la}} dt dt \tag{2.6}$$

$$x(0) = X_{pre} \quad x(T_{exit}) = x_{rail} \tag{2.7}$$

$\mathrm{T_{exit}}$ is defined as the exit time of the armature from rails and $\mathrm{x_{rail}}$ is defined as the position of the armature reference to the breech. $\mathrm{X_{pre}}$ is the initial position of the armature with the same reference. Since the propulsive force on the armature is disappears when the armature leaves the rails, the time interval from initial time to

$\mathrm{T_{exit}}$ is examined in the calculations. The action integral[1] of the armature is defined as in (2.8).

$$AI = \int_0^{T_{exit}} I_{rail}^2 dt \tag{2.8}$$

Friction forces are responsible for a loss mechanism [22]. $\vec{F}_{fric}$ can be modelled as in (2.9) [23] where μ_d and μ_s are dynamic and static friction coefficients respectively. ζ is the friction damping factor, and $\vec{F}_C$ is the contact force.

$$\vec{F}_{fric} = (\mu_d + (\mu_s - \mu_d)e^{\zeta - v})\vec{F}_C \tag{2.9}$$

Two different drag mechanisms occur at the launch package. These are named as electromagnetic drag, and aerodynamic drag. Aerodynamic drag is simpler than the electromagnetic drag in terms of analytical model's complexity. Aerodynamic drag which is denoted as $\vec{F}_{aero_{drag}}$ can be modeled as in (2.10). $\mathrm{C_d}$ is the drag coefficient (it is a dimensionless quantity.), $\mathrm{A_{lp}}$ is the area that frontier to the air, ρ_{air} is the density of air.

$$\vec{F}_{aero_{drag}} = \frac{1}{2} C_d A_{lp} \rho_{air} v_{arm}^2 \tag{2.10}$$

$\mathrm{C_d}$ is dependent on the launch package geometry. It can be reduced with well-designed geometry, which improves efficiency. Boeing 787 has $\mathrm{C_d}$ equals 0.024, whereas a geometry with rectangular frontier surface has $\mathrm{C_d}$ equals 1.05. $\mathrm{C_d}$ of an armature with a dummy weight can be approximated as 1.

$\vec{F}_{EM_{drag}}$ is the force related to the eddy-current brake mechanism. It is mostly related to the conductive containment around the launcher. $\vec{F}_{EM_{drag}}$ can have more severe effects than $\vec{F}_{aero_{drag}}$ if the conductive containment is not laminated. Parker *et. al* [24] put the first efforts to see the doom of the conductive containment. They state that, loss of $\vec{F}_{net}$ due to $\vec{F}_{EM_{drag}}$ may be as large as 20% to 25%. When the armature moves along the rail, there is a time-varying magnetic field from the containment perspective, even if the rail current is DC. Since the armature has a few km/s speed, $\frac{d\vec{B}}{dt}$ is severe; eddy currents occur in the conductive containment. Even if infinitely thin laminations

[1] The action integral is an essential parameter for EML's armature research. Forces (propulsive and lateral), joule heating are correlated with the square of the current. Thus, action integral represents, thermal, mechanical and electromagnetic loadings at the same time.

are used[2], the magnetic field suppression at the armature can not be reduced, which eventually reduces L' [25]. However, $\vec{F}_{EM_{drag}}$ can not be modeled analytically. Even 3-D FEM computation is not feasible, as lamination requires a large number of mesh elements. Moreover, the armature motion is required to observe the eddy brake. If the containment material is magnetic, then the non-linear B-H characteristic should also be introduced to the simulation environment. Thus, the $\vec{F}_{EM_{drag}}$ modeling is computationally limited and requires further research. However, if the containment is not electrically conductive, $\vec{F}_{EM_{drag}}$ is equal to the zero.

2.1.3 Analytical Calculations

EMLs have complex geometries. Therefore, the usage of analytical formulations solely is not sufficient when the designer analyzes the system. However, analytical formulations can give insight into the design process. For example, they show relationships between objectives and parameters or shrink the parameter space when optimization is required. In this section, two well-known formula in the EML research is explained. These are Kerrisk's Formula[3] which is used for L' calculation, and Löffler formula, which is used for rail pressure calculation. After that, kine-mechanical calculations are explained analytically. EMFY-3 has used an experimental base for kine-mechanical calculations.

2.1.3.1 Kerrisk's Formula

Kerrisk's [26] formula is the one of the well-known tool to compute L'. Three parameters are used; rail separation (s), rail width (w), and rail height (h). These parameters are illustrated in Fig. 2.1. It can be used for rectangular rails only. Multiple coefficients are used for linear regression which is enriched with experimental findings. These coefficients which are shown in Table 2.1.

[2] Infinitely thin lamination minimizes eddy currents created due to the magnetic field transient made by rail current. However, the armature creates its field distribution which differs geometrically from rails. Therefore, the lamination strategy can not affect the armature's field. In [25], Mallick explained these differences by decomposing eddy currents into two considering this difference. Interesting readers can find more details in this article.

[3] Kerrisk's Formula is called as L' with *high-frequency approximation* in the literature.

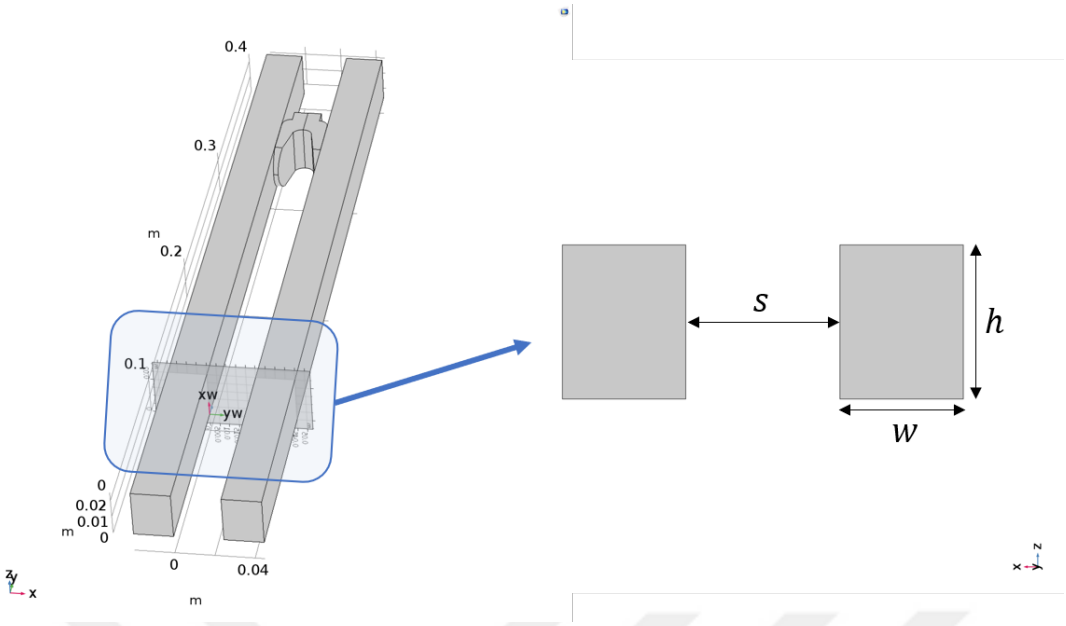

Figure 2.1: Geometric parameters of the EML.

Table 2.1: Kerrisk formula's coefficients.

	Value	**Standart Deviation**
A ($\mu H/m$)	0.441	0.003
B ($\mu H/m$)	-0.777	0.001
K_{a1}	3.397	0.146
K_{a2}	-0.067	0.007
K_{b1}	1.008	0.009
K_{b2}	2.743	0.058
K_{b3}	0.022	0.004
K_{b4}	0.264	0.039

Kerrisk's formula uses following equations, (2.11), (2.12), and (2.13).

$$F_1 = 1 + K_{a1}(w/h) + K_{a2}(w/h)(s/h) \tag{2.11}$$

$$F_2 = K_{b1} + K_{b2}(s/h) + K_{b3}(w/h) + K_{b4}(s/h)(w/h) \tag{2.12}$$

$$L' = (A + Bln(F_1))ln(F_2) \tag{2.13}$$

Kerrisk's formula have following assumptions:

- The rails are very long in the x direction (in Fig. 2.19).
- The rails are rectangular (not convex, concave).
- The rail corners are rounded (no sharp edges).
- Current flows on the rail surface only (high-frequency approximation).

To illustrate the effect of three rail parameters on L', contour plots are used. Rail width (w) is discretized into six values, 0.02 m to 0.12 m, other parameters are used in axes. These contour plots are represented in Fig. 2.2, Fig. 2.3, and Fig. 2.4.

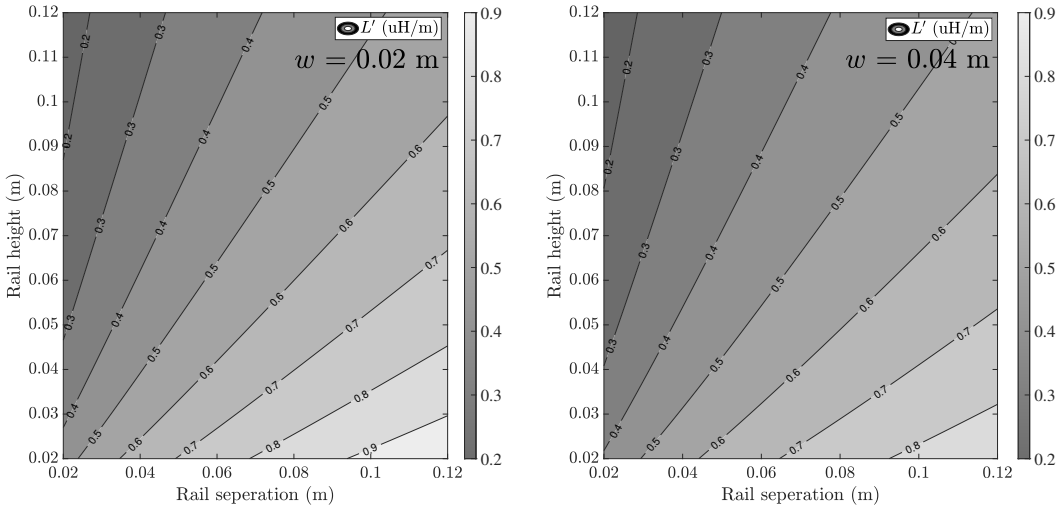

Figure 2.2: L' values respect to various rail separations and rail heights. w = 0.02 m (left), w = 0.04 m (right).

An increase in rail separation rises L' but returns are diminished when rail height and/or width are also increased. L' is more dependent on rail separation to height ratio rather than sole-dependence. An increase in the rail width decreases L' in any case.

When the rail separation is increased, there will be more magnetic flux linked between rails. Thus, the armature movement adds more inductance to the system, which results in larger L'. This effect is illustrated in Fig. 2.5. Black arrows indicate the magnetic field density vectors, whereas dashed red lines represent the integration area for L'. The rail height has the opposite effect. Larger rail height distorts the magnetic field distribution between rails, which reduces total linked flux. Such effect can be seen in

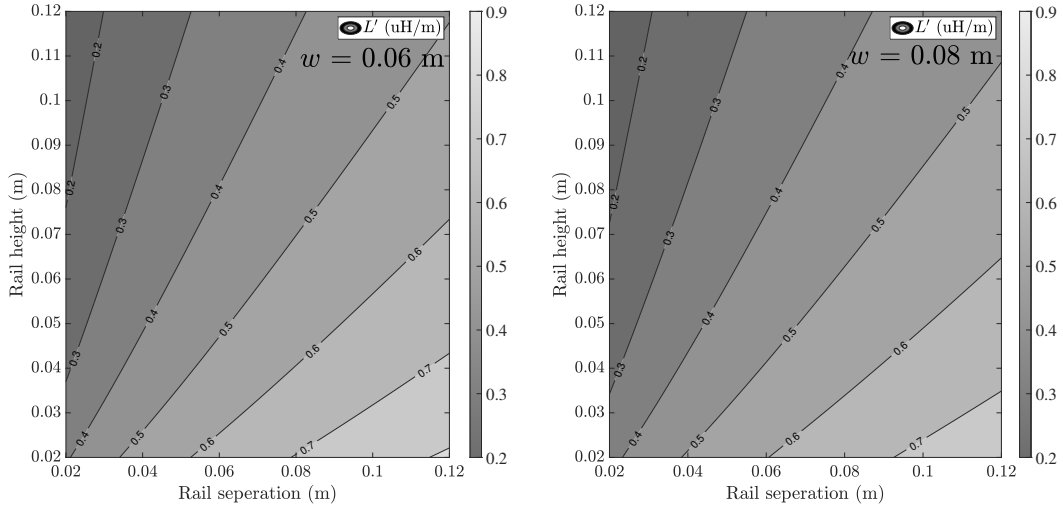

Figure 2.3: L' values respect to various rail separations and rail heights. w = 0.06 m (left), w = 0.08 m (right).

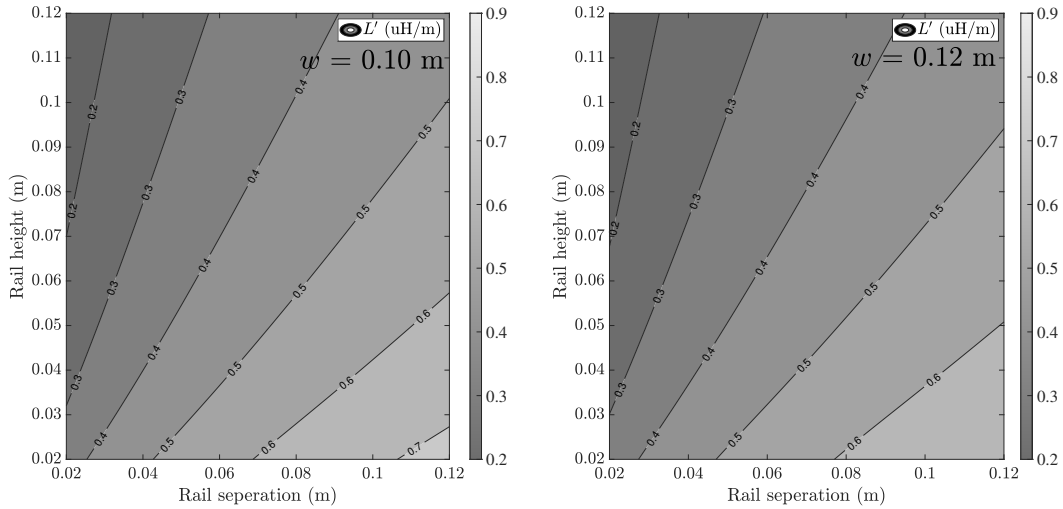

Figure 2.4: L' values respect to various rail separations and rail heights. w = 0.10 m (left), w = 0.12 m (right).

Fig. 2.6. Magnetic field density vectors have less magnitude at the integration line, although the current excitation is the same.

Rail width has similar effect on L' as rail height. Increase in rail width reduces L', as the rail current diffuses from inner rail boundary more. Thus, less flux is linked in integration boundary. This effect is illustrated in Fig. 2.7.

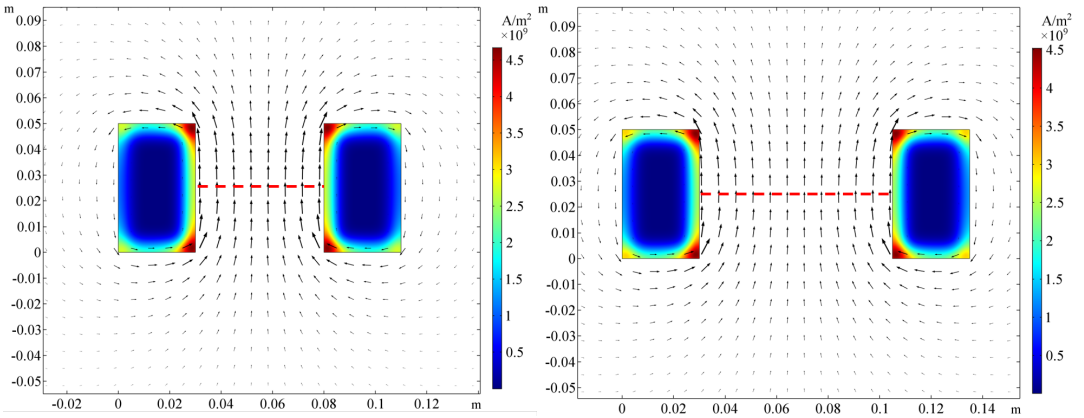

Figure 2.5: The effect of the increase in rail separation on field distributions. Black vectors represent magnetic field density. h = 0.05 m, w = 0.03 m, s = 0.05 m (left), s = 0.075 m (right)

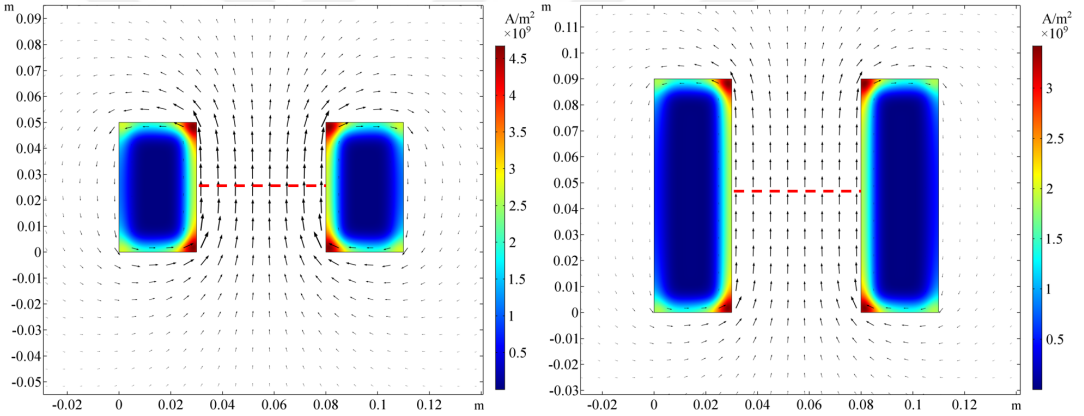

Figure 2.6: The effect of the increase in rail separation on field distributions. Black vectors represent magnetic field density. s = 0.05 m, w = 0.03 m, h = 0.05 m (left), h = 0.09 m (right)

To maximize L', rail separation should be maximized, whereas rail width and height should be minimized. However, increase in rail separation will also increases armature mass which is considered as parasitic mass. Moreover, the decrease in rail width and height increases current densities in rails. Larger current densities induce thermal consideration which reduces contact quality. Therefore, these dimensions should be selected considering not only L' but also other constraints as well.

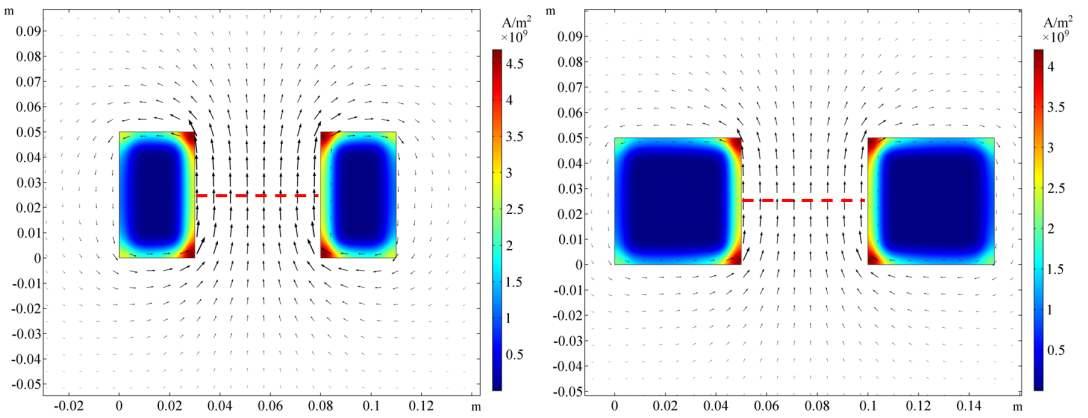

Figure 2.7: The effect of the increase in rail separation on field distributions. Black vectors represent magnetic field density. s = 0.05 m, h = 0.05 m, w = 0.03 m (left), w = 0.05 m (right)

2.1.3.2 Löffler Formula

Two conductors that are magnetically coupled exert electromagnetic forces on each other. The Lorentz force formed depends on the magnetic field and the current of the conductor. The magnetic field they generate on each other can be found with Biot-Savart which is Fig. 2.8. In EML, two rails have currents in the opposing direction, thus they push each other. The Loffler formula is used to compute rail pressure according to those forces. The geometric parameters used in Loffler formula are shown in Fig. 2.9. The formula is derived considering (2.14), and (2.15) by integrating Biot-Savart on the inner surface of the rails.

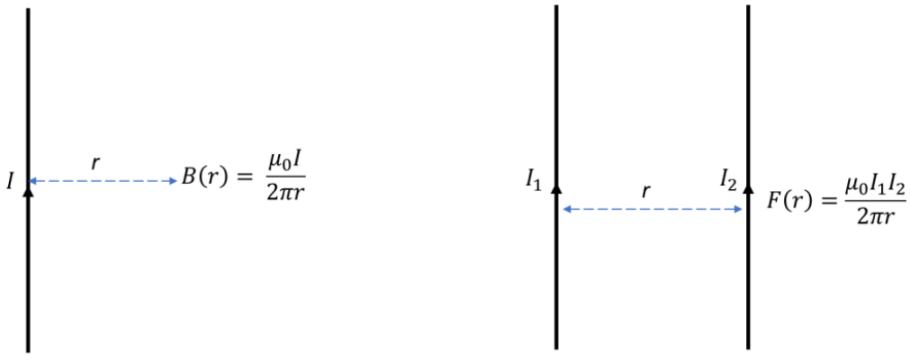

Figure 2.8: The intensity of the magnetic field around a conductor (left), the force between conductors dispersing current in the same direction. (right)

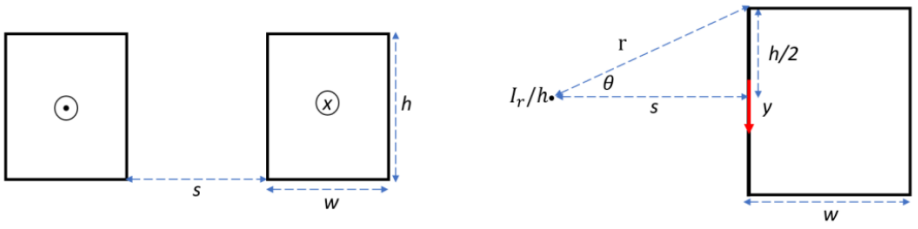

Figure 2.9: Geometric parameters used in the Löffler formula.

$$r = \frac{s}{cos(\theta)} \tag{2.14}$$

$$\begin{aligned} P &= 2\int_0^{arctan(\frac{h}{2s})} \frac{\mu_0 I_r I_r cos^2(\theta)}{2\pi h^2}\, d(tan(\theta)) \\ &= \int_0^{arctan(\frac{h}{2s})} \frac{\mu_0(\frac{I_r}{h})^2}{\pi} cos^2\theta sec^2\theta\, d\theta \\ &= \frac{\mu_0(\frac{I_r}{h})^2}{\pi} arccot\left(\frac{2s}{h}\right) \end{aligned} \tag{2.15}$$

Contour plots which show the relation between the rail pressure and rail dimensions are illustrated in Fig. 2.10, and 2.11. Each plot has different rail currents I_r those are shown as legends.

Increase in rail height and/or rail separation decreases rail pressure. Rail separation reduces propulsive force between rails by simply increasing the distance between them. Rail height, however, increase the area that propulsive forces act on. Thus, the pressure is reduced although the forces are the same.

The assumptions made under the Loffler rule are listed below;

- The effect of the armature on the rail's current and pressure has been neglected.
- It is considered that the current is completely concentrated on the inner surface. Even if the current collects inside due to the skin effect, skin thickness throughout the launch changes. Moreover the system is in DC state in the middle of the shot (assuming the pulse shaped rail current), the accumulation of the cur-

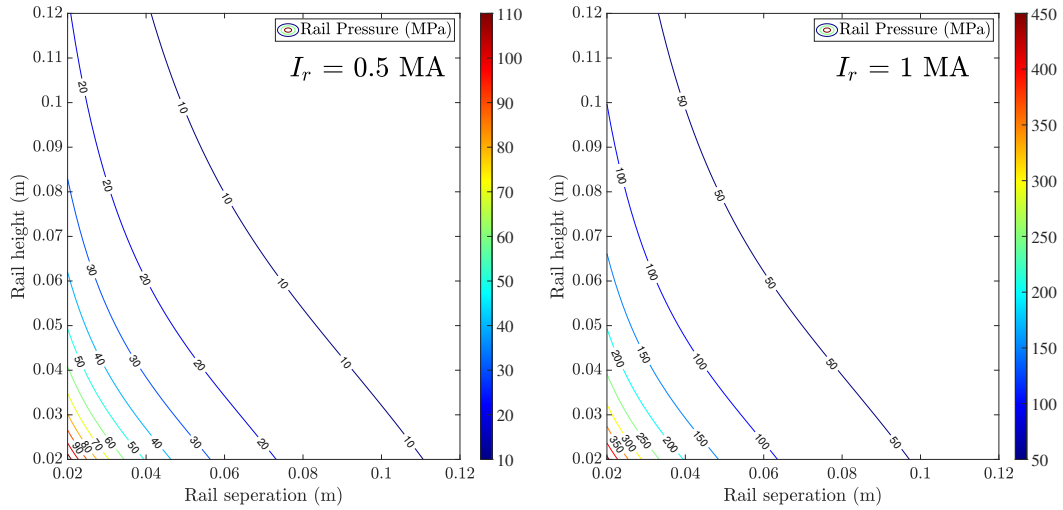

Figure 2.10: Rail pressure with respect to rail separation and rail height. $I_r = 0.5MA$ (left), $I_r = 1MA$ (right).

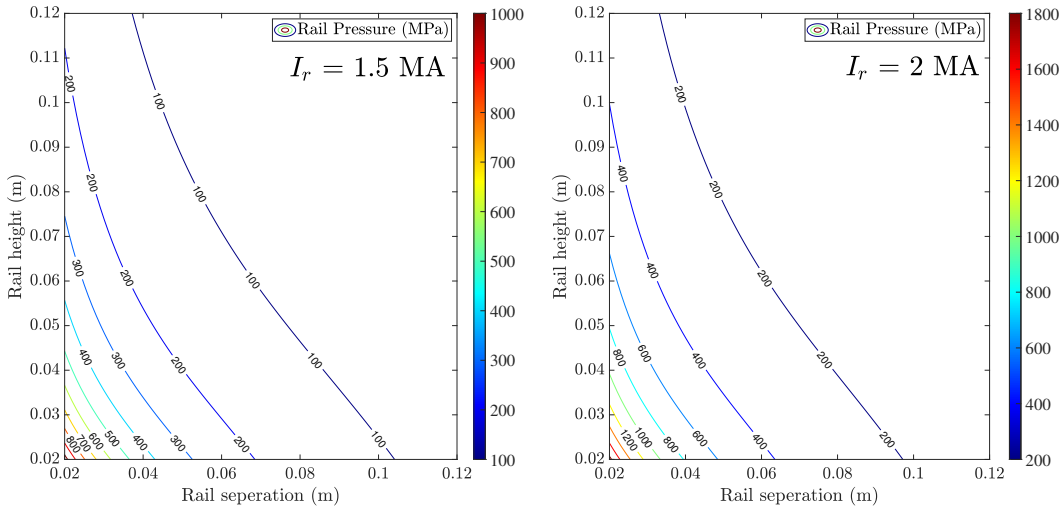

Figure 2.11: Rail pressure with respect to rail separation and rail height. $I_r = 1.5MA$ (left), $I_r = 2MA$ (right).

rent on the inner surface tends to decrease the pressure value. However, these transient in the rail pressure is neglected.

- It is considered that the current is homogeneously distributed in the direction of the rail height.

2.2 Governing Equations and Limitations

In this section, the governing equations of the FEA are described briefly. Although Maxwell equations are valid in all mediums of any time and space, the formulations do not directly impose all equations in one. For example, Ampere's law is directly implied in general transient magnetic field simulations; Faraday's law is a better alternative where superconductors are investigated[4]. Therefore, before going into details of the simulation models, it is essential to examine the formulations, which assumptions are made, what are the limitations are, etc. Moreover, common symmetry features which often appeals in FEA are described in EML geometries.

As a consequence of Maxwell's equations, currents and charges are not synchronized with changes in electromagnetic fields. The reason is that there is a finite time for the propagation of these fields. When the wavelength of the excitation current, which is denoted as λ, is too large with respect to the conductor length (typically a few meters), propagation delays can be negligible. This assumption is called *the quasi-static approximation*. The excitations for EMLs are a few hundred Hertz. When the excitation is 1 kHz, λ is roughly 299 km. Thus, the quasi-static approximation is valid, and the displacement currents can be neglected, as in (2.16).

$$\nabla \times \vec{H} = \vec{J} \tag{2.16}$$

Constitutive relations are described in (2.21) and (2.18). The magnetic vector potential, denoted as, $\vec{A}$[5] is defined as in (2.19).

$$\vec{B} = \mu_0(\vec{H} + \vec{M}) \tag{2.17}$$

[4] Although superconductors have practically zero resistance, the phenomena is dependent with the critical current density. The dependence of conductivity on the current amount makes it difficult to solve the problem when Ampere's law is imposed. The reason is that a circular dependency arises because the current-density calculation contains the conductivity, leading to a conductivity that is dependent on itself. The formulation which comes from Faraday's law fits better in that situation. See COMSOL's "Superconducting Wire" application note for further detail.

[5] The intuition behind the magnetic vector potential is not easy to understand as in the electrical scalar potential case. Moreover, the uniqueness of the numerical solutions with $\vec{A}$ is not guaranteed unless with suitable gauge transformations. The author suggests the interested readers to look at Feynman's lecture on *The Magnetic Field in Various Situations* for understanding, and COMSOL AC/DC Module Application Notes for further details.

$$\vec{E} = -\nabla V - \frac{\partial \vec{A}}{\partial t} \tag{2.18}$$

$$\vec{B} = \nabla \times \vec{A} \tag{2.19}$$

The current density $\vec{J}$ can be rewritten as (2.20) where $\vec{J_e}$ represent the excitation current.

$$\vec{J} = \sigma(\vec{E} + v \times \vec{B}) + \vec{J_e} \tag{2.20}$$

Then, the Ampere's law can be written as in (2.21), with the quasi-static assumption and the relations in (2.21), (2.18, (2.19). When all bodies are modeled as static, the v term disappears from (2.21). Moreover, $\vec{M}$ term is also assumed as zero; there is no magnetic source except the rail current. The ∇V term is diminished when all materials have homogeneous electrical conductivity. Thus, the final form (2.21) becomes (2.22). The only unknown parameter is the $\vec{A}$.

$$\sigma\frac{\partial \vec{A}}{\partial t} + \nabla \times (\mu_0^{-1}\nabla \times \vec{A} - \vec{M}) - \sigma v \times (\nabla \times \vec{A}) + \sigma \nabla V = \vec{J_e} \tag{2.21}$$

$$\sigma\frac{\partial \vec{A}}{\partial t} + \mu_0^{-1}\nabla \times (\nabla \times \vec{A}) = \vec{J_e} \tag{2.22}$$

(2.22) is called $\vec{A}$ formulation, and it is the most straightforward formula used in low-frequency electrical machinery simulations. Therefore, the most well-known commercial FEM software use $\vec{A}$ formulation with quasi-static assumption.

2.2.1 Boundary and Symmetry Conditions

The magnetic insulation is the boundary condition that sets the tangential components of the magnetic vector potential to zero at the boundary (2.23). It can also be used as a symmetry-type boundary condition. It represents a mirror symmetry plane for the magnetic field. The perfect magnetic conductor boundary condition set the magnetic field intensity's tangential components to zero at the boundary as in (2.24). It portrays

a mirror symmetry plane for the current. Moreover, it can be considered as a dual feature of the magnetic insulation[6].

$$\hat{n} \times \vec{A} = 0 \tag{2.23}$$

$$\hat{n} \times \vec{H} = 0 \tag{2.24}$$

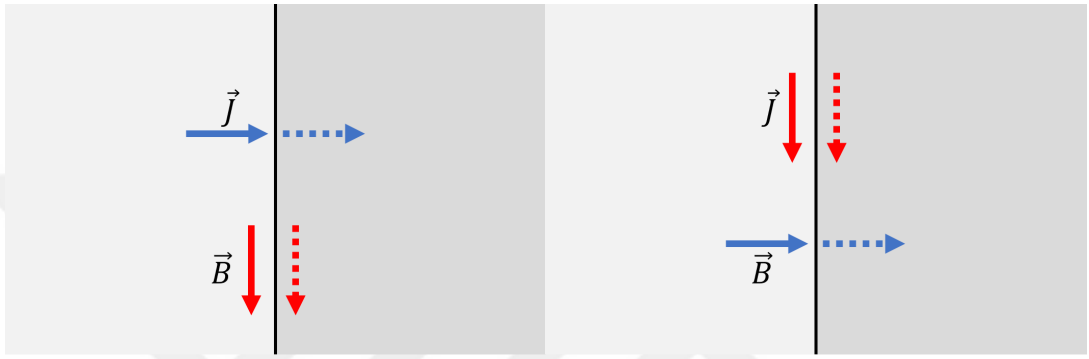

(a) Magnetic insulation (b) Perfect magnetic conductor

Figure 2.12: Boundary conditions that have symmetry feature.

Using symmetries in the FEA has an important advantage; it reduces the number of mesh elements and the number of freedom. Two types of symmetry can be used in EML FEM models. These are constructed with magnetic insulation boundary conditions (often called as *the magnetic wall*) and the perfect magnetic conductor boundary condition (called as *the electrical wall*). When two symmetry conditions are applied in the same geometry together, the resulting geometry is called as *"quarter symmetry"*. Such symmetry strategy is illustrated in Fig 2.13a and 2.13b.

These symmetry planes are demonstrated in Fig. 2.14a and Fig. 2.14b. Although the symmetry conditions are presented with (2.23), and (2.24), some clarification should be made considering the fields variables. The magnetic insulation mirrors the current density vectors through the symmetry plane in an anti-symmetric manner as in Fig. 2.15. The current density vectors are represented with black arrows. Magnetic fields only in the transverse direction with respect to the symmetry axis are mirrored. Thus

[6] The author suggests the excellent blog titled as *"Exploiting Symmetry to Simplify Magnetic Field Modeling"* by Walter Frei to interested readers.

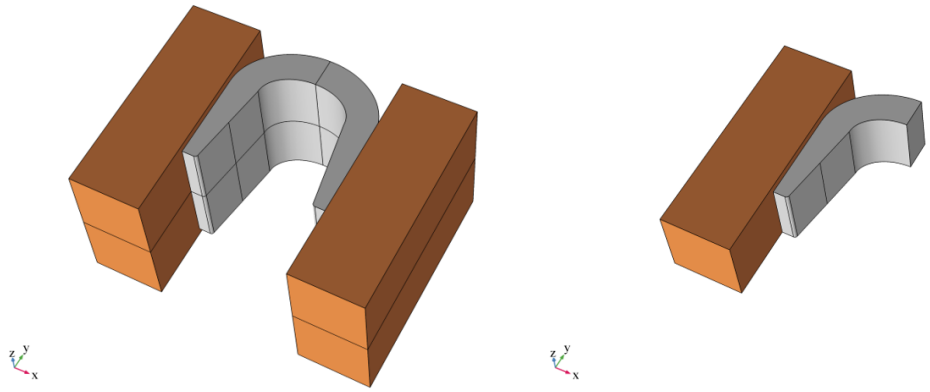

(a) Typical EML FEM geometry without symmetry (b) Reduced EML geometry, often called quarter model

Figure 2.13: Boundary conditions that have symmetry feature.

the magnetic field can not penetrate through the axis; that is why it is called the magnetic wall.

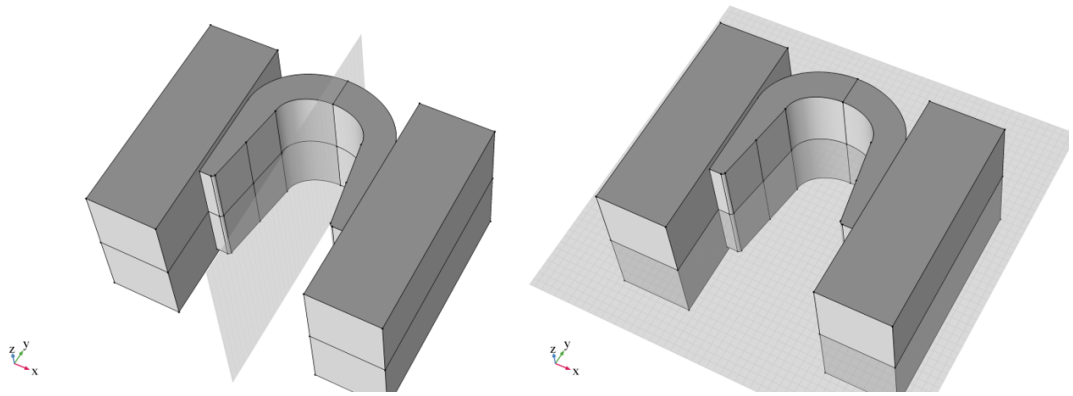

(a) Magnetic insulation (b) Perfect magnetic conductor

Figure 2.14: Boundary conditions that have symmetry feature.

The perfect magnetic conductor mirrors the magnetic field density vectors though the symmetry plane in anti-symmetric manner as in Fig. 2.16. The magnetic field density vectors are represented with red arrows. Current density vectors only in the transverse direction with respect to symmetry axis is mirrored. Thus the current can not penetrate through the axis, that is why it is called as the electrical wall.

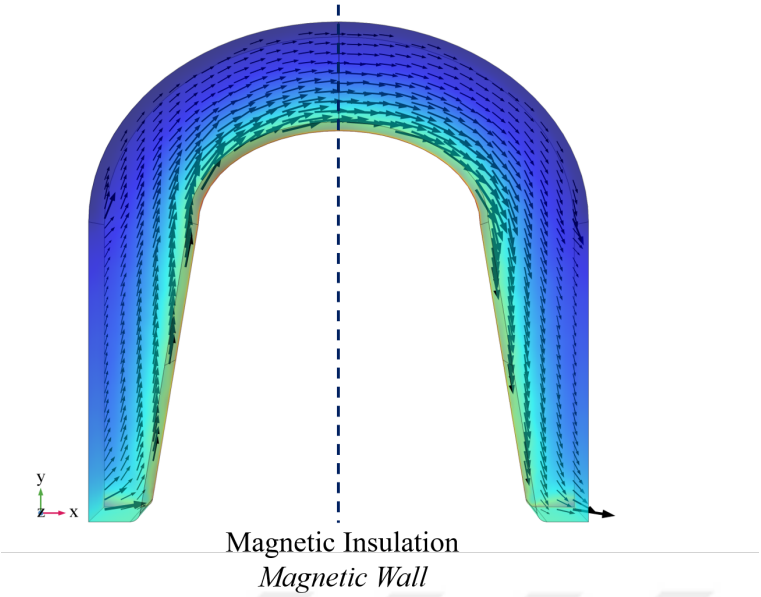

Figure 2.15: 3-D geometry of the model.

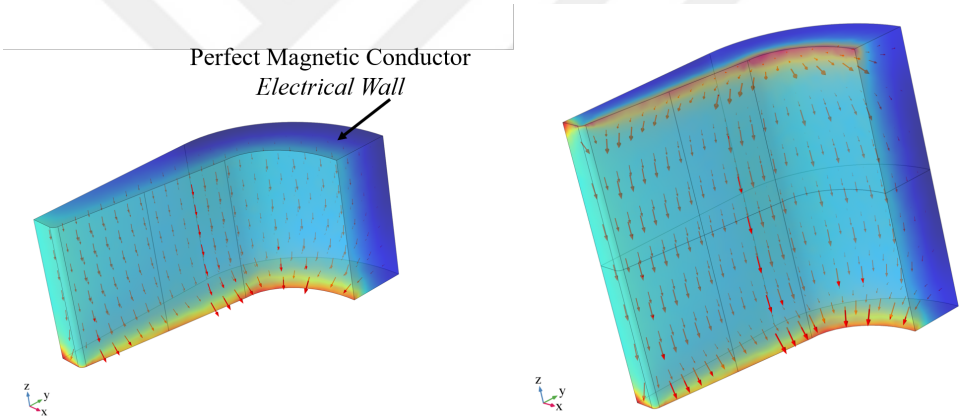

Figure 2.16: 3-D geometry of the model.

2.2.2 Limitations with 3-D FEM formulations

There are some limitations with transient electromagnetic FEM simulations. Firstly, (2.22) is built due to some assumptions. The first assumption is that all materials are static in a mechanical sense. All electro-mechanical conversion devices have some parts that are non-stationary. The problem with the FEM simulation with a mechanical motion is how we can interpret the continuity condition between stationary and moving parts. In the electrical motor/generator case, the air-gap -which is also the boundary between stator and rotor- is the boundary that continuity condition is ap-

plied. However, it should be noted that since the air is non-conductive, and (2.16) can be re-described as (2.25) in the air-gap between the stator and the rotor.

$$\boldsymbol{\nabla} \times \vec{H} = 0 \tag{2.25}$$

When there is a non-rotational vector field as in (2.25), we can declare a scalar potential ϕ as in (2.26).

$$\vec{H} = -\boldsymbol{\nabla}\phi \tag{2.26}$$

The continuity equation can then be built with a scalar potential interpolation with only one component at its spatial coordinate. Since we defined another variable rather than $\vec{A}$, this formulation is called $\vec{A} - \phi$. However, this formulation can not be used in the EML problem since the boundary between stationary rails and the moving armature is not electrically insulated like in the electrical motor case. The boundary is an electrical contact. Thus the scalar potential can not be defined since (2.25) is invalid in the electrical contact. This problem is referred to as *the sliding electrical contact* problem in the literature. Unfortunately, interpolating $\vec{A}$ in the electrical contact boundary to satisfy the continuity is not a good strategy. Since a vector element is used, there are three variables for each spatial point, challenging to interpolate. Such interpolation errors cause bad convergence in FEM, which means the simulation results are non-physical or numerically unstable. Thus, commercial FEM packages do not support a moving conductor in their 3-D formulations.

Two kinds of strategies are proposed to solve the sliding electrical contact problem;

- Improving the FEM formulation with additional variables i.e ϕ and/or V, and exploit all. Suitable boundary conditions, especially in electrical contact, should be enforced. Such an approach requires a deep understanding of numerical/approximation theory, as well as computational electromagnetic. Moreover, the number of unknowns will increase with each additional variable.

- Using "some modeling tricks." For example, to emulate the material motion, material properties can be swept rather than the actual meshes. Then, $\vec{A}$ formulation can be considered to solve the sliding electrical contact. However, it

should be noted that $\vec{A}$ formulation is based upon the assumption that all materials have non-varying electrical conductivity. This fact includes some errors in the FEM model. However, the question about how much error can be involved is not answered in the literature.

In this thesis, the error limits of such an assumption are questioned. Since there are no commercially available FEM packages that can model the sliding contact, the VSE is benchmarked empirically. The additional resistive effect due to VSE is obtained from experimental results and compared with our simulation model. The exploited VSE resistance is a critical lumped parameter for the overall system simulations. The simulation-experiment correlation is enhanced with the proposed method. The same procedure is applicable with different caliber EMLs or actuators, which have VSE on their conductors.

The second factor that limits the performance of the FEM is high aspect ratios. The aspect ratio is defined as the ratio of the largest dimension to the smallest one in particular geometry. A high aspect ratio occurs with long, thin elements. A cube has a unity aspect ratio, but a rail can have dozens since the typical rail length is a few meters but rail width and height a few centimeters. Geometries with a high aspect ratio require many mesh elements since the minimum length of the mesh elements is determined by the shortest length. For this reason, the analysis of EMLs is computationally expensive, and partial models are preferred over the complete geometry.

2.2.3 The 2-D Formulation

2-D FEM models are constructed when field variables do not change, or variation can be negligible in the symmetry direction. When solving a vector field such as $\vec{A}$ in 2-D, there are three options: to solve for the out-of-plane vector potential, the in-plane vector potential, or the three-component vector potential. Since $\vec{A}$ and $\vec{J}$ share same directions, these options should be chosen the way that currents flow.

2.2.3.1 Out-of-plane Vector Potential

When the current flows into symmetry plane with normal direction only, out-of-plane vector potential should be solved solely. Thus, tangential components of the vector potential is settled to zero. An example is illustrated in Fig. 2.17. Assuming that the armature has no influence on the rail current distribution (far-field assumption), the rail current distribution has symmetry along x-axis. Thus, the symmetry plane can be used in 2-D FEM model. The current distribution and the magnetic vector density vectors are shown in Fig. 2.17. It should be noted that this model can be used for L′ calculation when the rails are excited with some high-frequency current.

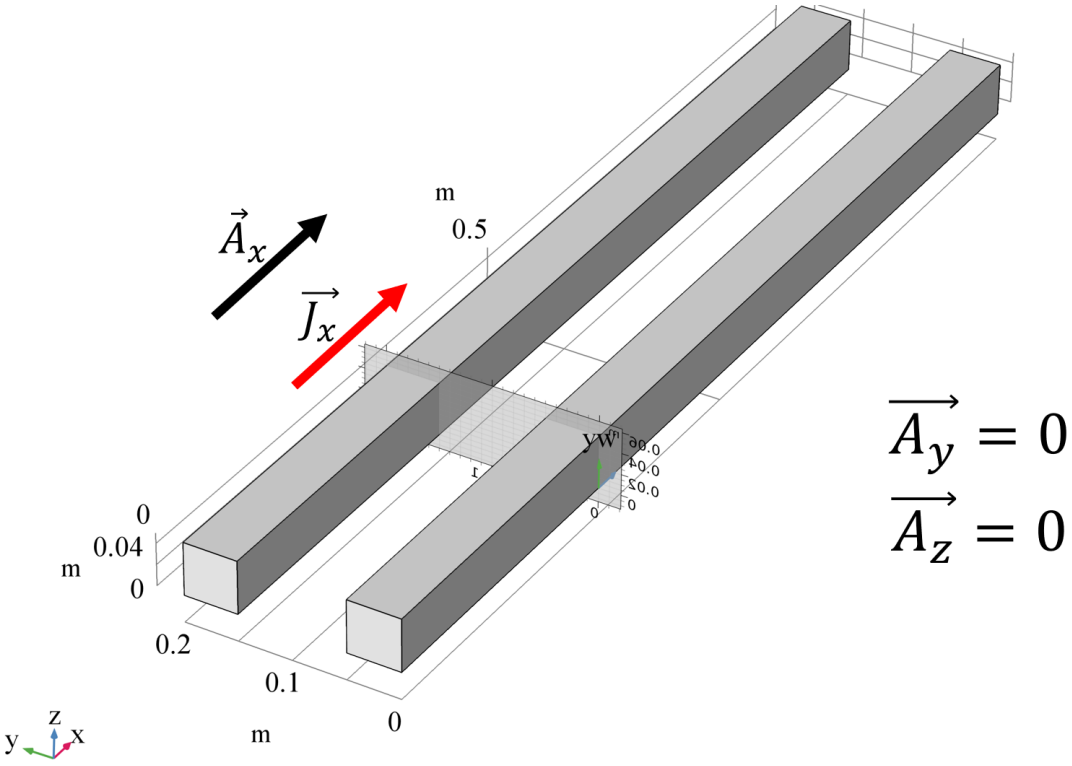

Figure 2.17: 2-D symmetry plane where out-of-plane vector potential usage is useful.

2.2.3.2 In-plane Vector Potential

Unlike the out-of-plane vector potential formulation, the in-plane vector potential assumes that currents flow only tangentially to the symmetry plane. A case for the usage of in-plane vector potential is shown Fig. 2.19. It should be noted that, the

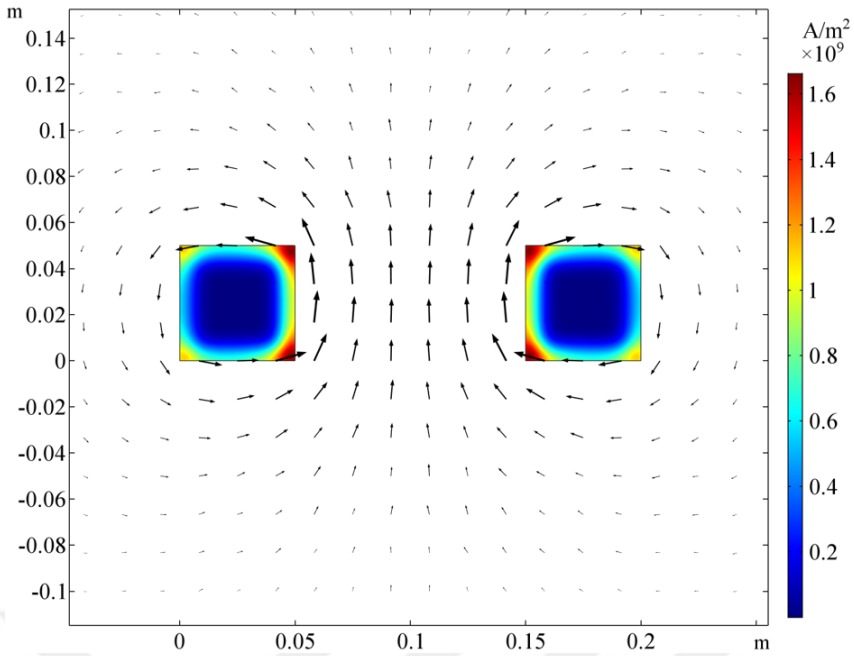

Figure 2.18: The current distribution in the rails and magnetic field density vectors in 2-D. The Rail current is 1.5 MA DC.

symmetry plane is can be used as perfect magnetic conductor boundary condition in 3-D models to exploit symmetry. The reason is in that plane, current directions are in plane-directions only. If the purpose of the analysis is to obtain field variables in that plane, in-plane vector potential is advantageous, as it reduces complexity dramatically. For example, since the maximum magnetic field density occurs that plane, the 2-D model works well. However, if field variables which are not belong to the symmetry plane are important, this model creates errors in its calculation. The reason is the rest of the geometry does not have symmetry naturally. Analysis where a volume integral is required (i.e. resistance calculations) can have serious error margins.

2.2.3.3 Three-component Vector Potential

The three-component vector potential uses variables in all directions unlike other two formulations. Even if a symmetry is used, each node in the 2-D space are represented with three-component vector potential. Therefore, there can be a current vector in each direction. This formulation have more complexity than other two alternatives. However, if the accuracy is needed (i.e. 2-D simulations, where the armature is

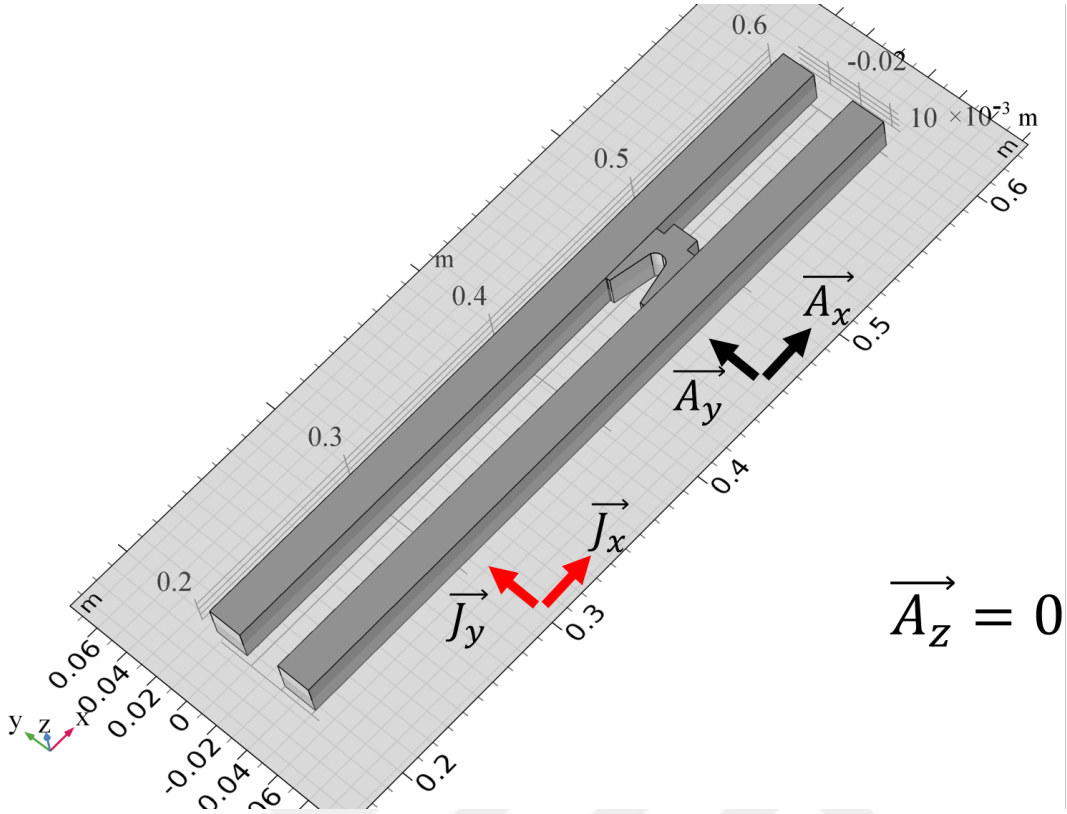

Figure 2.19: 2-D symmetry plane where in-plane vector potential usage is useful.

moved), this formulation is more suitable.

2.3 Conclusion

In this chapter following remarks are obtained;

- $\vec{A}$ formulation has a disability to model moving contact, which shares electrical contact in 3-D. The convergence issues force the new approaches to observe velocity-related phenomena.
- L′ can be correlated with rail separation to height ratio. Kerrisk formula is a practical analytical tool for L′ calculation.
- To increase in the rail height reduces the L′. Rail width also has the same characteristic. Both two geometric parameters are bounded with the maximum current density limit.

- An increment in the rail separation raises the L'. However, it also increases the armature mass, which reduces the projectile mechanical energy (as both projectile and armature share the same propulsive force).
- EML geometry can be reduced by using quarter symmetry.

CHAPTER 3

VELOCITY SKIN EFFECT MODELLING USING 2-D TRANSIENT AND 3D QUASI-TRANSIENT FINITE ELEMENT METHODS

Velocity skin effect (VSE) is a current narrowing phenomenon which is observed between two conductors that have a significant relative speed difference[27]. The physical reasoning is identical with skin effect, nevertheless, the field gradient is caused by conductor movement. Large armature velocities (>500 m/s) create severe current narrowing and large magnetic and temperature field gradients. Such effects not only create a resistive loss mechanism [28] but also carry significant risks to develop permanent damage in the rails and the armature. The launch security and the rail life-span would be under threat unless VSE were correctly examined. In Fig. 3.1, the current distribution in rails and the armature are given for steady and moving armatures. The current narrowing phenomenon is observed in the 2-D Transient simulation model.

Although the VSE is an important phenomenon, research efforts for VSE is not complete in the literature. The fundamental reason is computational limits due to velocity-dependent enormous gradients at the armature and rail interface, which is quite complicated to compute. Hsieh [29] *et. al* investigated the numerical issues with VSE computation that affect the accuracy in railgun codes. They indicate that only velocities less than 500 m/s could give reliable results. This article was written in 2001, and still, there is no commercial FEA software that tackles VSE computation in 3-D EML reliably [30]. Thus, special FEM codes are needed as commercial software is solely used for static mesh elements in 3-D electromagnetic FEM simulations due to

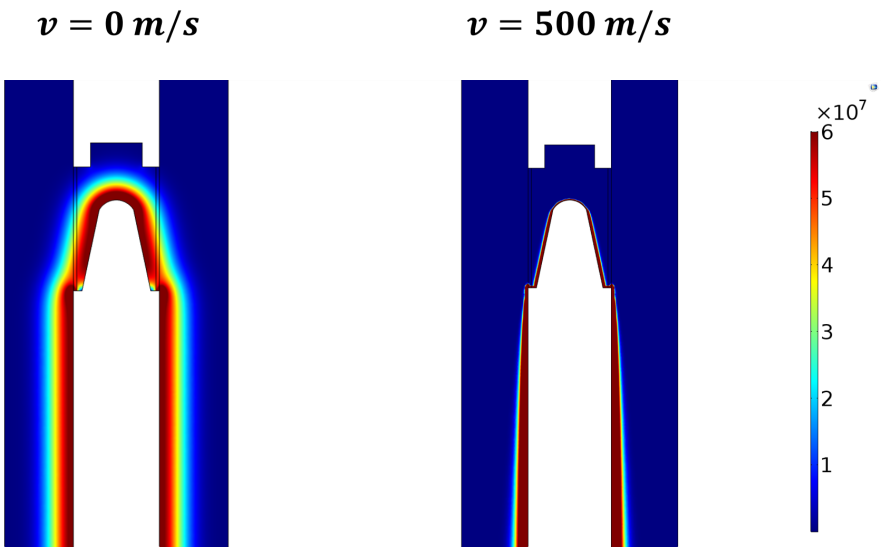

Figure 3.1: 2-D transient FEM results with stationary and moving armature. Colours represent the current density distribution, and it has unit $\frac{A}{m^2}$.

its formulation which is given in (3.1).

$$\sigma \frac{\partial \vec{A}}{\partial t} + \mu_0^{-1} \nabla \times (\nabla \times \vec{A}) = \vec{J}_e \tag{3.1}$$

There are non-commercial software which have capability to use dynamic (moving) mesh elements in EML problems. EMAP3D code uses Lagrangian description and rail reverse motion techniques[31], which is also called the upwinding method to simulate the electrical sliding contact problem under transient conditions. EFFE software[32, 33] also utilized the same technique; rail moves backward rather than the armature movement. Quasi-static, time-harmonic FEM are also used to model velocity induced resistances[34, 35]. Nonetheless, it should be noted that building these codes from scratch requires large teams with numerical background and several technical support unlike commercial ones. Moreover, even if the code have capability, it should have minimum computational complexity, since a complete rail modeling of EML requires a large number of mesh elements.

There are two computational domains in Transient[1] FEM models; stationary and moving. Rails and air domains belong to the stationary part, whereas the armature and

[1] From now on, the term *"transient"* refers to the armature motion, not time-dependent simulations. All simulation models covered in this section are time-dependent

surrounding air relate to the moving part. Continuity conditions are applied between two parts to solving discontinuity in the field distributions. In this case, at the intersection between the moving and stationary parts, there must be extrapolation as there are two independent mesh nodes around the exact spatial points. However, there is another case. For example, Quasi-Transient (Q-T) methods, where instead of mesh movement, the material properties are swept in the direction of the motion. In this case, the continuity condition is not required between the two domains. The intersection region is simply connected. An example of such a strategy can be Shatoff *et al.*'s work. In this particular study, they moved the rail conductivity backward to the actual armature moving direction and applied a stationary armature to simulate the relative motion, and current distribution at the rail-armature interface is targeted. Furthermore, Hundertmark *et al.* [36] used time and position-dependent conductivity function armature-air domain, and let rails are stationary. Transients due to the armature movement at the rail-armature interference are targeted. In the earlier study [21], we got a lumped VSE resistance through a similar conductivity function to improve the simulation model's precision. These efforts are validated with empirical data [37, 21].

In this work, we go further in the studies on Q-T FEM literature. The Q-T strategy is used to determine the correctness of 2-D models in VSE calculations. The study is carried in a 2-D Q-T FEM and checked with a 2-D transient FEM, where mesh elements move as a domain, not their material properties. VSE resistances are obtained for different armature speeds. As the Q-T strategy is verified, VSE resistances are evaluated in 3-D Q-T FEM to exploit any potential difference due to 2-D and 3-D differences. Adjusted VSE resistors are added to 3-D FEM static simulations as in [37, 21], individually as a figure of merit. The constructed model is compared with the experimental results to evaluate the performance of the VSE models. Two different launchers, The EMFY-1 and EMFY-2 launchers, are utilized for this purpose. The geometric parameters of these launchers are given in Table 3.1. It is essential to have two different EMLs to eliminate any possible bias in the study. Before going into the details of the research models conducted, the models are briefly explained.

Table 3.1: Geometric Parameters of Launchers

	EMFY-1	**EMFY-2**
rail thickness	20 mm	60 mm
rail height	25 mm	60 mm
rail seperation	25 mm	50 mm
rail height	3 m	3 m

3.1 Models

Since the study aims to search VSE resistances, at 2-D and 3-D simulation environments, multiple models are used. Four different models are used. These are the 2-D Transient FEM (2D-T), 2-D Quasi-Transient FEM (2D-QT), 3-D Quasi-Transient FEM (3D-QT), and 3-D Hybrid FEM model. The properties of the models are given in Table 3.2.

3.1.1 2-D Transient FEM

In 2-D Transient FEM, the armature is modeled with moving mesh elements. Armature modeled as C-shaped since it is general choice for solid armatures. The model geometry is illustrated in Fig. 3.2[2]. Since there are moving mesh elements two different domains constructed. These are stationary domains denoted as Ω_{s} and moving domains denoted as Ω_{m}. They are illustrated in Fig. 3.3. Air domains very near to the armature are modeled as stationary, thus they are not deformed. Air domains below and ahead of the armature are deformed to create motion. Partial differential equations with proper boundary conditions are introduced to create mesh displacements. Since rails are stationary whereas armature and air between rails not, there are discontinuous mesh nodes in the rail-armature interface different from static models. The continuity condition is applied at the interface to interpolate the field variables. Magnetic insulation is settled as the continuity condition[3].

2-D models are built on the fact that field variables do not change in the symmetry direction. Thus, in the VSE investigation of EMLs, it mean that the rail's current

[2] It should be noted that the model geometry can be halfed using symmetry feature.
[3] Magnetic insulation creates perfect electrical contact.

Table 3.2: Properties of simulations models used.

Model Name	**Mesh Type**	**Armature Shape**	**Armature Motion**	**Purpose**
2-D Transient FEM	moving	C-shaped	moving meshes	obtaining $\mathrm{R_{VSE}}$ under 2-D assumption.
2-D Quasi-Transient FEM	static	rectangular	conductivity sweep	obtaining $\mathrm{R_{VSE}}$ validate Q-T strategy.
3-D Quasi-Transient FEM	static	rectangular	conductivity sweep	obtaining $\mathrm{R_{VSE}}$ without 2-D approximation.
3-D Hybrid FEM	static	C-shaped	armature has no motion.	comparison with experimental results.

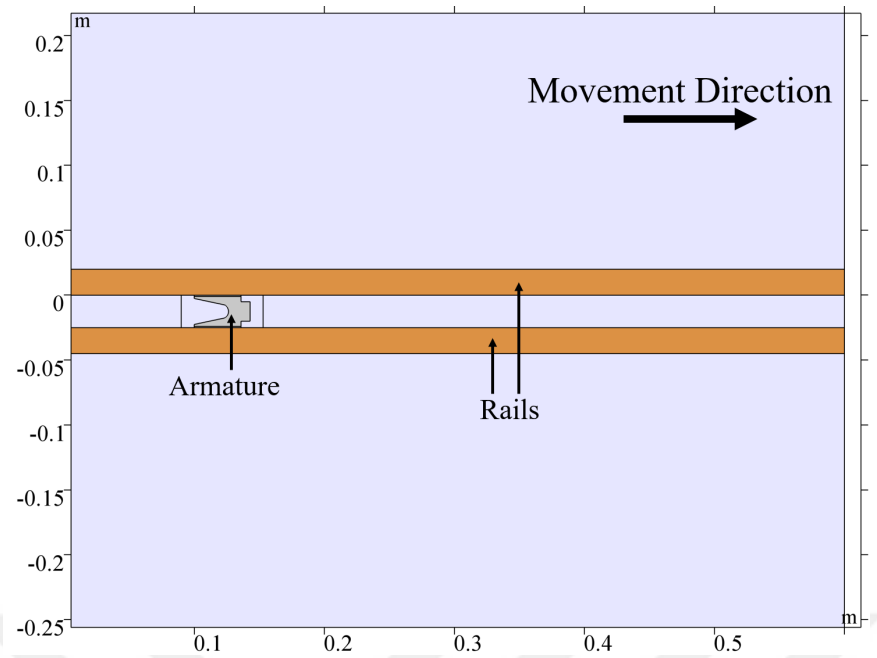

Figure 3.2: 2-D transient model geometry

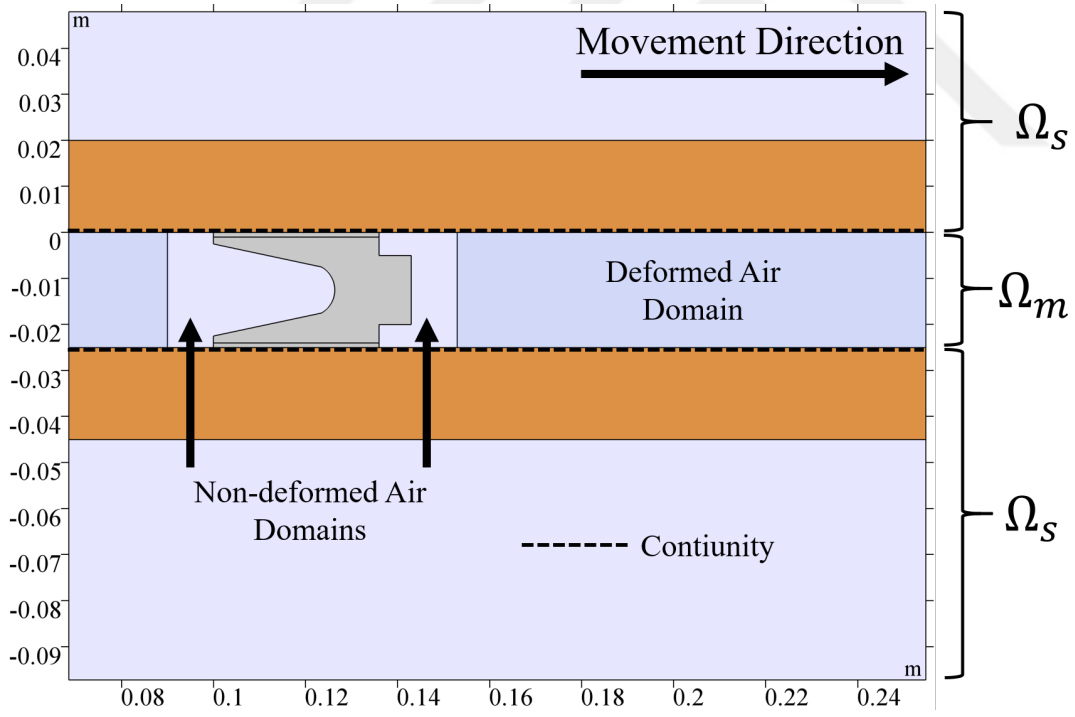

Figure 3.3: Computational regions

distribution does not change through rail height.

3.1.2 2-D Quasi-Transient FEM

Q-T strategy is based on the material property movement rather than mesh elements. Nevertheless, the accuracy of the strategy is still engrossing without solid proof. The purpose of the model in this section is to validate the accuracy claim. Since mesh movement in 3-D FE models is not available for low frequency electromagnetic analysis[4], the claim is tested in 2-D. The armature's time and position dependent electrical conductivity function is illustrated in Fig. 3.4. Although, the armature is illustrated as C-shaped, in Q-T models armatures are modelled as rectangular. The reason is the material function is moving pulse-shaped, rather than complex surface function. Mesh structures of 2-D Transient and 2-D Q-T models are presented in Fig. 3.5. 2-D transient FEM model uses discontinuous mesh structure as in Fig 3.5(a) However, 2-D and 3-D Q-T FEM and 3-D Hybrid FEM models use continuous mesh structures. The reason is not they use static meshes, unlike the 2-D transient model. Fig. 3.5(b) shows meshes of the 2-D Q-T model. The conductivity function which is used for armature motion emulation is shown. The armature has 50 mm in length and sits at 0.2 m at the start. Red rectangles represent the zoomed areas.

2-D Q-T and 2-D transient models are analyzed in terms of field distributions to approve the effectiveness of the Q-T strategy. According to the results, these two models have exact current density distributions. Each model's rail current density distributions concerning different armature velocities are illustrated in Fig. 3.6. Error distributions of current densities are also demonstrated. The points that the rail current penetrates the armature (armature tails) and the armature's moving direction are indicated with arrows. In error plots, zero errors are symbolized with black pixels.

3.1.3 3-D Quasi-Transient FEM

Deep physical insight is demanded for precise use of the velocity feature in electromagnetic analysis. Material properties alter in this direction of the armature motion. As mentioned before, the mesh movement at the sliding contact is not an option in

[4] Further details can be found in AC/DC Module User Guide COMSOL, *Velocity (Lorentz Term)*. The guide states that: "This node (Velocity) is only valid in 2D and 2D axisymmetry when only solving for the out-of-plane component of the magnetic vector potential." As the magnetic vector potential and the current density vector are in the same direction, out-of-plane solutions are not useful in EML analysis.

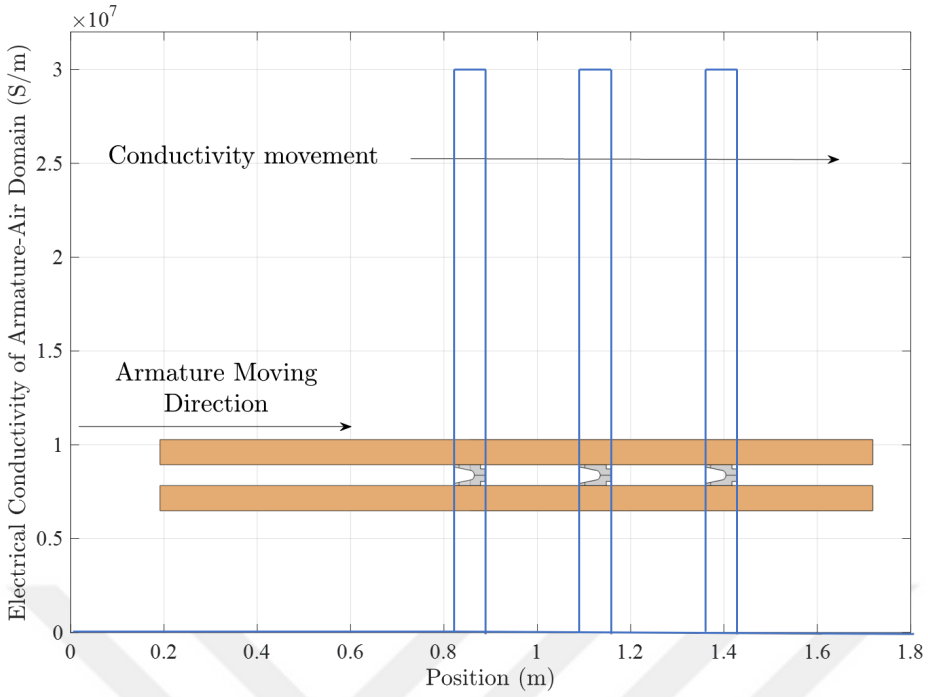

Figure 3.4: The armature's time-position dependent electrical conductivity function.

3-D. As the mesh elements are discontinuous, there exist significant interpolation errors. The underlying issue is that curl elements are used for a vector potential solution ($\vec{A}$). Three-component $\vec{A}$ vectors are used of each point. These vectors are doubled curled in the 3-D $\vec{A}$ formulation which increases the numerical instability. 2-D models use fewer components and do not necessarily compute double curl operators. Consequently, in the 3-D Q-T FEM, the armature mesh elements are not moved or deformed. However, the air-armature regions electrical conductivity is updated with time. The material properties are changed to emulate the armature movement; this approach is called the Eulerian method. It should be noted that since the mesh elements are simply-connected, field variables are continuous on all boundaries. Therefore, there is no requirement to introduce continuity conditions.

Proper time discretization is required, as all simulation models are time-dependent. There are two types of solvers; fixed and stationary. Fixed solvers have constant time-step size. Fixed-step solvers have much longer simulation times, but they are on the safe side in terms of convergence. However, variable-step solvers alter the step size while the simulation continues. They reduce the step size to improve accuracy. When

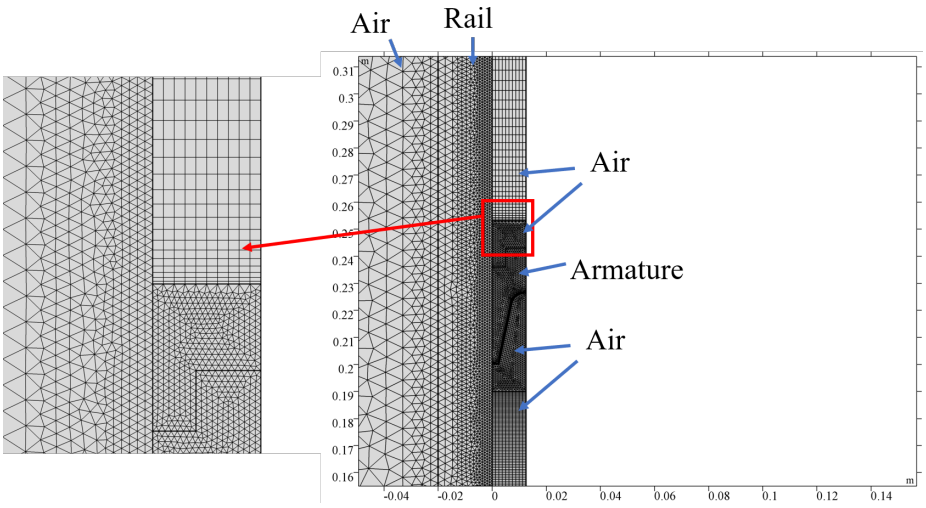

(a) Discontinuous mesh nodes.

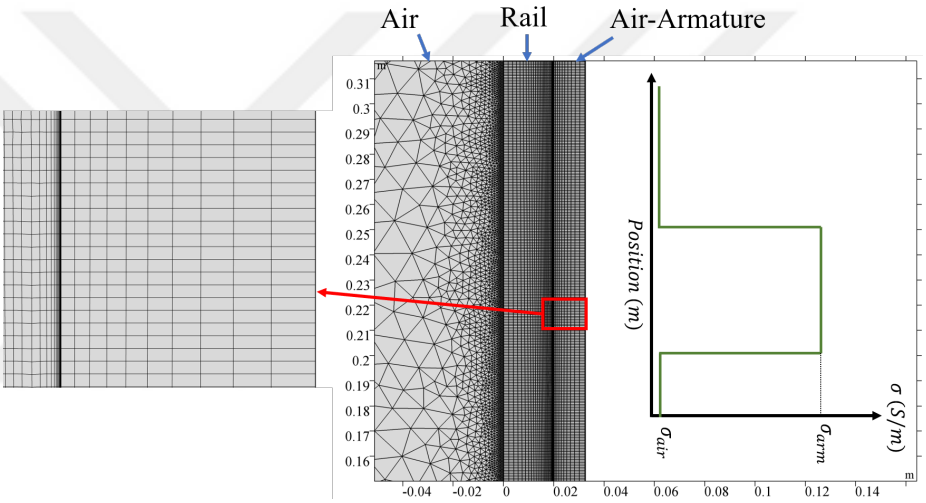

(b) Continuous mesh nodes.

Figure 3.5: Mesh structures of the simulation models.

a model's states change suddenly and increase the step size to withdraw from taking redundant steps, the model's states gradually change. In this study, a variable-step solver is utilized with a minimum time-step penalty. This penalty ensures there is no sudden conductivity jump. Time-dependent solver convergence settled a value calculated from maximum armature velocity. For example, for 1 mm maximum mesh size in the air-armature domain and 1000 m/s armature speed, time-dependent solver convergence is provided to have 0.5 μs step size as maximum to prevent discontinuity due to movement. Even though such a strategy increases simulation time as the convergence is limited, It enables us to investigate the transients due to the armature

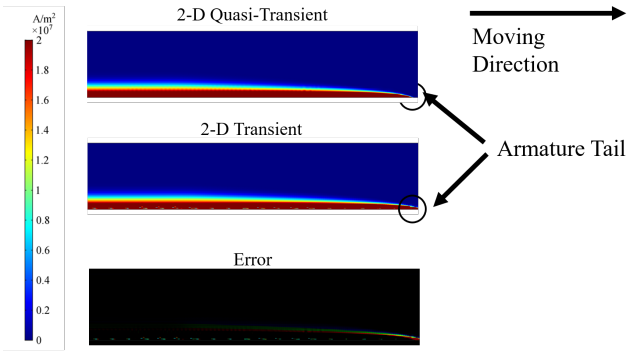

(a) $v = 500$ m/s

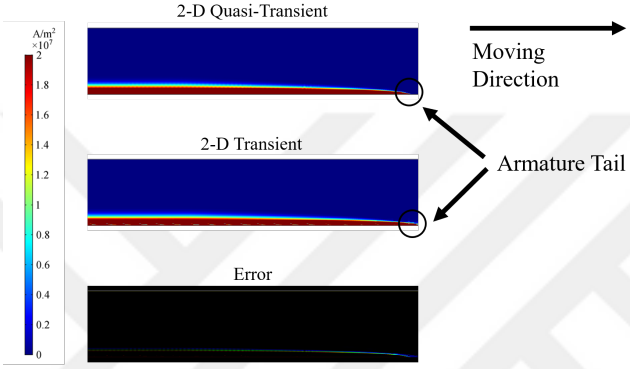

(b) $v = 1000$ m/s

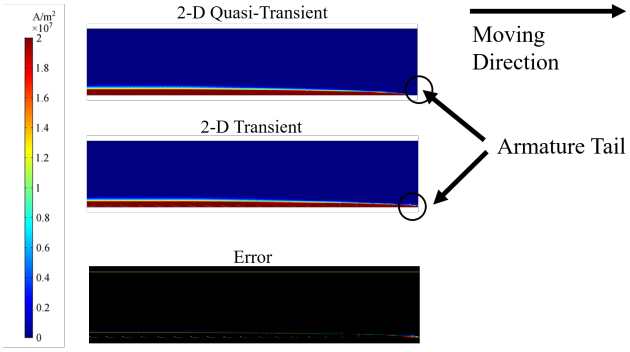

(c) $v = 2000$ m/s

Figure 3.6: Comparisons of 2-D Q-T model and 2-D transient model in terms of rail current density distribution at $v = 500$ m/s, $v = 1000$ m/s and $v = 2000$ m/s. Mean absolute error is utilized for error calculations.

movement.

When the armature has 1200-m/s speed, the current density distribution in the middle surface of the rail is illustrated in Fig. 3.7. Arrows denoted with letters used to show cross-section positions are used in Fig. 3.8.

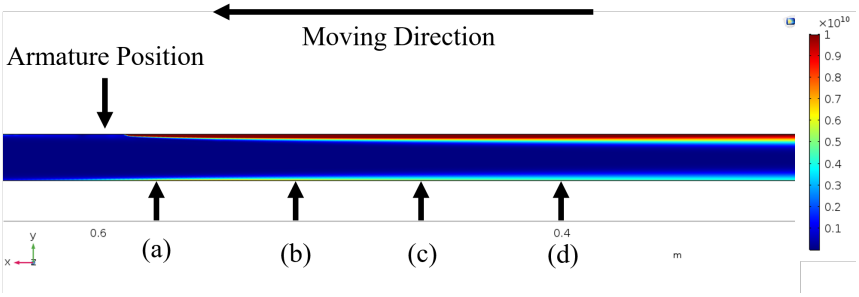

Figure 3.7: The current density distribution in the middle surface of the rail when the armature has 1200 m/s speed. The color legend is for the current density only and its unit is $\mathrm{A/m^2}$.

The rails middle surface is demonstrated with black lines in the rail cross sections in the same figure. An important argument that can be extracted from Fig. 3.8. is the current density distribution is not homogeneous through rail height, which is also indicates that the error comes from the 2-D approximation of R_{vse}. The current density distribution, which is calculated from 2-D transient/quasi-transient FEM models, is similar to the current density distribution at the rails middle surface only.

3-D Q-T FEM analysis showed that the current narrowing phenomenon due to VSE is more dominant in the x-y plane (z = 0) direction of the rail which is also marked with black lines. 2-D approximation modeled the system like it is infinitely high and identical; therefore, the VSE is considered uniform across to z axis. This result causes overestimation of $\mathrm{R_{VSE}}$ when the 2-D approximation is applied.

3.1.4 3-D Hybrid FEM

Many mesh elements are required as EMLs tend to high aspect ratio due to longer rails considering their cross-section. Partial rail modeling is a solid strategy to reduce computational load. Lumped circuit parameters can be used to represent rail portions that are not modeled in FEM geometry. The armature is located at the pre-load distance. The hybrid FEM model has a stationary armature. Consequently, the current

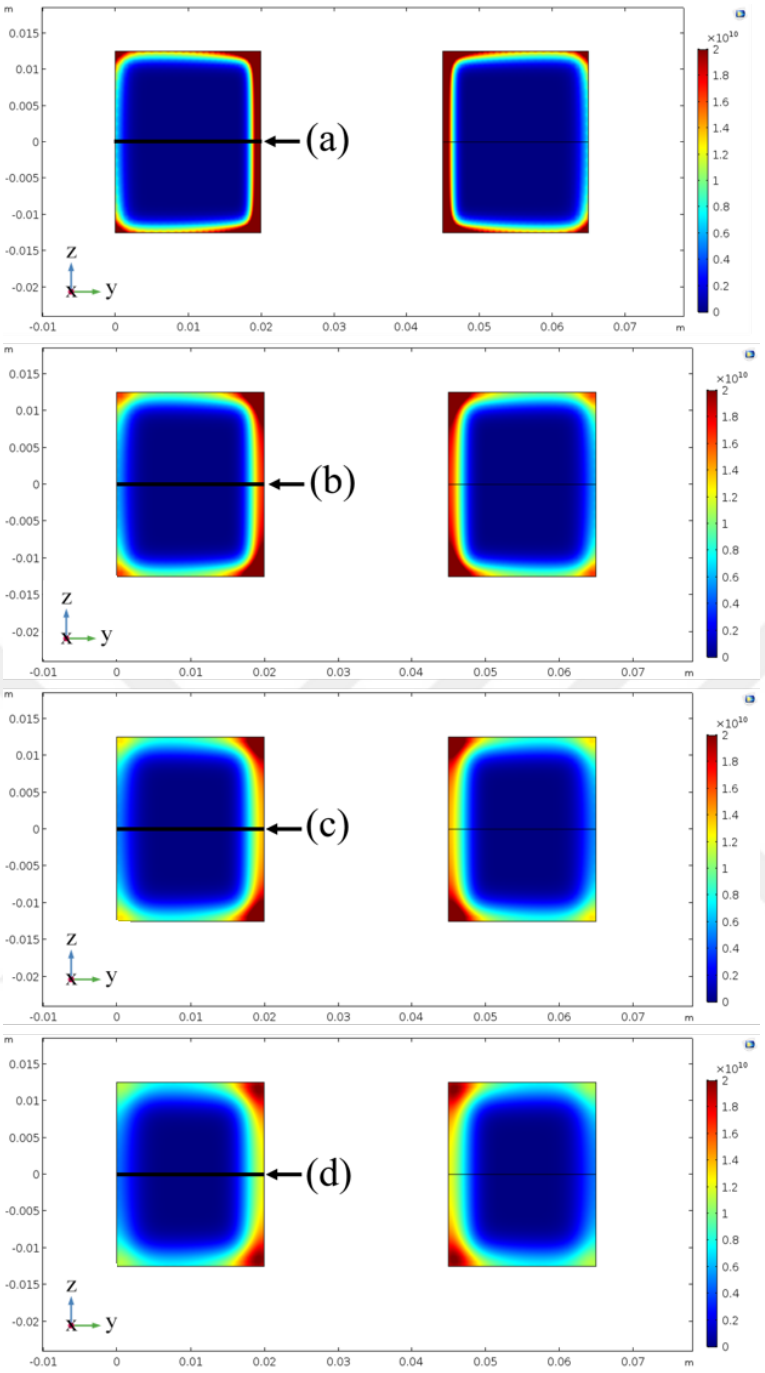

Figure 3.8: Current density distribution in rails with various rail cross-sections. The color legend is for the current density only and its unit is $\mathrm{A/m^2}$. Small letters represent the cross-section points demonstrated in Fig. 3.7.

distribution of the rails did not restrict due to VSE. The structure of the hybrid model, which we used, is demonstrated in Fig. 3.9.

The current density distributions in the rail when 3-D static and 3-D quasi-transient

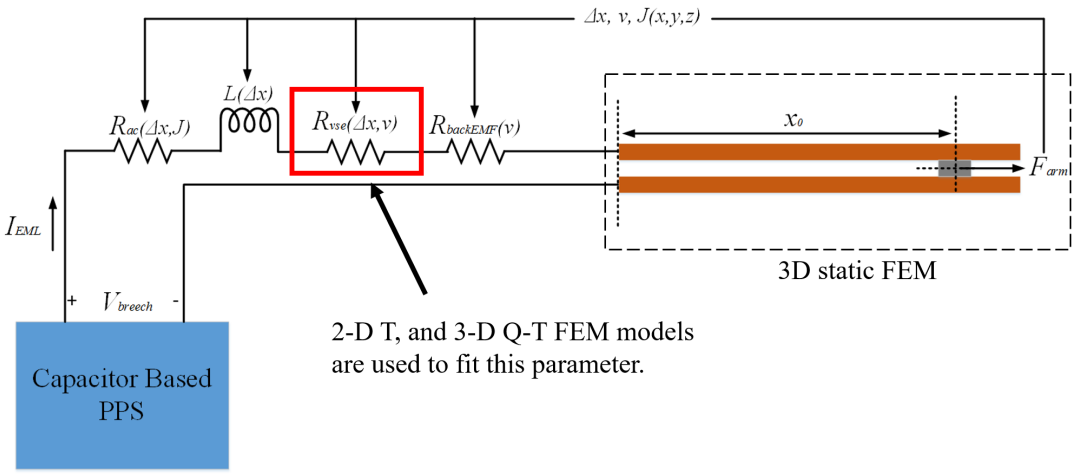

Figure 3.9: Hybrid FEM model used to simulate EMLs.

methods are used are illustrated in Fig. 3.10. The physical effects such as inductance and resistance variations due to armature movement are added to the simulation environment using lumped parameters. One of the mentioned physical effects is VSE resistance, which is denoted as R_{vse}, which is calculated from 2-D transient and 3-D Q-T analysis.

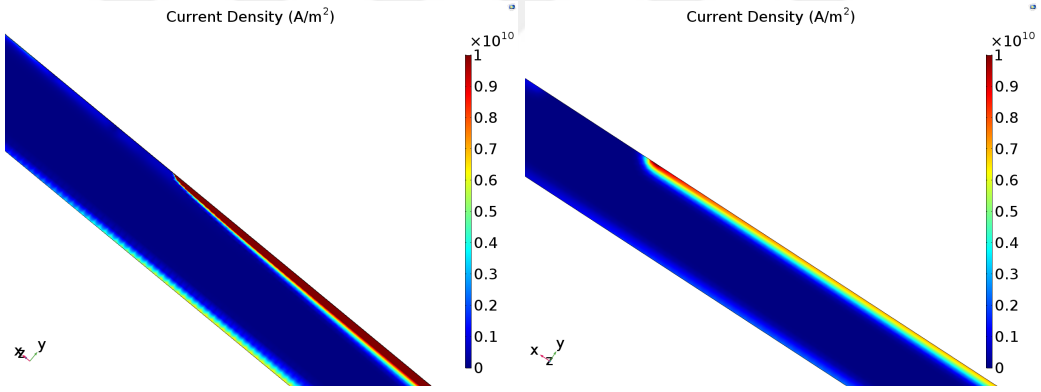

Figure 3.10: The current density distribution (A/m^2) in rail 3-D Q-T simulation (left) and static armature simulation (right). The Q-T analysis is made with an armature which has 1000 m/s velocity.

Other lumped parameters which we used to model the rail portion which related with armature regions are defined as exterior inductance, L_{ext} interior inductance L_{int}, AC resistance R_{ac} and back EMF resistance R_{emf}. L_{ext} is used to model inductance contribution in the air region between rails. However, L_{int} is used to model inductance contribution in the rails and air region between rails, excluding the exterior region.

Total inductance contribution due to p amount armature movement can be modeled, to sum up, that inductance (1).

$$L(t) = p(L'_{int}(t) + L'_{ext}(t)) \tag{3.2}$$

Back EMF resistance, $\mathrm{R_{backEMF}}$ formulation can be extracted from (3.2) to (3.5). EML can be considered as single turn coil. Therefore, linkage flux $\lambda(\mathrm{t})$ can be calculated from the inductance and rail current $\mathrm{I(t)}$.

$$\lambda(t) = L(t)I(t) \tag{3.3}$$

$$\mathcal{E} = \frac{d\lambda(t)}{dt} = \frac{dL(t)}{dt}I(t) + L(t)\frac{dI(t)}{dt} \tag{3.4}$$

$$\mathcal{E} = R_{backEMF}I(t) + L(t)\frac{dI(t)}{dt} \tag{3.5}$$

Back EMF due to armature movement is modeled as a resistance. Although it behaves as a voltage source, this assumption, from a mathematical perspective, does not pose a problem. $\mathrm{R_{ac}}$ can be calculated using the joule loss in the rail portion volume *V*. In (3.6), the resistivity of the rails is denoted as ρ_{rail}. $\mathrm{J_{rail}}$ and $\|.\|$ represents the current density inside the rails and $\mathrm{l_2}$ norm, respectively.

$$R_{ac} = p\frac{1}{I(t)^2}\iiint_V \rho_{rail}\left\|J_{rail(t)}\right\|^2 dV \tag{3.6}$$

The only lumped parameter which can not be computed directly from the hybrid FEM model is $\mathrm{R_{vse}}$. This parameter is imported from the studies which were done with 2-D transient and 3-D quasi-transient methods. Since all the other parameters are kept constant, the error that comes from $\mathrm{R_{vse}}$ calculations is directly transferred to the outputs of the hybrid FEM simulations. We avoided full discussion of the 3-D Hybrid FEM model since we do not want to duplicate with previous work. Interested readers can access detailed discussion about other parameters in and [21] and [37].

3.2 Methodology of the conducted work

The block diagram of the conducted work is shown in Fig. 3.11. Three different simulation models are developed, which are explained in the previous subsections in detail. In the analysis subsection, velocity-dependent VSE resistances are fitted with given velocity sample v, using two different models; 2-D transient and 3-D Q-T FEM. The fitted resistances are added to 3-D hybrid FEM, excited with PPS. The purpose of the hybrid model is to enhance the overall simulation-test accuracy [37]. It should be noted that the hybrid models objective is to increase simulation-experiment accuracy as well as creating a figure of merit that is used to compare performances of VSE resistances obtained by 2-D and 3-D analysis.

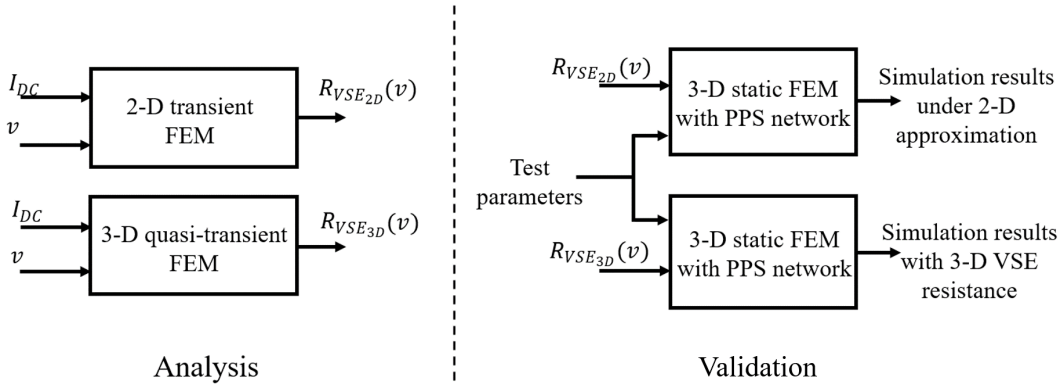

Figure 3.11: The methodology used to investigate the accuracy of 2-D approximation on VSE resistance.

3.2.1 Analysis

Extraction VSE resistance value from simulations has two parted procedure. Firstly, the 2-D transient FEM model is used to simulate different constant armature velocities. DC excitation is used in this part of the study. Secondly, obtained resistance values are decomposed into two parts; steady and transient parts. These parts are then used to fitting functions [37]. The identical procedure is employed for 3-D Q-T FEM as well.

3.2.2 Validation

Finding a figure of merit for VSE resistance calculation is the primary goal of the validation section. In this regard, these fitted lumped parameters are imported to the 3-D hybrid FEM model. To ensure the precisions of the methods, several experiments are conducted, and empirical data is collected. Then these launch experiments are simulated.

3.3 Results

In this section, the results of the VSE fittings and their performance are presented. VSE resistances exploited by the 2-D transient FEM model for several speeds are shown In Fig. 3.12. The result confirms that both transient and steady VSE resistance levels boost with the armature speed. Furthermore, R_{vse} values, which are received by 3-D Q-T simulations, are demonstrated in Fig. 3.13. The same trend is observed in terms of both transient and steady parts.

It should be noted that R_{vse} values are computed between 0.2- and 0.5-m ranges. Rail portioning is essential in EML simulations as the rail lengths tend to be much higher sized, considering the rail cross-section. Such a strategy decreases computational load effectively. As they exhibited a linear relationship with rail position, we extrapolate them for other ranges.

After exploiting lumped parameters, including R_{vse}, which obtained 3-D Q-T and 2-D transient FEM results, the hybrid simulation model is tested with experimental results to investigate the differences. The parameters of EMFY-1 and EMFY-2 experiments are shown in Table. 3.3. The rail currents are compared to evaluate accuracy of R_{vse} fitting, as it is a significant contributor to the total EML resistance. The results of the 3-D Hybrid FEM simulations where 3-D Q-T and 2-D transient methods used for R_{vse} and experimental results are compared in Figs.3.14- 3.17. The results show that the 3-D Q-T method is the most consistent with experimental results.

Experimental results can be used to explain the overestimation of R_{vse} with the 2-D approximation. The EML can be reduced as a passive RL circuit at its later stages

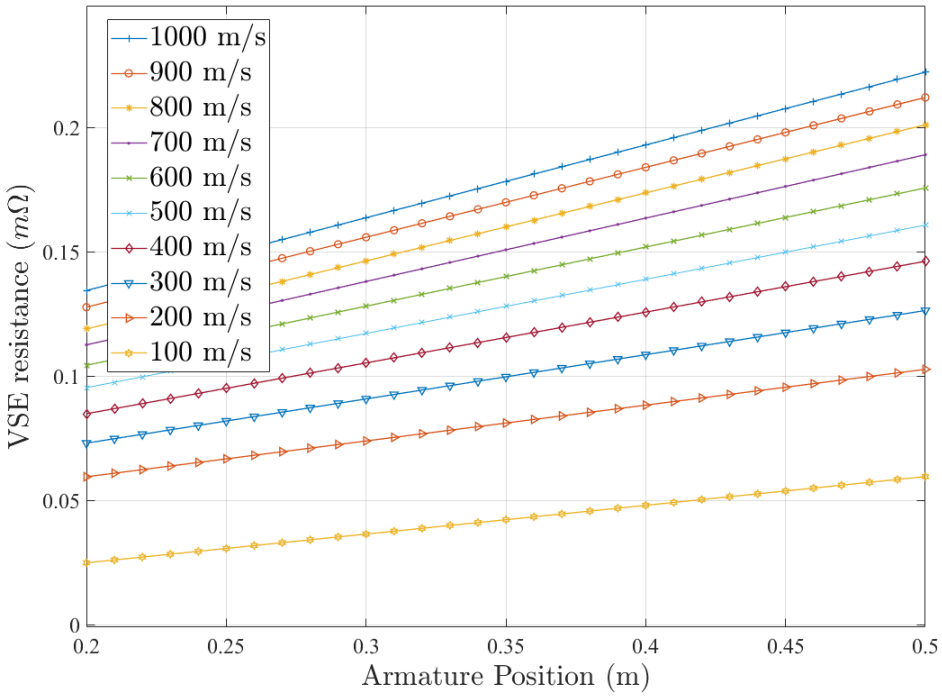

Figure 3.12: 2-D transient simulation results for VSE resistance with respect to armature position graph for armature velocities from 100 m/s to 1000 m/s.

Table 3.3: Parameters of EMFY-1 and EMFY-2 Experiments

	EMFY-1		**EMFY-2**	
	Exp. A	**Exp. B**	**Exp. C**	**Exp D.**
Initial Electrical Energy (kJ)	750	625	1227	3241
Launch Package Mass (g)	41.4	41.6	932.0	1033.2
Capacitor Voltage (V)	3560	3250	4000	6500
Armature Exit Velocity (m/s)	2174	1973	627	1020

of the launch. The reason is that all PPS units are fired, they are discharged. All capacitors are disconnected from EML electrically, as thyristors are ON state, diodes are in free-wheeling. This can be seen in Fig. 3.18. At that point the rail current decay rate depends only on the EML inductance, L_{EML}, and resistance, R_{EML}. Due to the potential overestimation of the R_{vse}, the 2-D transient simulations have faster decay than experimental results. The discrepancy at the late stage of the experiments associates with R_{vse} dominance at the late stage of the launch as armature velocity continuously increases.

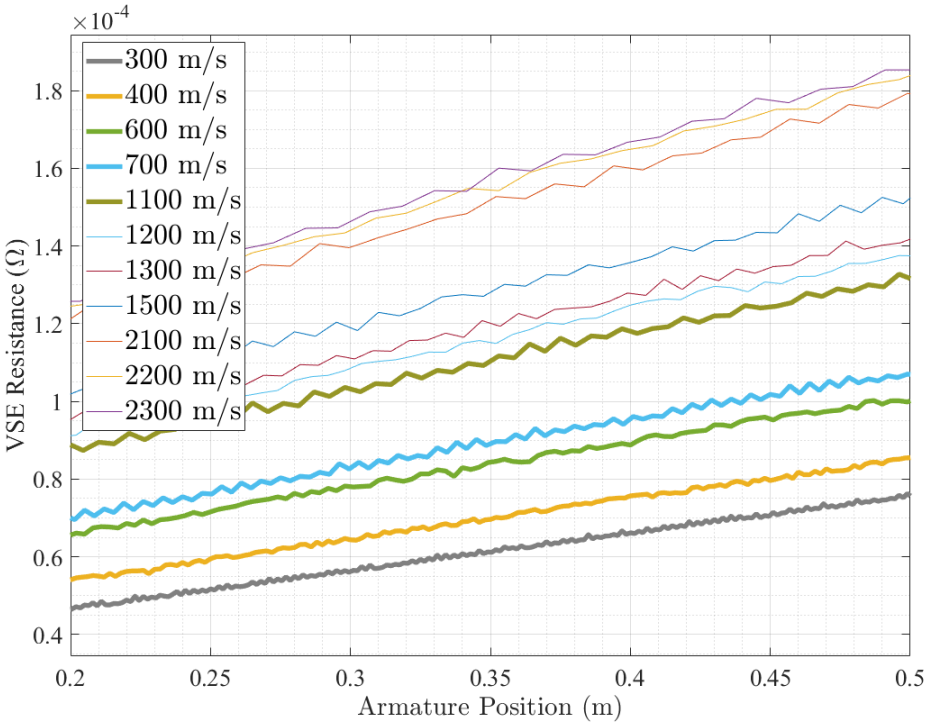

Figure 3.13: 3-D Q-T simulation results for VSE resistance with respect to armature position graph for armature velocities from 300 m/s to 2300 m/s.

Even though VSE resistance can be exploited by Q-T strategy, it is important to note that there are some restrictions. Firstly, the armature cannot be analyzed in detail due to geometry limitation. The conductivity function is moving pulse-shaped. It is challenging to write a time-dependent and a complex shaped conductivity function. For that reason, the armature is modeled as a rectangular prism, as shown in Fig. 3.19. Another restriction is that the time-dependent solver convergence. To prevent sudden conductivity jumps between mesh elements, time-steps are locked at a specific value. Considering the armature velocities, these time steps are extremely fine which increases the computational time.

3.4 Conclusion

Comparison between 2-D transient and 3-D Q-T FEM in terms of VSE modeling is exhibited in this study. The Q-T method is utilized to model the armature motion in 3-D. VSE is targeted in these models. The exploited VSE resistances are employed

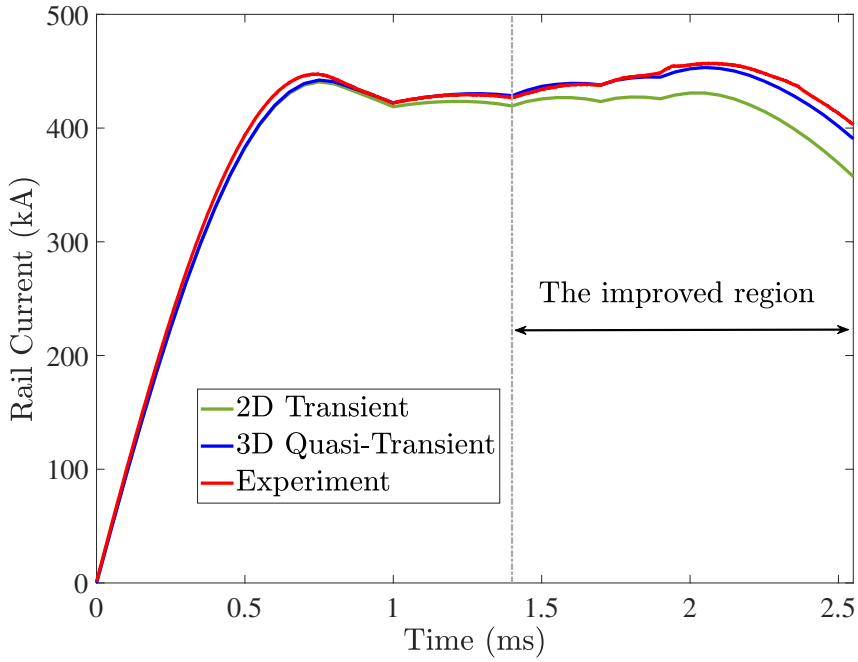

Figure 3.14: Simulation and experimental results for the rail current of the experiment-A with EMFY-1

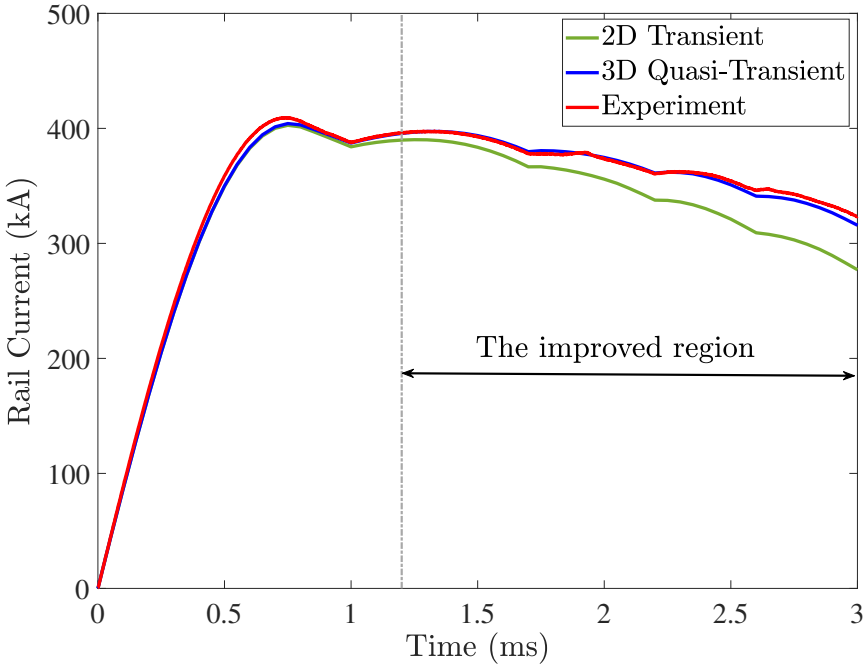

Figure 3.15: Simulation and experimental results for the rail current of the experiment-B with EMFY-1

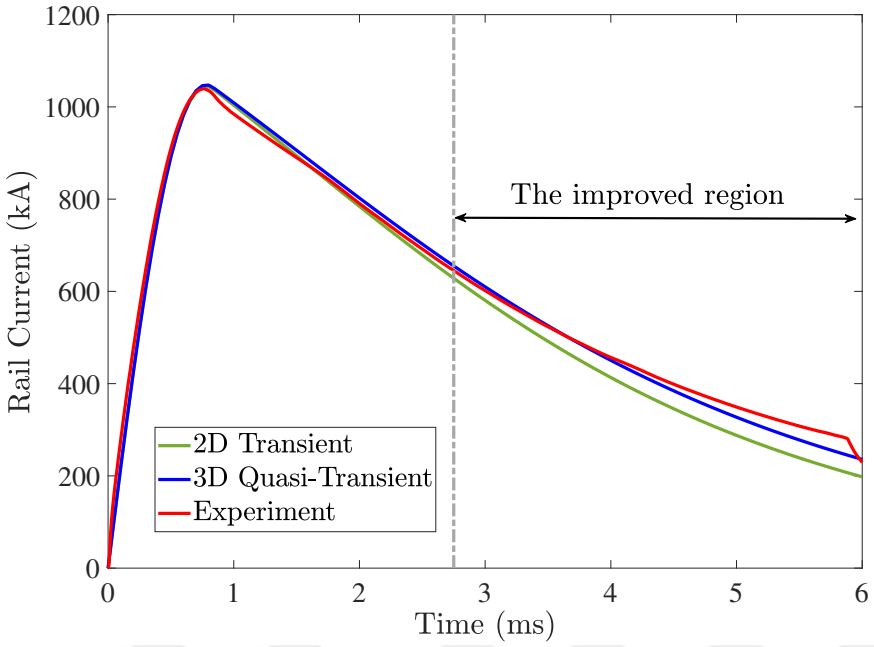

Figure 3.16: Simulation and experimental results for the rail current of the experiment-C with EMFY-2

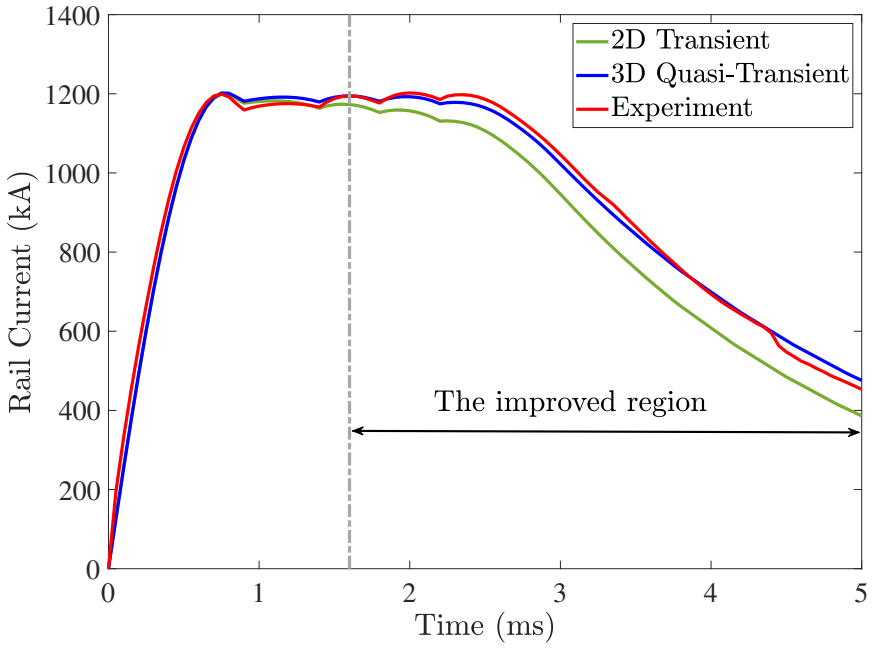

Figure 3.17: Simulation and experimental results for the rail current of the experiment-D with EMFY-2

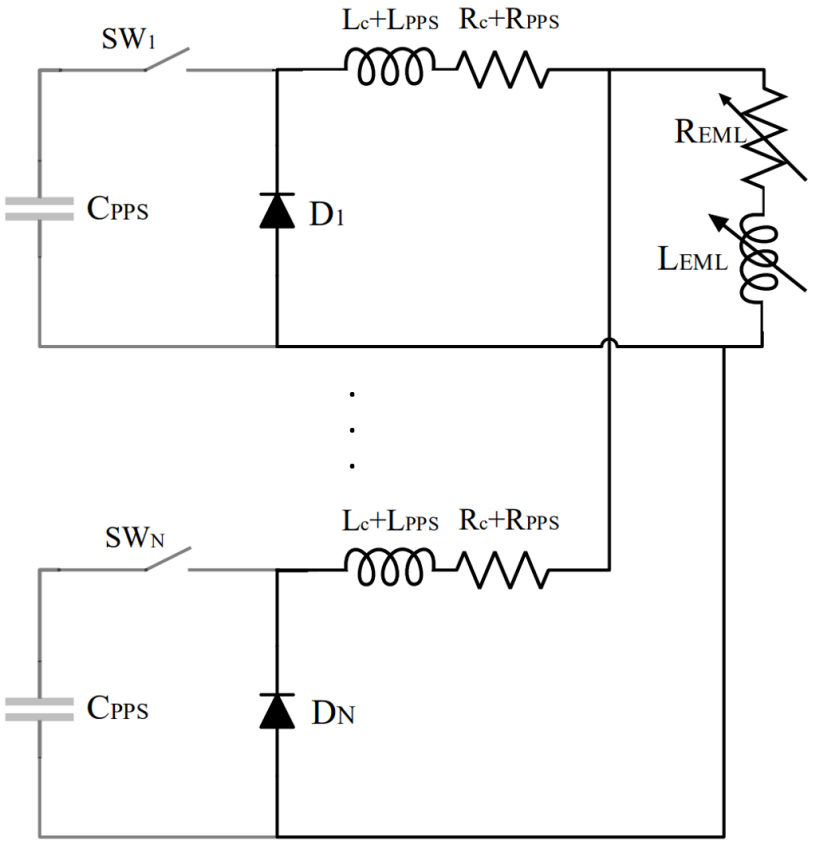

Figure 3.18: The circuit schematic of the last stage of the launch. Disconnected units are demonstrated using gray color. $\mathrm{R_{PPC}}$ and $\mathrm{L_{PPC}}$ represent the PPS resistance and inductance, respectively. $\mathrm{R_c}$ and $\mathrm{L_c}$ represent cable resistances and inductances.

into hybrid FEM-lumped model. Hybrid-FEM model is used to evaluate the accuracy with the empirical data obtained from launch experiments. The following conclusions are reached.

1. The Q-T method can be used model VSE in commercial FEM codes. 2-D transient and Q-T FEM give uniform current density distribution in the rails.

2. The hybrid FEM model reduces the computational burden of EMLs, such as the number of mesh elements and the requirement of the armature motion in the simulation. Although the field distribution at the sliding contact does not contain the current narrowing phenomenon, the VSE's resistive effects are added to the simulation environment, which improves losses and efficiency calculations.

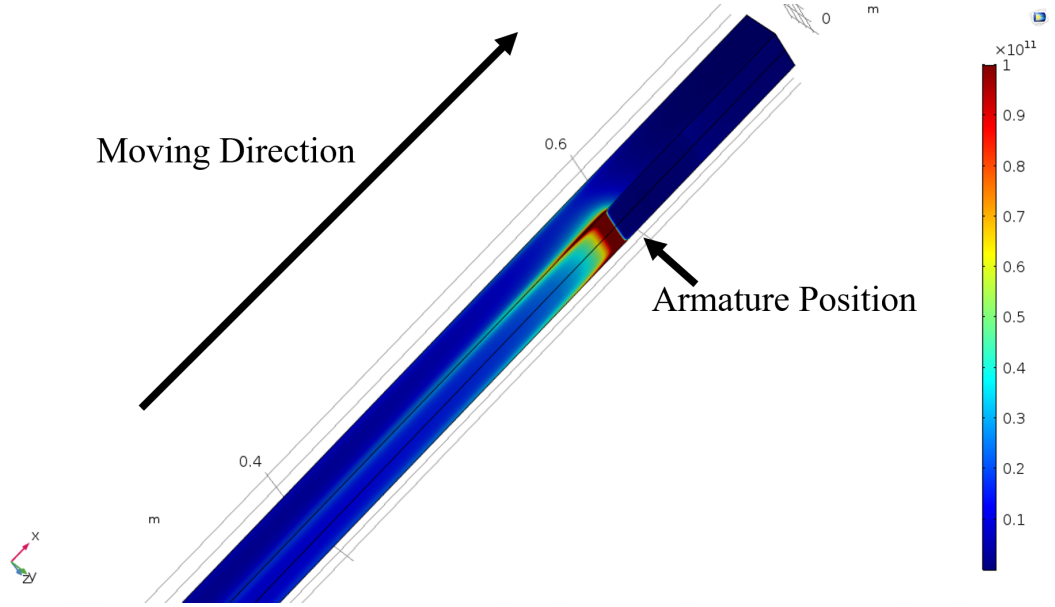

Figure 3.19: The current density distribution (A/m^2) in the rail with 3-D Q-T model. The armature modelled as rectangular prism.

3. The 2-D model overestimates VSE resistance. The reason for that is the current narrowing phenomena occur in the middle of the rail more dominantly. 2-D approximation assumes that the current distribution is identical in all rail height directions. However, this is not the case in the actual rail current distribution.

The study revealed that the exploited VSE resistance is a essential lumped parameters for the EML simulations. The proposed method give us the oppurtunity to improve the accuracy considering the empirical results. It is important to note that this study is applicable with other EMLs, electromagnetic actuators where VSE has a dominant effect on their conductors.

CHAPTER 4

TRANSIENT INDUCTANCE AND BACK-EMF CALCULATIONS OF ELECTROMAGNETIC LAUNCHERS

This chapter presents a hybrid 3-D FEM coupled electrical circuit simulation method for EML. This model has empowered with transient inductance variations and a new electromotive force (EMF) calculation method. The proposed method introduces not only the EMF related to the armature motion but also the EMF due to rail current distribution change. The study is unique in that sense, as the previous studies focus only on the EMF sourced by armature motion. This phenomenon becomes dominant when larger rail widths are utilized. The proposed method is implemented with a control method where the novelties are excluded. The effectiveness of the model is verified experimentally with two different EMLs developed by ASELSAN [38]. As two different EMLs is utilized, the discussion about the new EMF method is enlarged considering the different rail dimensions.

The 3-D geometry which is used in FEM models is shown in Fig. 4.1. This geometry refers to the EMFY-2 launcher. The armature is held fixed at the pre-load position during the FEM simulation. Armature motion increases the total inductance and the resistance of the EML. A lumped circuit is added to the model in this regard. The point of such addition is adding the electromagnetic effects of the armature motion into a static FEM model. This lumped circuit is coupled with kine-mechanical equations whose shown in (4.1), and (4.2). The main driving force of the armature is Lorentz force which a volume integration, where $\mathrm{V_{arm}}$ denoted as the volume of the armature, can obtain;

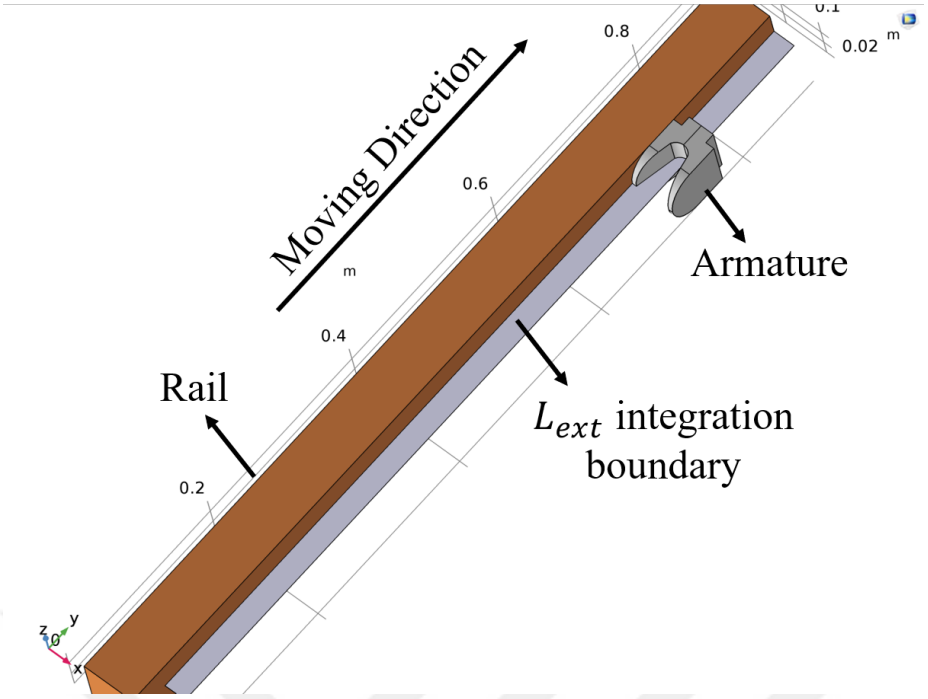

Figure 4.1: The geometry which is used for 3D FEM analysis of EMFY-2. Half symmetry is used for all FEM simulations. The integration boundary for $\mathrm{L_{ext}}$ is demonstrated. However, the armature is modeled as whole for visual purposes.

$$\vec{F}_{arm} = \iiint_{V_{arm}} \vec{J} \times \vec{B}\, dV \tag{4.1}$$

$$\Delta x = \int_0^t \int_0^t \frac{\vec{F}_{arm}}{m_{arm}}\, dt\, dt \tag{4.2}$$

$\Delta \mathrm{x}$ is the displacement of the armature from its initially pre-load position, $\mathrm{m_{arm}}$ is the mass of the armature. The parameters used in the circuit simulation and their roles in the overall model are summarized in the following sections.

4.1 EMF calculation

The EML can be considered a one turn coil with a time-dependent geometry as in (4.3).

$$\Phi(t) = \lambda(t) = L(t)I(t) \tag{4.3}$$

The electromotive force (EMF) can be calculated using Lenz's Law as in (4.4).

$$\epsilon(t) = \frac{d\lambda(t)}{dt} = \frac{dL(t)}{dt}I(t) + L(t)\frac{dI(t)}{dt} \tag{4.4}$$

The first term in (4.5) is related to the transient inductance of the system. When the armature is considered as the only moving part, the total inductance of the system increases only with armature movement with a single direction. Therefore, there is an EMF related to this transient inductance variation. Then, the back-EMF part can be reconstructed as in (4.7) and (4.8) in which velocity denoted as v is the armature velocity and L' is the inductance gradient. Although EMF is not physically a resistance, it can be used in a mathematical model to represent the EMF voltage.

$$\epsilon(t) = (\frac{d}{dx}\frac{dx}{dt}L(t))I(t) + L(t)\frac{dI(t)}{dt} \tag{4.5}$$

$$\epsilon(t) = vL'(t)I(t) + L(t)\frac{dI(t)}{dt} \tag{4.6}$$

L' can be derived using the Lorentz force on the armature as followings (4.7), and (4.8);

$$\vec{F}_{arm} = \frac{1}{2}L'I^2 \tag{4.7}$$

$$L' = \frac{2\vec{F}_{arm}}{I^2} \tag{4.8}$$

Then the first part of the EMF equation can be used to model $\mathrm{R}_{\mathrm{backEMF}}$ as given in (4.10).

$$\epsilon(t) = R_{backEMF}I(t) + L(t)\frac{dI(t)}{dt} \tag{4.9}$$

$$R_{backEMF}(t) = vL'(t) \tag{4.10}$$

As mentioned before, (4.10) is constructed considering inductance variation occurs only one direction, the direction of the armature motion. However, L' does not necessarily equals to $\frac{\partial L}{\partial x}$. If the inductance has variance in y direction also, then L' becomes

as in (4.11).

$$L' = \frac{\partial L}{\partial x} + \frac{\partial L}{\partial y} \tag{4.11}$$

It is important to note that the kine-mechanical equations do not use L' in the (4.11). The reason is that the armature is accelerated only by the force at the x-direction. The second term in the equation is the voltage on the inductance due to rail current transient. This inductance can be further divided into two parts: the interior inductance L_{int} and the exterior inductance $\mathrm{L_{ext}}$. Integration surfaces which we used to calculate this inductance in the previous study [37] are demonstrated in Fig. 4.2. These boundaries will be examined in more detail in this chapter in the subsequent section.

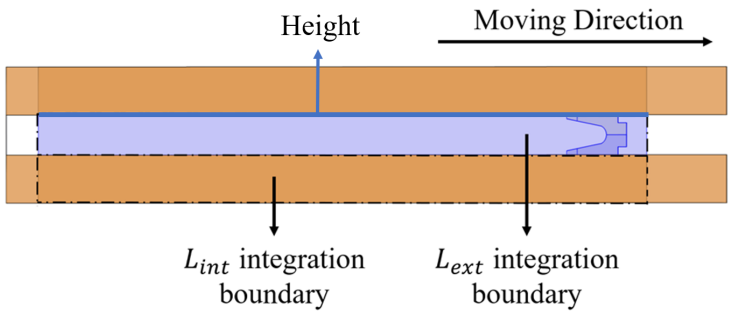

Figure 4.2: Integration boundaries which are used for $\mathrm{L_{ext}}$ and L_{int} calculations in the previous study [37]. Inductance gradients, L'_{ext} and L'_{int} is calculated dividing the calculated inductance values with the height of the integration boundaries.

The armature displacement is the only term that contributes inductance change when the $\mathrm{R_{backEMF}}$ is determined using (4.10). Nonetheless, this is not the only mechanism. Rail currents also move laterally due to their diffusion process. The current path in the rails moves with time. This variation in the rail current path is responsible for an inductance change; a change in the inductance created an EMF term. Particularly for larger launchers, the phenomenon of the rail inductance transient becomes more prevailing as the more extensive lateral rail current displacement occurs. Both EMF terms should be included in the model. For that reason, EMF resistance should be

regarded as in (4.12) rather than (4.10).

$$R_{backEMF}(t) = \frac{dL(t)}{dt} \tag{4.12}$$

The deviation of the equivalent current path in an EML is analogous with a coil that is deformed as shown in Fig. 4.3.

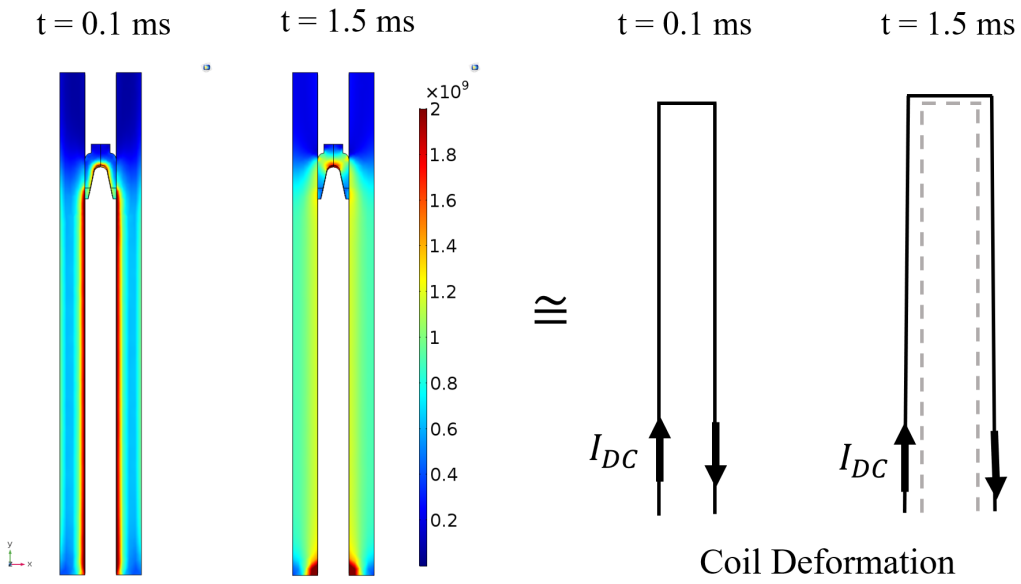

Figure 4.3: Coil deformation analogy. Transition from highly transient rail current to DC state can be considered as lateral deformation of a coil. Changing in the rail current path creates a transient inductance change which is also a source of EMF. The color legend is for the current density only and its unit is $\mathrm{A/m^2}$.

There exists an induced EMF when an AC excitation is applied. However, there are other ways to induce EMF. For example, even if a DC is applied to the coil, the deformation in the coil geometry still induces an EMF term. This situation is illustrated in Fig. 4.3.

Initial firings of the PPS units put rail current into a highly transient state. Thus, the rail current is concentrated at the edges regarding the skin effect. Nonetheless, the rail current leads into the DC state subsequent to its peak value and gets a more homogeneous distribution in the rail cross-section, excluding the near-armature region. Lateral displacement of the rail current due to the diffusion can be viewed as an ex-

pansion of a single turn coil. Thus not only the armature movement contribute to the EML inductance, but the lateral displacement does it also. Consequently, when the armature movement is recognized as the only source of EMF, the calculated EMF is less than the actual one.

EMF resistance calculations with and without transient rail inductance (which included lateral rail current movement) for EMFY-1 and EMFY-2 are exhibited in Fig. 4.4. It should be noted that the proposed model has higher EMF resistance than the EMF resistance calculated with the control method. The proposed one also includes the rail inductance change. The proposed method utilizes (4.10) to model EMF, whereas the control group employs (4.12). Both methods are use (4.8) for kine-mechanical calculations.

The rail thicknesses are presented in Table 3.1. The difference between the two EMF calculations is not significant at the EMFY-1 launcher. The reason is that the rail width of the EMFY-1 is less than EMFY-2. The lateral movement of the rail current does not induce as much inductance as in the EMFY-2 case. Thus, the phenomenon is more clearly visible in EMFY-2 calculations.

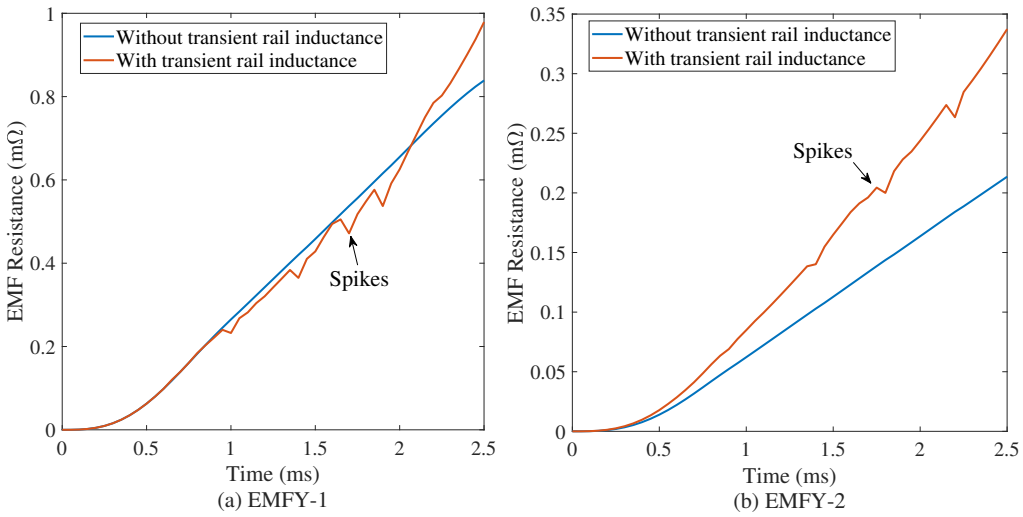

Figure 4.4: Comparisons of the two calculation methods of EMF resistance on EMFY-1 (a) and EMFY-2 (b). Spikes at the EMF resistance where transient rail inductance included comes from the discrete derivative operator in (4.12).

The inductance of the EML seen from the breech arises while the armature is moving

towards rails. Nevertheless, the 3-D FEM evaluates the inductance of the EML at the pre-load position only. The reason is the armature is located in its initial position (pre-load), and it is static throughout the simulation. Inductance increase due to armature motion reckoned to the simulation utilizing the lumped inductances. The difference between these inductances stands from their integration boundaries. The exterior boundary is located between rails, responsible for the magnetic flux integration between rails. $\mathrm{L_{ext}}$ can be computable with integration with the exterior boundary. On the other hand, the interior boundary is located inside the rail. Interior boundary is used to calculate L_{int}, which is then used to model the rail inductance with $\mathrm{L_{ext}}$. Both inductance gradients, which are determined from 3-D FEM, are utilized to calculate total EML inductance. The armature displacement, which is evaluated from kine-mechanical equations, is used with inductance gradients as in (4.13).

$$L(t) = p(L'_{ext}(t) + L'_{int}(t)) \tag{4.13}$$

In this part of the study, we developed two main contributions to inductance gradient calculation. The first one is about the methodology we used for lumped inductance calculation. We used two different methods to compute L_{int}, namely, the flux integration method and the stored energy method.

The flux integration method use a surface integral on the inductance related area to count the rail flux. Since the definition of the inductance is how much net flux linked with unit current, only one-sided magnetic field density vectors are integrated. Then the inductance is calculated using (4.14) where $\mathrm{A_{int}}$ is the area integration for the interior inductance calculation. The energy method uses the stored magnetic energy in the rails to compute inductance. The stored energy in rail is calculated as in (4.15) and (4.16) where $\mathrm{V_{rail}}$ is the volume of single rail.

$$L_{int}(t) = \frac{1}{I} \iint_{A_{int}} (B_z(t) > 0) B_z(t)\, dA_{int} \tag{4.14}$$

$$E_{stored}(t) = \iiint_{V_{rail}} \vec{H}(t)\vec{B}(t)\, dB = \frac{1}{2} L_{int}(t) I^2(t) \tag{4.15}$$

$$L_{int}(t) = \frac{2E_{stored}(t)}{I(t)} \tag{4.16}$$

However, these two methods give slightly different results as shown in Fig. 4.5. L'_{int} calculations diverge especially at the down-slope region of the rail current.

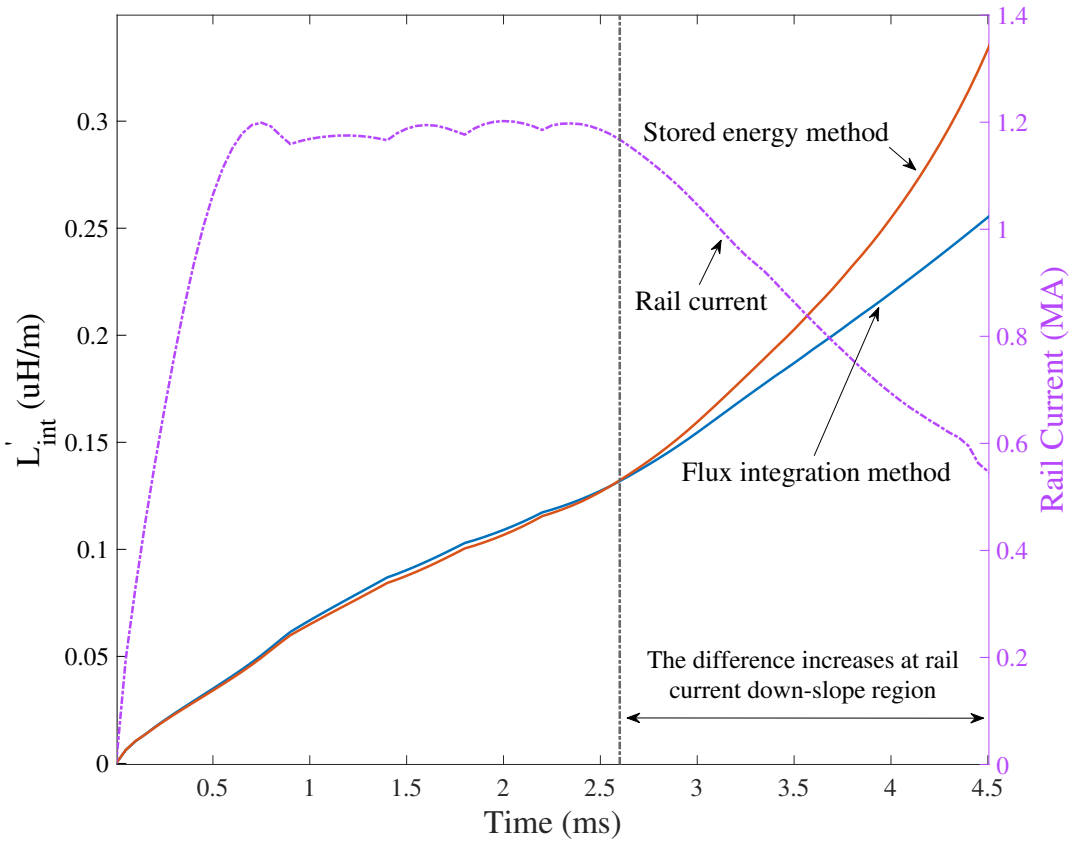

Figure 4.5: The comparison of L_{int}. EMFY-2 simulation model used in this calculations. Difference between two model increases especially at the down-slope rail current region.

This variation is explained in Fig. 4.6 using the current distribution and the magnetic flux density vectors. At t = 0.5 ms, current density is concentrated at the edges due to skin effect which is shown in Fig. 4.6a. Therefore, there is a small magnetic field density inside the rail, which makes L_{int} minimal. Then, rail current starts to go into low-frequency state at t = 1.5 ms, which is shown in Fig. 4.6b. Some of the magnetic flux density vectors in the rail close their loop through the air region. Therefore, when flux counting method is used, not only the rail inductance but also air inductance is

calculated. The part of the L_{int} that comes from the air region can not be calculated from the stored energy method since the volume integration includes only the rail.

It should be noted that both strategies for calculating L'_{int} are essentially proper, but there is a slight variation due to their description. For example, at t = 4.75 ms, the rail current has a down-sloped slope. Two electromagnetic effects are forming the current distribution at that phase. The first one is the skin effect due to the non-DC rail current. The second is the current diffusion from the edges to the rail inside. This transition is triggered due to rail current waveform turns into AC from DC. In both cases, L_{int} is still high due to the inner current density. Nevertheless, L_{int} value evaluated from the stored energy method is a bit misleading. In stored energy method, the current distribution at the edges contribute $\mathrm{L_{ext}}$ rather than L_{int}. The reason is a volume integration in (4.15) utilized for L_{int} calculation. The outer air region, interior, and exterior boundaries are demonstrated in Fig. 4.7.

Ceylan *et al.* [37] used the integration domain that is illustrated in Fig. 4.2. This boundary covers not only rails but also the armature domains. However, this integration boundary brings errors in inductance calculation when used in the lumped parameter calculation. The reason is that the targeted inductance parameters should be utilized to model the rail portions, which is not covered in 3-D FEM. It should be noted that rail lengths are extremely long, considering their cross-section sizes. It is unpractical to fully-model them. Hence, the current distribution should not be affected due to armature. The new integration area which excludes the armature is shown in Fig. 4.9. Integration boundaries are located far away from the armature intentionally. The new integration boundaries are shorter than the previous armature-included boundaries in the simulation. Such change inhibits the effects of lumped port (the regions where current excitations are provided) and the armature. Because the calculated inductance value is normalized with the length of the integration boundary, the length should be an invariant parameter for inductance gradient calculation. $\mathrm{L_{ext}}$ calculations with two different integration boundaries are shown in Fig. 4.8. The new boundary which excludes the armature give 12% deficit in $\mathrm{L_{ext}}$ calculation.

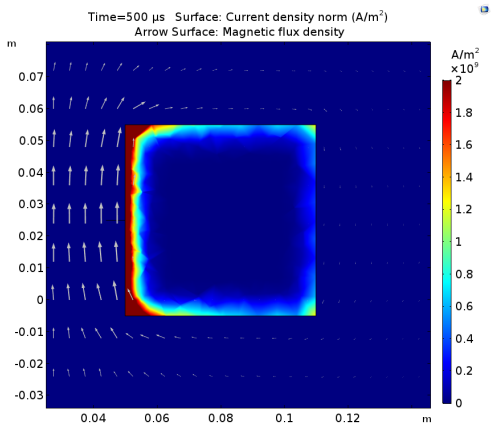

(a) t = 0.5 ms

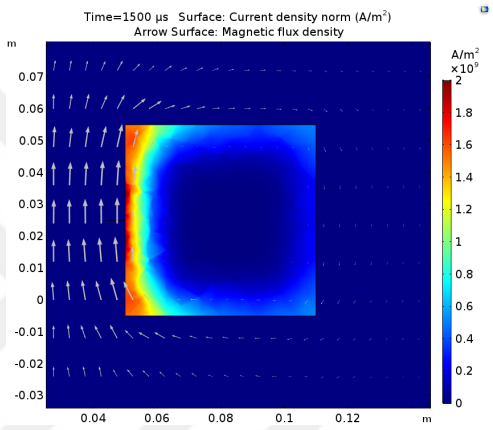

(b) t = 1.5 ms

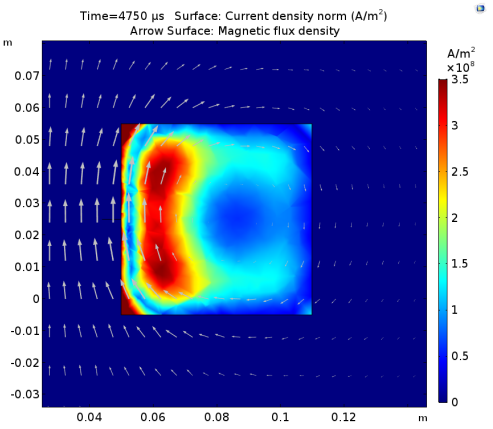

(c) t = 4.75 ms

Figure 4.6: Rail current distribution and magnetic flux density vectors throughout the launch. The color legend is for the current density only and its unit is $\mathrm{A/m^2}$. The rail current waveform is demonstrated in Fig. 4.5. a) 0.5 ms, b) 1.5 ms and c) 4.75 ms

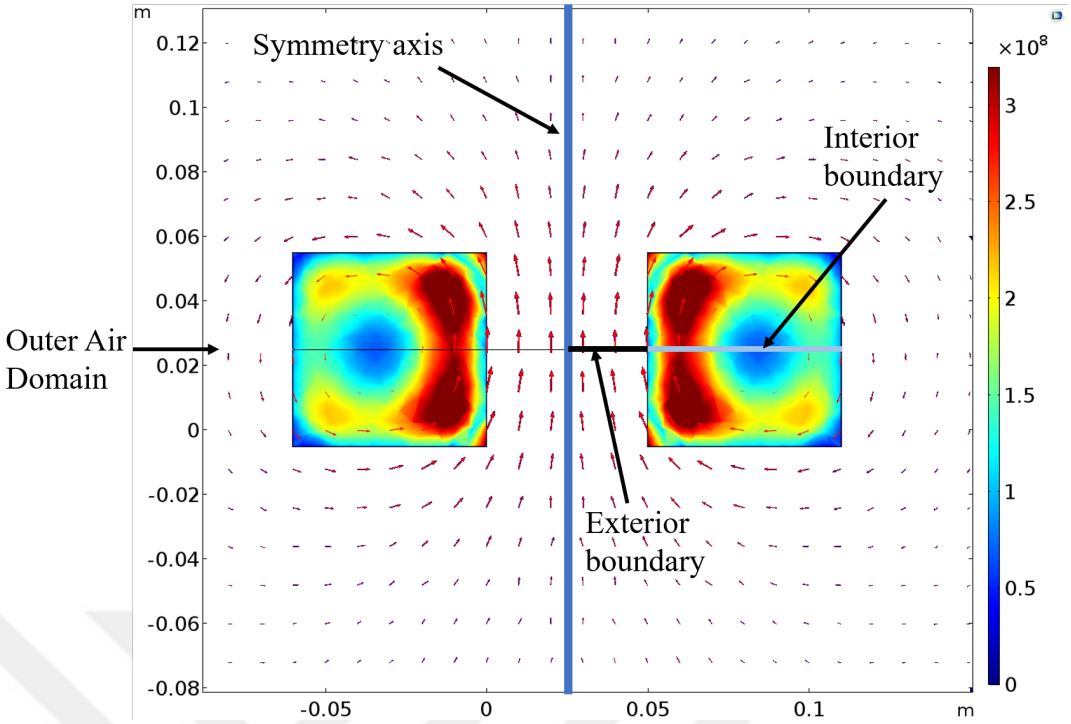

Figure 4.7: Definitions of the interior and exterior boundaries, outer air domains and the symmetry axis. The color legend is for the current density only and its unit is $\mathrm{A/m^2}$. There is a significant amount magnetic flux density around the outer air domain which is taken into account when the inductance are calculated.

4.2 Velocity skin effect modeling, R_{vse}

In the previous study [37], the 2-D transient FEM simulation is utilized to find VSE resistance, $\mathrm{R_{vse}}$. The reason is that the transient 3-D FEM analysis is difficult to converge for simulations of EMLs. The study was not conducted in 3-D, as it is challenging to converge simulations, especially the armature movement is required. In the proposed method, we used 3-D Q-T FEM simulations to fit $\mathrm{R_{vse}}$ rather than a 2-D approximation, or 3-D T FEM where the computational load is the limiting factor. As aforementioned, in Q-T FEM, the armature does not move, i.e., mesh elements of the armature are kept stationary. Nevertheless, the conductivity of the air-armature region is modified with time in the direction of armature motion to simulate the movement. In Fig. 3.4, the moving pulse-shaped armature-air conductivity function is represented. This conductivity function does not exactly reflect the armature fields due to the geometry simplification; it has a value to examine VSE.

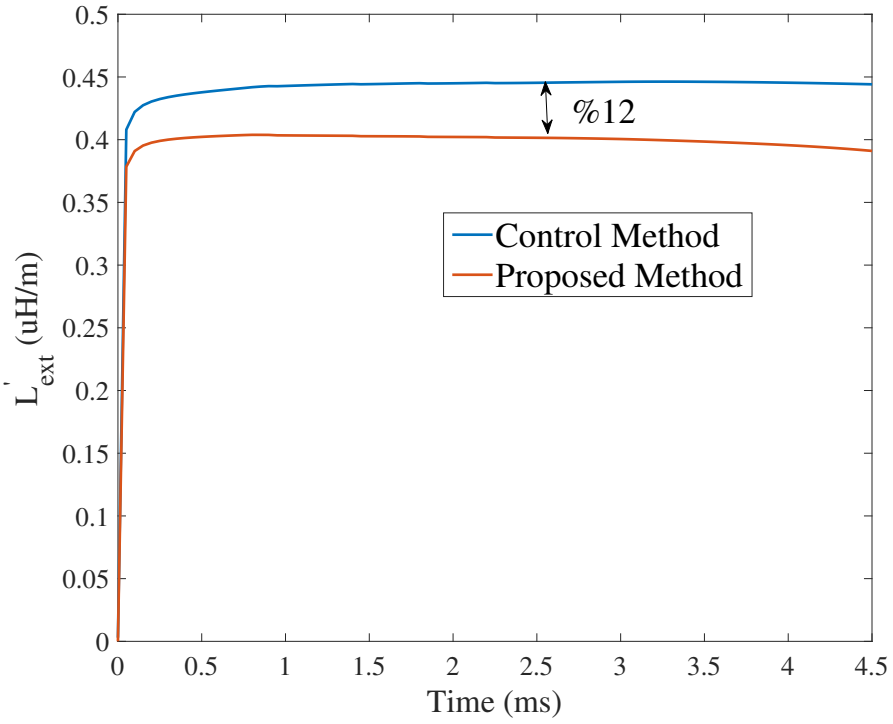

Figure 4.8: Comparison of L'_{ext} calculation methods. Control method found inductance gradient %12 higher since the domain includes armature rail interaction region. Integration boundaries which are used in the control method and the proposed method can be seen in Fig. 4.2 and Fig. 4.9 respectively.

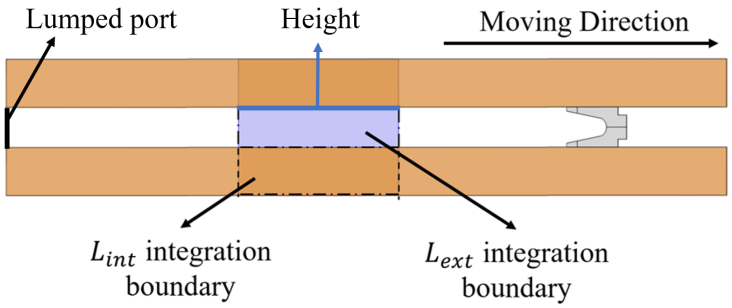

Figure 4.9: The new integration boundary for lumped inductance calculations.

The 2-D approximation of the R_{vse} overestimates the actual value. The reason is rooted due to the symmetry approach. The 2-D approximation pretends that the rails and the air have infinite height and that the current distribution is uniform across the axle of symmetry. However, the 3-D rail geometry has finite rail length. Thus, the distribution of the current and magnetic field on the axis of symmetry is not uniform.

Assuming an infinite rail height, the current clustering occurs up to the rail height, resulting in an overestimated VSE resistance calculation.

4.3 Results

In order to validate the hybrid model, four launch experiment results are used. The developed hybrid model includes transient inductance and EMF calculations, whereas there is also one control method. The proposed method regards improvements, whereas the control method is used to create a benchmark. Both EMFY-1 and EMFY-2 launchers are used in launch experiments. Two launch results of EMFY-1 and two launch results of EMFY-2 are represented. Differences between the proposed and control methods are listed in the following.

1. The proposed method utilizes (4.12) for $\mathrm{R_{backEMF}}$ calculation which includes the transient inductance related EMF. On the other hand, the control method employs (4.10), which only calculates EMF due to armature motion only.

2. Both the proposed and the control group methods practice the flux-integration method to determine lumped inductance parameters. Nevertheless, the proposed method uses an integration boundary where the armature is excluded (the armature is far away from the integration boundary), which is shown in Fig. 4.2. The control group uses an armature included boundary (the armature is near to the integration boundary), which is given in Fig. 4.9. Two integration boundaries dissociate each other in terms of the armature-rail interference on the inductance calculation regions.

3. The proposed method uses R_{vse} from 3-D Q-T analysis whereas the control group uses R_{vse} from 2-D transient analysis which used in [37].

Rogowski coils are utilized for rail current measurements for both EMFY-1 and EMFY-2 launchers. A high-speed camera is used to determine the muzzle velocity. Although the complete armature velocity curve is lack, muzzle velocity and armature exit time can be utilized together to verify the kine-mechanical equations of the

models. Experimental parameters of EMFY-1 and EMFY-2 are provided in Table 4.1.

.

Table 4.1: Parameters of EMFY-1 and EMFY-2 Experiments

	EMFY-1		**EMFY-2**	
	Exp. A	**Exp. B**	**Exp. C**	**Exp D.**
Initial Electrical Energy (kJ)	750	625	1227	3241
Launch Package Mass (g)	41.4	41.6	932.0	1033.2
Capacitor Voltage (V)	3560	3250	4000	6500

The simulations and experiment rail current waveforms comparison for EMFY-1 launcher is given in Figs. 4.10 and 4.11. EMFY-2 experiments are compared with the simulations in Figs. 4.12 and 4.13.

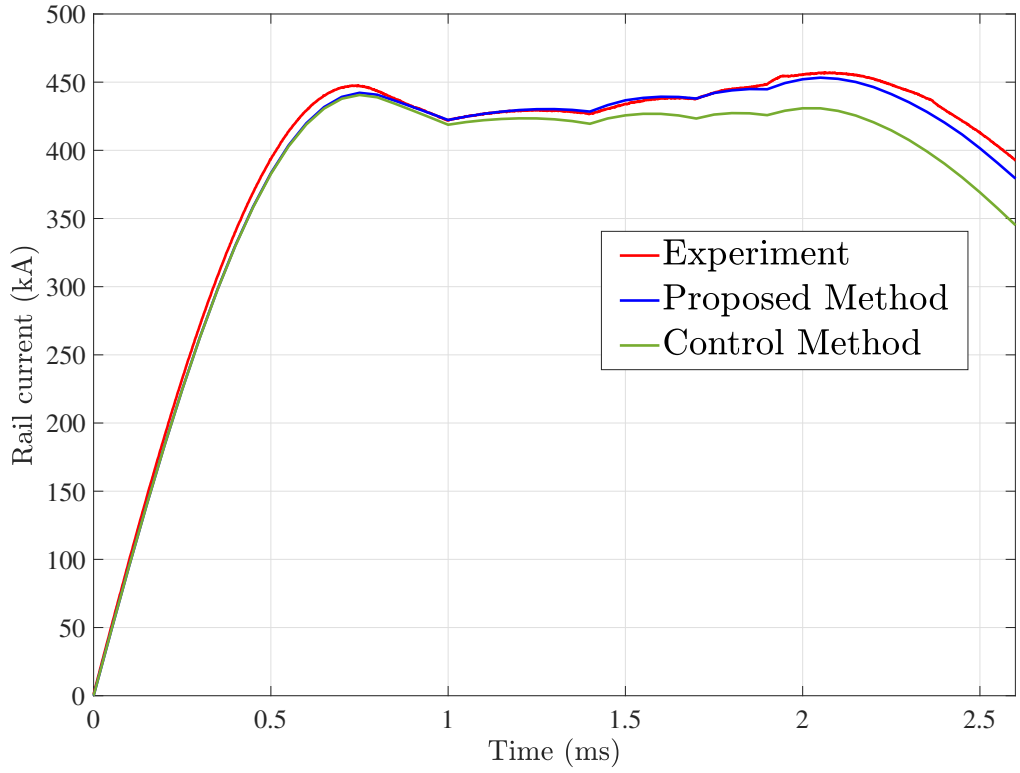

Figure 4.10: Simulated and experimental rail currents of the experiment-A. EMFY-1 launcher is used in this experiment.

The root mean square error (RMSE) of the rail current waveforms which is obtained from simulations and experiments is given in the table 4.2.

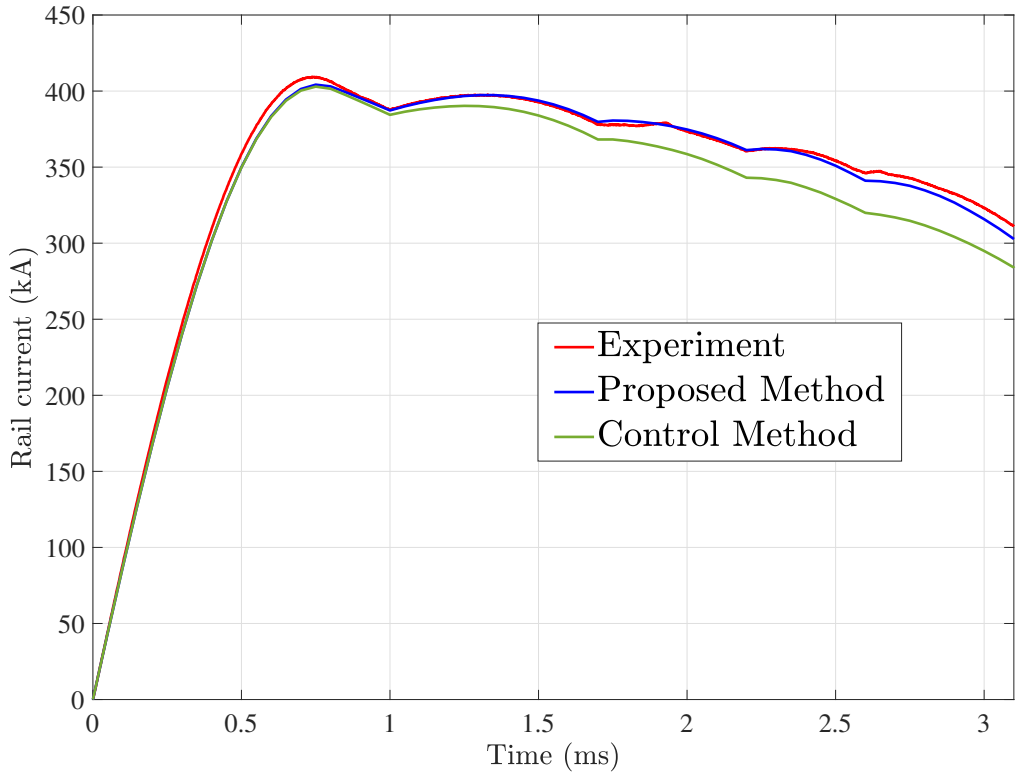

Figure 4.11: Simulated and experimental rail currents of the experiment-B. EMFY-1 launcher is used in this experiment.

In order to enumerate the error between rail current waveform, we used RMSE, which is given in (4.17). n, $\bar{x}$, and x represent the amount of the sampled data, simulated value, and experimental value, respectively. The results of the proposed method, control method, empirical results, and improvement ratios (IRs) are presented in Table 4.3.

We used improvement ratio (IR) to compare two methods. It uses the mean absolute error (MAE) of measurement parameters. These measurement parameters are armature exit time, muzzle velocity, and muzzle current.

MAE and IR are defined in (4.18) and (4.19), respectively. $x_{control}$, $x_{proposed}$ and $x_{represent}$ represent the value evaluated from the control method, the value evaluated

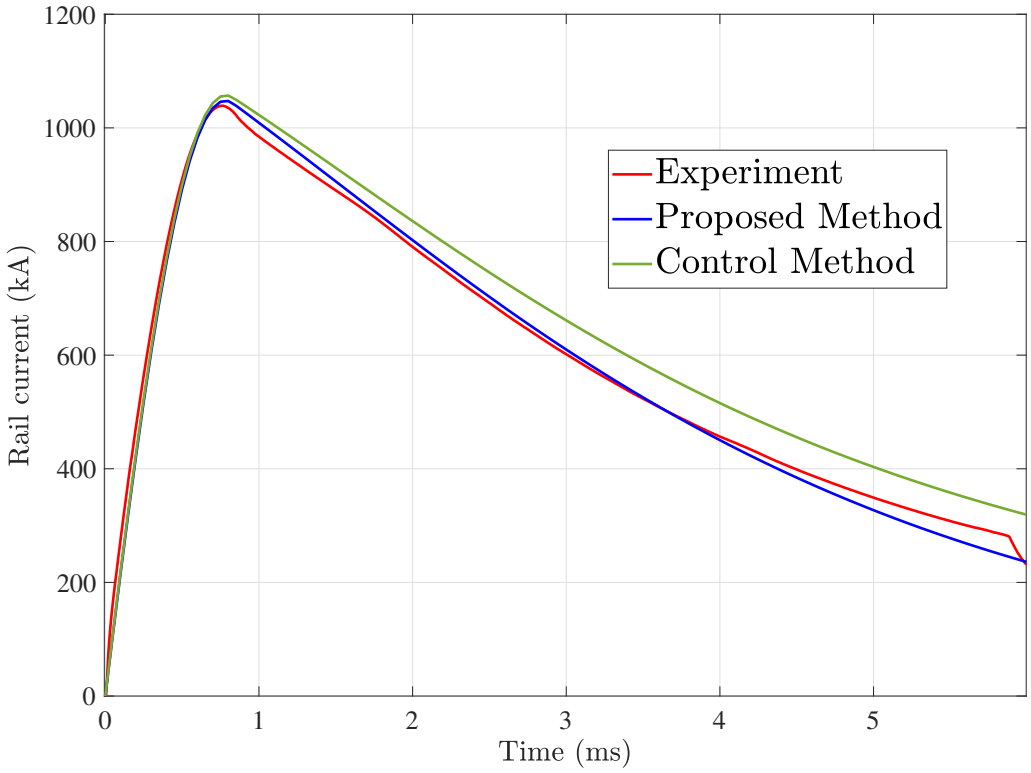

Figure 4.12: Simulated and experimental rail currents of the experiment-C with EMFY-2 launcher.

from proposed method and experimental result, respectively.

$$RMSE = \sqrt{\frac{1}{n}\sum_{i=1}^{n}\left(\hat{x} - x\right)^2} \tag{4.17}$$

$$MAE = |\hat{x} - x| \tag{4.18}$$

$$IR = \frac{MAE(\hat{x}_{control}, x) - MAE(\hat{x}_{proposed}, x)}{x} \tag{4.19}$$

The proposed method proved that transient inductance and EMF calculations are improved. For this regard, simulation-experiment accuracy is enhanced by 3.49% on average. Furthermore, empirical rail current waveforms and simulation results agree more. Thus, the inductance and resistance parameters of the EML are obtained better

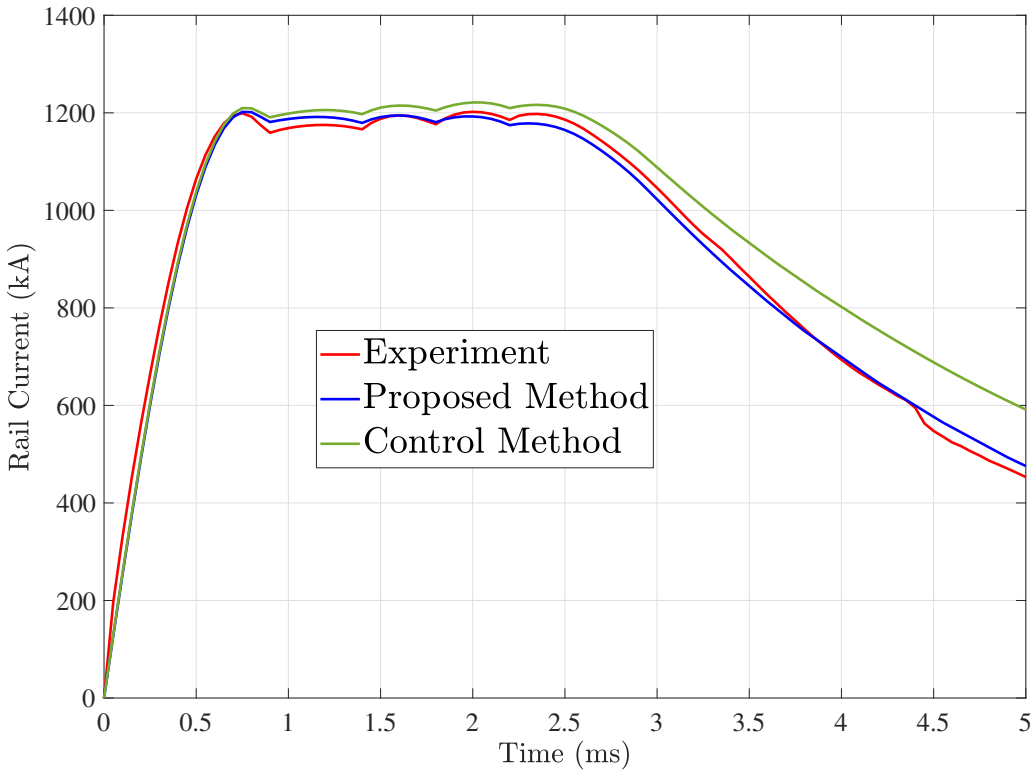

Figure 4.13: Simulated and experimental rail currents of the experiment-D with EMFY-2 launcher.

with the proposed method. In order to understand why improvements have happened, we need to look at the differences between the proposed and the control method. Two simulation methods separate each other at the downslope rail current region. The EMF in the EMFY-1 launcher, which arises from the shift in rail inductance due to lateral displacement of rail current, is not significant compared to EMFY-2. The reason is that EMFY-1 has a smaller rail width. In the control method, the down-slope rail current is lower. The potential reason for such a phenomenon can be an overestimated resistance parameters. The EML model can be considered as discharging the RL circuit in the region of the down-slope rail current. Hence, an overestimated lumped resistance causes the rail current to decay more quickly. As aforementioned, VSE resistance was obtained from the 2-D approximation larger than the 3-D one.

Interestingly, in EMFY-2 simulations, the down-slope mismatch is not dominantly seen. Two factors can be explain such a difference:

Table 4.2: Error analysis[1] of Rail Current Waveform

Experiment No	Previous Method	Proposed Method
EMFY-1 Experiment A	73.29 kA	18.4 kA
EMFY-1 Experiment B	19.61 kA	4.61 kA
EMFY-2 Experiment C	49.58 kA	18.57 kA
EMFY-2 Experiment D	99.13 kA	22.65 kA

[1] RMSE error which we defined in (16) used in this analysis.

Table 4.3: Some Critical Outputs of the EMFY-1 and EMFY-2 Experiments and Simulations with the control and proposed methods

	Proposed Method	Control Method	Exp. Result	Improvement[1]
EMFY-1 Experiment A				
Peak Rail Current (kA)	453	444	457	2.84%
Muzzle Current (kA)	368	325	354	4.21%
Armature Exit Time (ms)	2.70	2.82	2.75	0.70%
Muzzle Velocity (m/s)	2220	2062	2174	3.04%
Muzzle Kinetic Energy (kJ)	102.02	88.44	98.30	6.25%
Efficiency (%)	13.60	11.79	13.11	6.25%
EMFY-1 Experiment B				
Peak Rail Current (kA)	404	401	409	0.73%
Muzzle Current (kA)	306	282	303	5.94%
Armature Exit Time (ms)	2.99	3.10	2.98	0.32%
Muzzle Velocity (m/s)	1891	1744	1973	7.45%
Muzzle Kinetic Energy (kJ)	74.74	63.26	80.96	14.18%
Efficiency (%)	11.96	10.12	12.90	14.18%
EMFY-2 Experiment C				
Peak Rail Current (kA)	1046	1055	1039	0.87%
Muzzle Current (kA)	239	309	272	1.47%
Armature Exit Time (ms)	5.99	6.14	5.90	2.54%
Muzzle Velocity (m/s)	577	576	627	0.15%
Muzzle Kinetic Energy (kJ)	155.14	154.61	199.31	0.27%
Efficiency (%)	12.65	12.62	16.24	0.27%
EMFY-2 Experiment D				
Peak Rail Current (kA)	1202	1222	1202	1.66%
Muzzle Current (kA)	564	657	595	5.21%
Armature Exit Time (ms)	4.51	4.65	4.40	2.37%
Muzzle Velocity (m/s)	928	920	1020	0.78%
Muzzle Kinetic Energy (kJ)	444.47	436.78	585.02	1.31%
Efficiency (%)	13.71	13.48	18.08	1.31%

[1] Improvement ratio is described at (4.19).

1. $\mathrm{R_{backEMF}}$ is under-estimated

2. the VSE resistance is overestimated.

The EMF, derived from rail current displacement, is the leading term in the EMFY-2 as the rail width is larger. Thus, $\mathrm{R_{backEMF}}$ calculation without it appears in an underestimated lumped resistance. Moreover the VSE resistance is overestimated also in EMFY-2 model as in the EMFY-1 model. Two different factors cancels each other in a way that the effect of $\mathrm{R_{backEMF}}$ is more significant. Therefore, in EMFY-2 control method simulations rail current discharges slower.

4.4 Conclusion

The reports that are achieved during the development of the hybrid simulation model can be listed as:

- The results showed that the boundaries, where L_{ext} and $\mathrm{L_{int}}$are placed, are critical as they have differed in two separate methods. They must be determined at the proposed method's surfaces. The surface, which is illustrated in figure 4.9 can be used to calculate the inductance of the system, which 3-FEM did not include in the simulation model.

- The armature movement created an EMF in the rail. However, this is not the only source. The lateral movement of the rail current also creates an EMF. This contribution is dominant, and it must be taken into account in the EML simulations. The right approach for estimating EMF resistance is given in (4.12).

- The calculation of the VSE resistance performed with a 2-D approximation overestimates the actual VSE resistance by 40%. Due to the large error margin, the 3-D Q-T FEM model is a better choice for VSE resistance modeling.

- A hybrid model such as the union of lumped-circuit and 3-D FEM can be used efficiently for EML simulations. Such a method decreases computational complexity. The error due to approximations is tolerable.

CHAPTER 5

TRIGGERING TIME OPTIMIZATION OF PULSE POWER SUPPLIES

Pulse power systems (PPS) for EML applications are mostly capacitor-based topologies [12]. In order to achieve a few MJ stored electrical energy, many capacitor-based PPS modules should be connected in parallel. As there are many units in the PPS, each unit's triggering time changes the total rail current waveform [39]. An example of such a system is demonstrated with Fig. 5.1.

Thus, the timing sequence of PPS affects the performance of the EML directly. Therefore the set of triggering times should be calculated carefully. Examples of optimized and non-optimized rail currents are illustrated in Fig. 5.2.

The optimization of the PPS unit's timing sequence though different objectives and constraints is a well-studied problem in the literature. There are two main approaches to the problem. These are called as iterative and non-iterative algorithms. The literature is mainly focused on non-iterative algorithms, such as evolutionary algorithms (EAs).

A GA is a meta-heuristic optimization algorithm that is inspired by the theory of natural evolution. The algorithm shows the process of natural selection where the fittest individuals are selected for the next generation. Elitism in the GA implies the best solution obtained for the current generation and have a pass to the next generation. Notably, it means keeping the best individual found intact for the next generation. Since it has a positive impact on the convergence of the algorithm, it is also used in this study. The tournament selection parameter is the number of individuals that

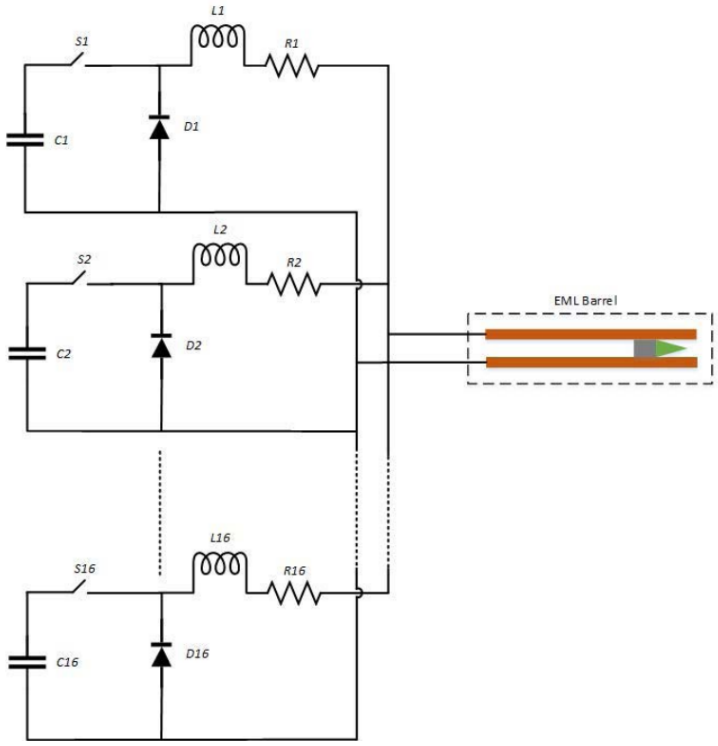

Figure 5.1: The connection of pulse power supplies to EML. In this study 32 capacitive based PPS module connected parallel to EML.

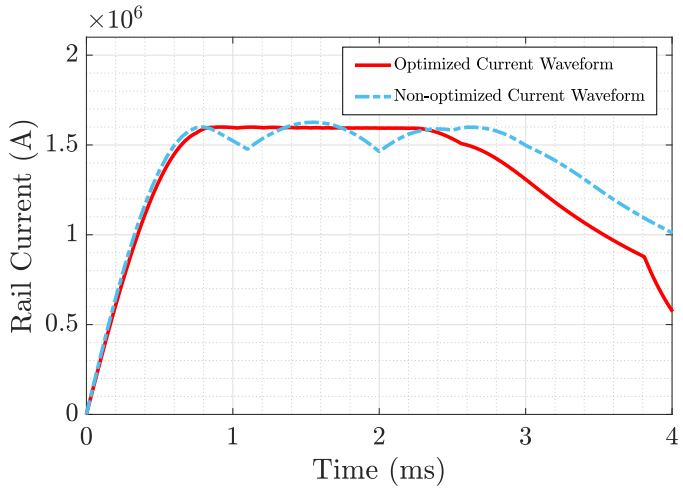

Figure 5.2: Optimized pulse-shaped rail current, and non-optimized one.

sorted as a group. These groups are used crossovers, which ensure the quality of the matches.

PSO is another nature-inspired meta-heuristic optimization algorithm like GAs. The communication between crowds of animals, such as birds and fish, such as finding

a food source and avoiding predators, increases their speed of finding the optimal solution. In this application, "birds" are the triggering times and "the search for a food source" is an analogy for obtaining the v_{max}.

The usage of genetic algorithms (GA) for triggering time optimization problem (TTOP) has the following motivation: the relation between desired rail current waveform and triggering times is nonprogrammable or requires hardware modifications to control the output waveform shape [40]. The triggering time's nonprogrammable nature returns in large numbers of input parameters. Thus, GA has more reliable performance on large dimensional input space so that it is the primary way to use in TTOP[39, 40, 41, 42, 43]. However, the relationship between the rail current waveform and triggering times can be programmable in particular rail current shapes. For example, Zhang *et al.* [44] asserts that for a given magnitude of flat rail current, the set of triggering times that guarantees the desired rail current is unique and can be calculated iteratively. The proposed algorithm is compared with GA-based solutions of TTOP, and the iteration-based method has superior effects on determining timing sequence in terms of costs of computation [45].

In this chapter, an iterative algorithm that calculates the set of triggering times for a given muzzle velocity is proposed. The flat-top rail current waveform is targeted; however, it did not be deemed a strict constraint to the optimization algorithm. An internal control algorithm achieved the rail current's flatness, which reduced the optimization problem's complexity. Apart from other iterative-based solutions of TTOP in literature[44, 45], the proposed model has an additional constraint on down-slope rail current, which is linked with transition risks in the literature. Moreover, the study carried with different capacitor voltages to define the vertex of the TTOP under given constraints. The algorithm is compared with non-iterative algorithms in the literature, GA and Particle Swarm Optimization (PSO). These algorithms are used to create benchmarks to present the computational load deficit when the proposed algorithm is used.

The organization of the chapter is the following: firstly, the literature survey of the TTOP is supplied, and the main objectives and constraints of these problems are defined. Then, the simulation model used in this study is demonstrated. The proposed

Table 5.1: EML Design Parameters and Limitations.

Rail Height	70 mm
Rail Separation	70 mm
Rail Width	50 mm
Rail Length	5 m
Pre-load Distance	70 cm
Projectile Mass	500 g
Maximum Linear Current Density	32.5 kA/mm
Maximum Peak Current	2275 kA

model is described and compared with the GA and PSO models, and the conclusions are presented. Although the proposed method is found to be applicable for different launcher systems, for clarity the launcher design and limitations are used which are listed in Table 5.1.

5.1 Triggering time determination

Triggering strategy is one of the decisive features that affect the launcher efficiency and the systems' generated forces. Thus, TTOP is a well-studied topic in EML literature. These studies can be divided into two sections in terms of their objectives. These are listed in the following subsections.

5.1.1 Optimizing the Triggering Times to Obtain the Maximum Muzzle Velocity

Although the L', one of the important parameter which determines the EML efficiency, is not dependent on the triggering strategy, other parameters such as linear current density $\vec{J}_{linear}$, the muzzle current $\vec{I}_{exit}$ influence the launch. An example of such TTOP is given in (5.1). Constraints are illustrated with a rail current example in Fig. 5.3.

The objective of the problem is maximizing the muzzle/exit velocity denoted as v_{exit}. Constraints are adjusted considering the transition phenomena, which are linked heavily to the launch security. The transition phenomenon is described as the transition of

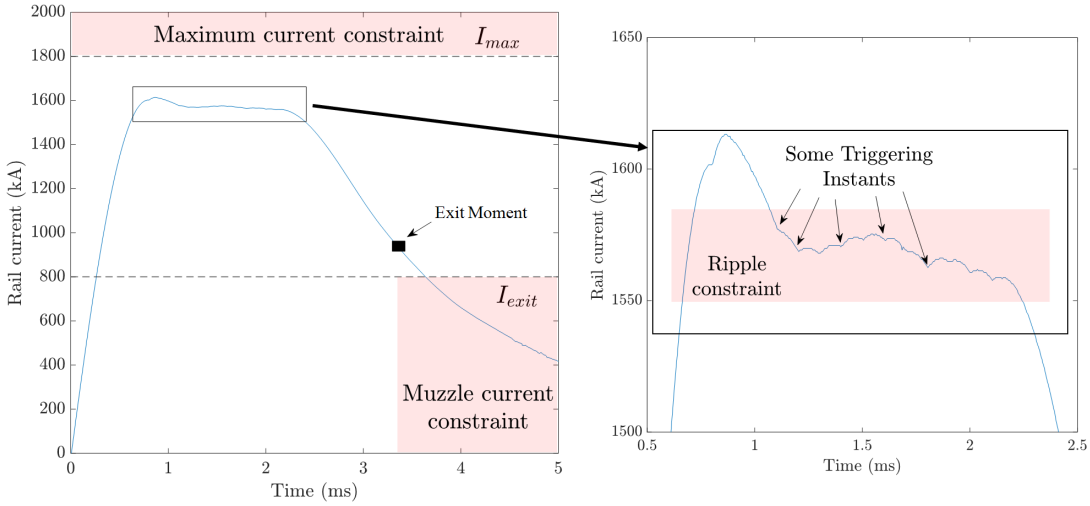

Figure 5.3: Constraints in 5.1 are illustrated with an rail current example.

solid contact into arcing contact. There are multiple mechanisms that cause transition [46]. One of them is the $\vec{J}_{linear}$. I_{max} refers to the maximum allowed rail current, which is related to rail dimension and the $\vec{J}_{linear}$. Therefore, for a pre-defined EML geometry and selected $\vec{J}_{linear}$, I_{max} can be introduced as a constraint to the magnitude of the pulse shape current denoted as I_{ref}. The muzzle/exit current denoted as I_{exit} is considered as another transition constraint. I_{exit} is responsible for the so-called "down-slope transition," which is reported by different studies in the literature. Wang *et al.* [47] reported that the down-slope transition occurs when the I_{exit} is lower than 90% of the I_{ref}. Satapaty *et al.* [48] made a statistical analysis based on the experiments and showed that the down-slope transition occurs when I_{exit} is lower than 80% of the I_{ref}. It should be noted that these studies were conducted with small and medium caliber EMLs, respectively. In EMFY-3 experiments, transitions are observed either I_{exit} is above 80% of I_{ref} or I_{exit} is below 80% of I_{ref}. Increasing I_{exit} percentage decreases the efficiency of the launch, as the muzzle current is useless in terms of electro-mechanical energy conversion. Thus, in this study, I_{exit} is

constrainted 50%. This value can be adjusted as a hyper-parameter for TTOP.

$$\begin{aligned} \text{max} \quad & \mathrm{v_{exit}} \\ \text{subject to} \quad & \mathrm{I_{ref}} \leq \mathrm{I_{max}} \\ & \mathrm{I_{exit}} \geq 0.5\mathrm{I_{ref}} \\ & |\mathrm{I_{rail}} - \mathrm{I_{ref}}|_{\mathrm{RMS}} \leq \epsilon \mathrm{I_{ref}} \quad t \in [t_1, t_2] \end{aligned} \tag{5.1}$$

The third constraint is the deviation of the pulse current wave-shape. RMSE is used as an error measure, which is defined in (5.2). n represents the number of current samples. ϵ in the third constraint in the (5.1) is the allowed deviation in the I_{rail}. It should be in the form of a flat-top pulse shape. Sharp variations in the rail currents are undesirable due to voltage oscillations in the EML, which is considered as inductive load.

$$\mathrm{RMSE} = \sqrt{\frac{1}{\mathrm{n}} \sum_{\mathrm{i}=1}^{\mathrm{n}} \left(\mathrm{I_{ref}} - \mathrm{I_{rail}}\right)^2} \tag{5.2}$$

Zhengjun *et al.* [42] made a TTOP study that maximize v_{exit} and efficiency. Since two objectives are targeted, the Pareto frontier is used. The acceleration of the armature is constrained due to the payload security. The deviation of the pulse current shape, as well as I_{exit} is not considered. Yu *et al.* made another TTOP study that has the same objective as [42]. I_{ref} is constrained, considering the maximum allowed acceleration. The novelty of the simulation model, the addition of VSE and contact resistances, are introduced. However, I_{exit} and the quality of the pulse current waveform is not recognized. Moreover, both studies used an evolutionary algorithm (EA) that is computationally expensive, and not practical.

5.1.2 Optimizing the Triggering Times to Ensure Desired Muzzle Velocity

Efficiency can be sacrificed when the tactical operation is deemed in EMLs. Therefore, TTOP should have different objectives rather than maximizing v_{exit}. An example of such TTOP is represented in (5.3). The objective of the TTOP is the diminishing the quadratic velocity error. l_1 norm/absolute error is not considered as a

minimizer considering its non-differentiable nature. (5.3) shares the same constraints with (5.1).

$$\begin{aligned} \text{min} \quad & (\mathrm{v_{desired}} - \mathrm{v_{exit}})^2 \\ \text{subject to} \quad & \mathrm{I_{ref}} \leq \mathrm{I_{max}} \\ & \mathrm{I_{exit}} \geq 0.5\mathrm{I_{ref}} \\ & |\mathrm{I_{rail}} - \mathrm{I_{ref}}|_{\mathrm{RMS}} \leq \epsilon \mathrm{I_{ref}} \quad t \in [t_1, t_2] \end{aligned} \tag{5.3}$$

Chao *et al.* [49] used a harmony search algorithm for TTOP. Desired muzzle velocity $v_{desired}$ is targeted. I_{max} is used as an constraint. However, I_{exit} is not considered. Zhang *et al.* [44] used an iterative algorithm rather than evolutionary algorithms for the TTOP. $v_{desired}$ is targeted. The shape of the pulse rail current is constrainted. However, the efficiency is not considered. Liu *et. al* maximized the efficiency with $v_{defined}$ under the I_{max} constraint. However, I_{rail} does not consider the pulse waveform as well as the I_{exit} constraint. The literature survey is summarized in Table 5.2.

Table 5.2: Literature Survey on Triggering Time Algorithms.

	Objective	**Method**	**Constaints**
[50]	Muzzle velocity	Iterative	-
[51]	Muzzle velocity	GA	Current
[52]	Max velocity, max efficiency	GA, NSGA-II	Accelaration
[53]	Max velocity, max efficiency	GA, NSGA-II	Current
[54]	Desired current waveform	GA	
[49]	Muzzle velocity	Harmony Search, ODM	Current

5.2 The Simulation Model

The detailed analysis of EMLs requires 3-D FEM simulations. However, optimizations with 3-D FEM are time-consuming; thus, appropriate simplifications should be made to have reasonable computation time [16]. In this section, these simplifications and the construction of the 1-D EML model is explained. The EML can be modeled with a dynamic R-L circuit. The R-L circuit is illustrated in Fig. 5.4. $\mathrm{R_{EML}}$ and $\mathrm{L_{EML}}$ represent the total resistance and inductance of the EML, respectively. It should be noted that $\mathrm{R_{EML}}$ is dependent not only position but also frequency (f) and

the armature velocity (v).

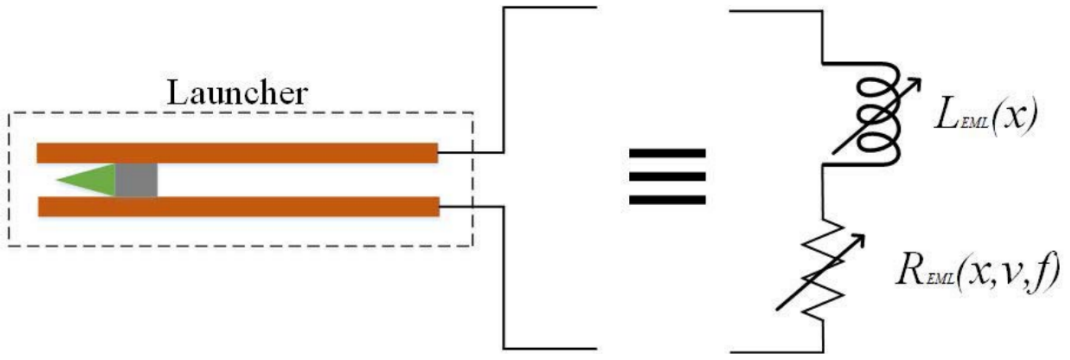

Figure 5.4: The R-L approximation of the EML system. $\mathrm{L_{EML}}$ and $\mathrm{R_{EML}}$ defined as equivalent inductance and resistance of electromagnetic launcher [37].

In EMLs, there are mainly three major elements affecting the $\mathrm{R_{EML}}$ like in (5.4). The AC resistance, $\mathrm{R_{ac}}$ occurs when there is a change in the rail excitation current due to skin and proximity effects. The second element is the VSE resistance ($\mathrm{R_{vse}}$), which happens at the trailing edge of the armature-rail contact interface and is highly dominant at high projectile velocities. The last element is the EMF at the breach denoted as $\mathcal{E}$, which can be modeled as a resistor. ($\mathrm{R_{emf}}$). Although EMF is not a resistive component from a physical perspective, it can be modeled with a resistor from a mathematical perspective as in (5.5), (5.6) as mentioned before in Chapter 3 and 4.

$$\mathrm{R_{EML}} = \mathrm{R_{vse}(v)} + \mathrm{R_{ac}(f)} + \mathrm{R_{emf}(v)} \tag{5.4}$$

$$\mathcal{E} = \frac{\mathrm{dL(t)}}{\mathrm{dt}}\mathrm{I(t)} + \mathrm{L(t)}\frac{\mathrm{dI(t)}}{\mathrm{dt}} \tag{5.5}$$

$$\mathcal{E} = \mathrm{R_{emf}I(t)} + \mathrm{L(t)}\frac{\mathrm{dI(t)}}{\mathrm{dt}} \tag{5.6}$$

As stated in [55] and [56] the $\mathrm{L_{EML}}$ has two components. $\mathrm{L_{ext}}$ is the inductance between the rails and $\mathrm{L_{int}}$ is the inductance component inside the rails. In (5.7) calculation of the total inductance gradient ($\mathrm{L'_{EML}}$) was presented. B equals to $\mathrm{B_z}$ due to

symmetry. Multiplied with the number of turns (single turn in our case), the surface integral of $\mathrm{B_z}$ results in flux linkage λ. When λ is divided by the rail current results in the instantaneous inductance of the rails is obtained. In order to find the total transient inductance gradient, flux linkage λ was divided to I_{rail}, and the distance between the breech and the $\mathrm{B} = 0$ contour line inside of the armature which is denoted by $\mathrm{x_0}$. The $\mathrm{L_{EML}}$ calculation was given in (5.8). The integration area and $\mathrm{x_0}$ can be seen in Fig. 5.5.

$$\mathrm{L'_{EML}} = \mathrm{L'_{ext}} + \mathrm{L'_{int}} = \frac{\frac{1}{2\mathrm{I_{rail}}} \int |\mathrm{B_z}| \mathrm{dA}}{\mathrm{x_0}} \tag{5.7}$$

$$\mathrm{L_{EML}(x)} = (\mathrm{L'_{ext}} + \mathrm{L'_{int}})\mathrm{x} \tag{5.8}$$

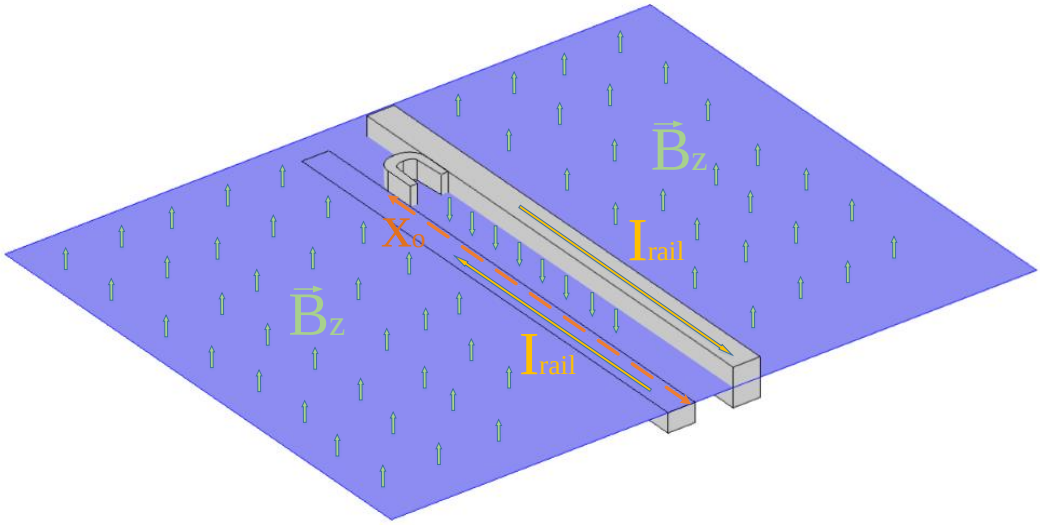

Figure 5.5: Integration boundary and $\mathrm{x_o}$.

$\mathrm{R'_{ac}}$, $\mathrm{L'_{ext}}$ and $\mathrm{L'_{int}}$ is found by calculating gradients while keeping the armature stationary in 3-D FEM. These gradients are used to create position-dependent lumped parameters updated with the armature motion in the 1-D model. The total resistance of the rail is calculated using the ohmic loss calculation as in (5.9). Hence an empiric formulation was developed and used during the simulation. In (9-11), the resistivity of the rails is denoted as ρ_{rail}. $\mathrm{J_{rail}}$ and $\|.\|$ represents the current density inside the

rails and l_2 norm, respectively.

$$\mathrm{R_{ac}(x)} = \mathrm{x}\frac{1}{\mathrm{I(t)}^2}\iiint_{\mathrm{V}} \rho_{\mathrm{rail}} \left\| \mathrm{J_{rail(t)}} \right\|^2 \mathrm{dV} \tag{5.9}$$

Due to the lack of a 3D body in the 1-D simulation environment, transients of $\mathrm{L}^{'}$ and $\mathrm{R_{ac}}$ are not achievable. In [55], $\mathrm{R_{ac}}$ is relatively high during the early stages of the launch compared to $\mathrm{R_{vse}}$ and $\mathrm{R_{emf}}$, $\mathrm{R_{vse}}$ and $\mathrm{R_{emf}}$ are the dominating resistances after 500 m/s. Moreover, in our study, the flat-top current further reduces the skin effect; hence $\mathrm{R_{ac}}$ was neglected during the analysis. In this study, special attention to $\mathrm{L'_{EML}}$ calculation is given due to precise transient modeling. A 3D FEM model is performed to investigate the following theorem, which is similar to the study in [55] and [56].

Theorem 5.2.1 *Total inductance gradient ($\mathrm{L'_{ext}} + \mathrm{L'_{int}}$) is invariant from I_{ref} when pulse rail current is applied. The rise time of the rail current is kept constant, considering the rail currents form from identical PPS units.*

The variation of $\mathrm{L'_{EML}}$ with different rail current pulses needs to be analyzed. In Fig. 5.6 the rail geometry and in Fig. 5.7 the excitation currents are presented. According to Fig. 5.7, the total inductance gradient does not change for different pulse current excitations. In this figure, non-optimized I_{rail} is shown for better understanding of the third constraint of (5.1) and (5.3).

It is possible to consider the rails as a single turn concentrated coil where the effective distance between the rails changes due to the dependence of skin effect on the change in the rail excitation current. In Fig. 5.6 the distance between the rails geometry is d_1, the distances between the concentrated current and inner edge of the rails are d_2 and therefore the effective distance between the rails is $\mathrm{d_{coils}} = \mathrm{d}_1 + 2\mathrm{d}_2$.

If there is a change in the magnitude of current (i.e $\frac{\mathrm{dI}}{\mathrm{dt}}$), $\mathrm{d_{coils}}$ gets closer to d_1 since the skin effect current concentrates on the inner surface of the rails (as in current rise at the first few ms.). However, as the current reaches to flat top of the waveform, the current distribution gets more homogeneous, and hence more flux-linkage (λ) is

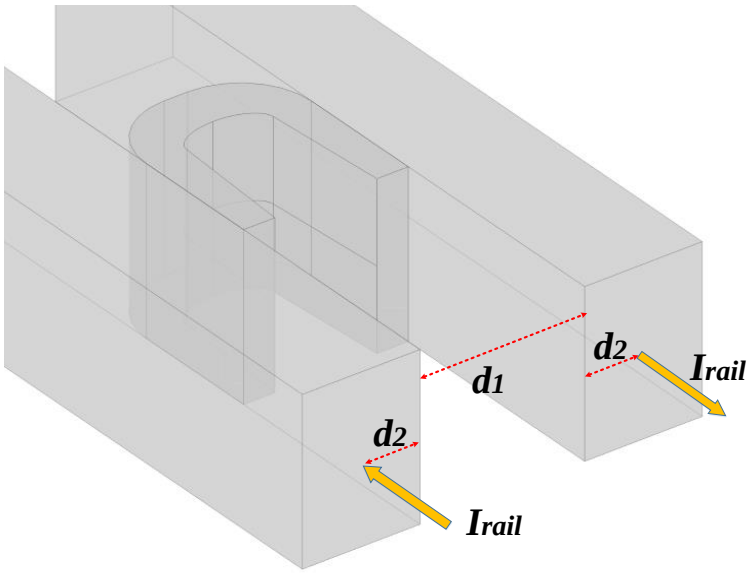

Figure 5.6: Concentrated coil approach, breech to muzzle cross-section.

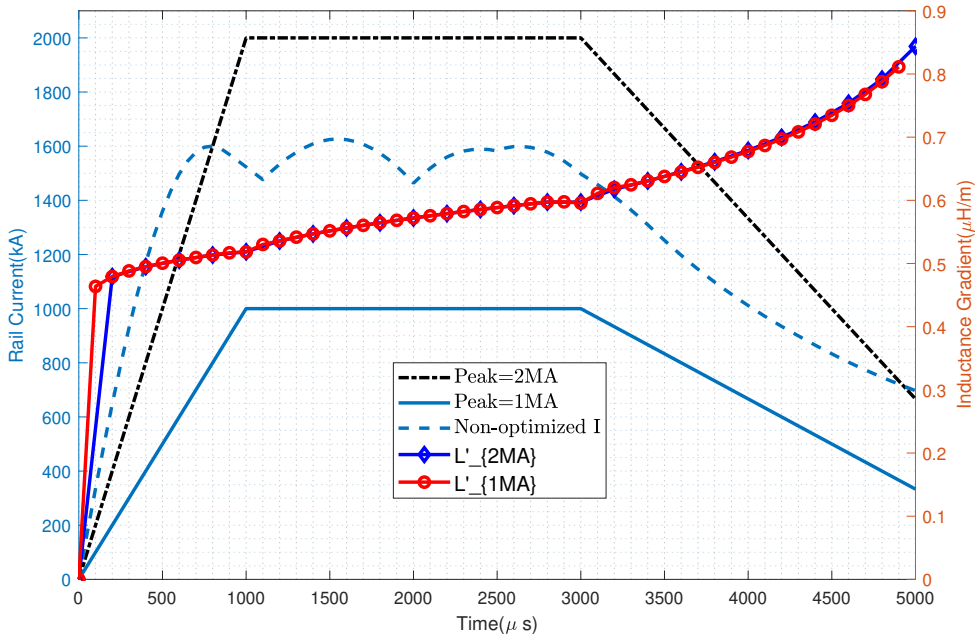

Figure 5.7: Current excitation on the rails, resultant transient inductance gradients and non-optimized current waveform.

obtained. Moreover, since the change in total $L^{'}$ is independent of current pulse shape, the same $L^{'}$ can be used during 1-D modeling. Thus, there is no need for 3-D FEM simulation for accuracy of L', when the triggering times are optimized.

5.3 Multi-level Fast Triggering Time Algorithm (MFTTA)

Multiple capacitive PPS modules are used to achieve higher energized projectile in EML applications. Parallelling is applied to complete this task. 16 PPS modules are used. For larger-caliber as well as higher energy EMLs, the number of capacitive PPS unit is also increased. In this study, 32 capacitive PPS modules are used for that purpose. Since there are multiple electrical excitation modules, there is N triggering time, which should be optimized. The design variables are shown by following vector notation where i represent PPS module index and α represents the number of initial firing as in (5.10), and (5.11).

$$\vec{t} = \begin{pmatrix} t_\alpha \\ \vdots \\ \vdots \\ \vdots \\ \vdots \\ t_{32} \end{pmatrix} \quad 0 \leq t_i \leq 4\text{ms} \;\; \forall i \in [\alpha, 32] \tag{5.10}$$

$$\mathrm{t_i} = 0 \quad \forall i \in [1, \alpha] \tag{5.11}$$

MFTTA consists of two main parts. The first part is a hysteresis control of I_{rail} with the I_{ref}, which is the magnitude of the trapezoidal current waveform. Then, the algorithm determines how many modules to be fired at the beginning. The pulse current shape is conserved with a hysteresis control in the simulation model. The hysteresis control is made with COMSOL's Event interface, where the simulation can be stopped with predefined variable conditions. Therefore, when I_{rail} is below I_{ref}, the event interface is triggered and saves the time where this event happened. This time can be used as a new triggering time, since the new triggering can hold the I_{rail} at the I_{ref} level, thanks to the additional energy comes from the new PPS module. The second part of the MFTTA is responsible for the find the I_{ref} that ensures the $v_{desired}$. Each part is explained in the following subsections. The pseudo-code of the algorithm is presented in Fig. 5.8.

Algorithm 1 The Multi-Level Fast Triggering Time Algorithm.

Input: $v_{desired}$
Output: $[t_1 ... t_N]$

Calculating Initial Firing:
Discretize I_{ref} with N_{min} and N_{max}
Obtain pulse rail current which have magnitude I_{ref} using hysteresis control in the simulation
Discretize v using previous step rail currents
Find the I_{ref} interval (N_i and N_{i+1}) for $v_{desired}$
Line Search at the interval
Compute two intermediate points using golden ratio

while $r_e < \epsilon$ **do**
  if $(I_1 < I_2)$ **then**
    Change the lower bound; $I_L = I_2$
    Carry the intermediate point to the next; $I_2 = I_1$
    Calculate the new intermediate point, I_1'
  end if
  if $(I_2 < I_1)$ **then**
    Change the higher bound; $I_H = I_1$
    Carry the intermediate point to the next; $I_1 = I_2$
    Calculate the new intermediate point, I_2'
  end if
  compute relative error, r_e
  compute the new distance $(I_H - I_L)$
end while
return $\vec{I}_{opt}$

Figure 5.8: Pseudo-code of the algorithm.

5.3.1 Pulse Current Shape with Hysteresis Control (PCSHC)

The flowchart of the pulse current shape with hysteresis control (PCSHC) is illustrated in Fig. 5.9. The first part is a hysteresis control of rail current with the given reference current I_{ref} which is the peak of the trapezoidal current waveform. Intermediate results of the hysteresis control is illustrated in Fig. 5.10. Then, the algorithm determines how many modules to be fired at the beginning.

The rail current waveforms with various initial firing sequences are given in Fig. 5.11. The maximum current limit is determined by the maximum linear current density constraint and rail dimensions. After selecting the number of initial firing modules, the algorithm tries to find the next triggering points which create pulse shaped rail current at I_{ref}. COMSOL's Event interface is used to build an hysteresis control. Simulation

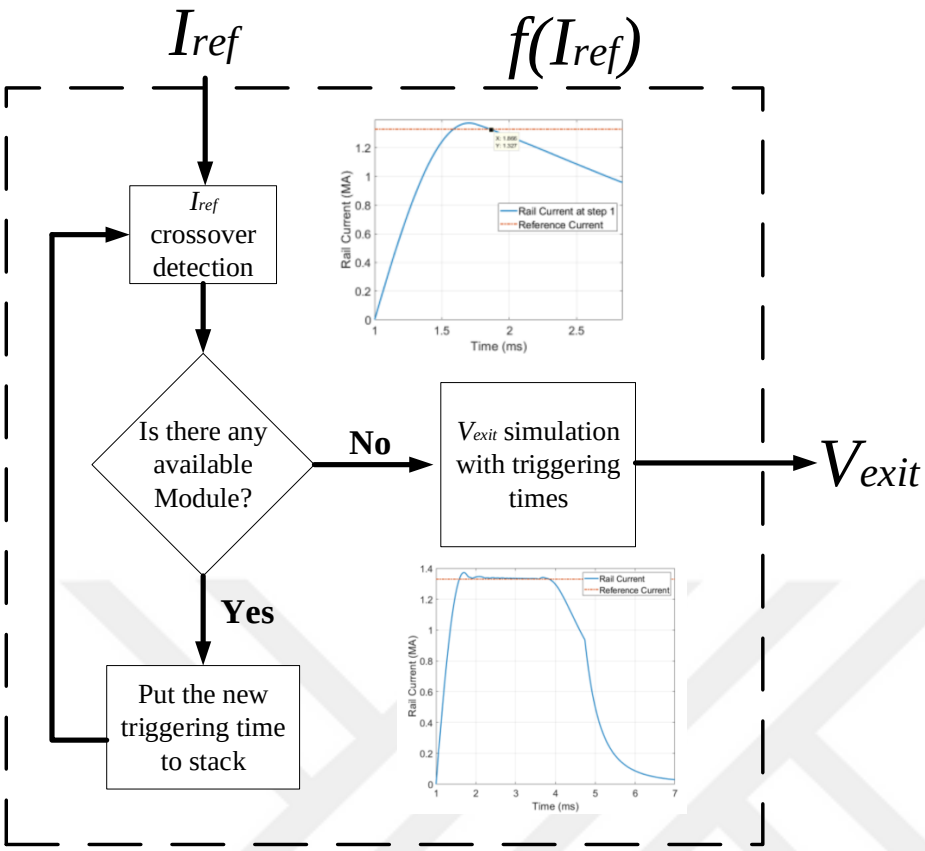

Figure 5.9: PCSHC. The algorithm takes input as I_{ref} and give N amount triggering time which associated with a unique ν_{exit}. The algorithm spend $N - M$ circuit simulation time for all obtaining triggering times.

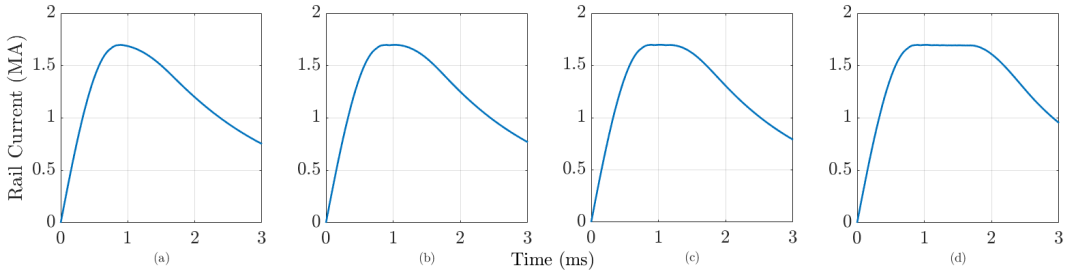

Figure 5.10: Intermediate results of the pulse current algorithm. The algorithm search for trigger time which is defined as moment that rail current decreased from I_{ref}. Then, it restart the simulation with a new triggering time, and search for next. While iterations continue, the rail current becomes pulse shape current with increasing width.

is aborted just after the new trigger point is generated to reduce the computation time. The results of the first part of the algorithm with respect to various I_{ref} values are given in Fig. 5.13. If the PPS unit has N parallel modules and one simulation takes T time, after selecting the initially fired modules (denoted as M), firing instants of $N-M$ units need to be determined. This means that the simulation has to be repeated $N-M$ times for pulse current waveform which has a magnitude of I_{ref}. Since there is a stop condition in simulations, simulations are aborted immediately after finding the triggering instant, controller finds triggering sequence at $(N-M)t/2$ time, neglecting the convergence time of the simulation. Simulations take a few seconds since the study conducted in 1-D.

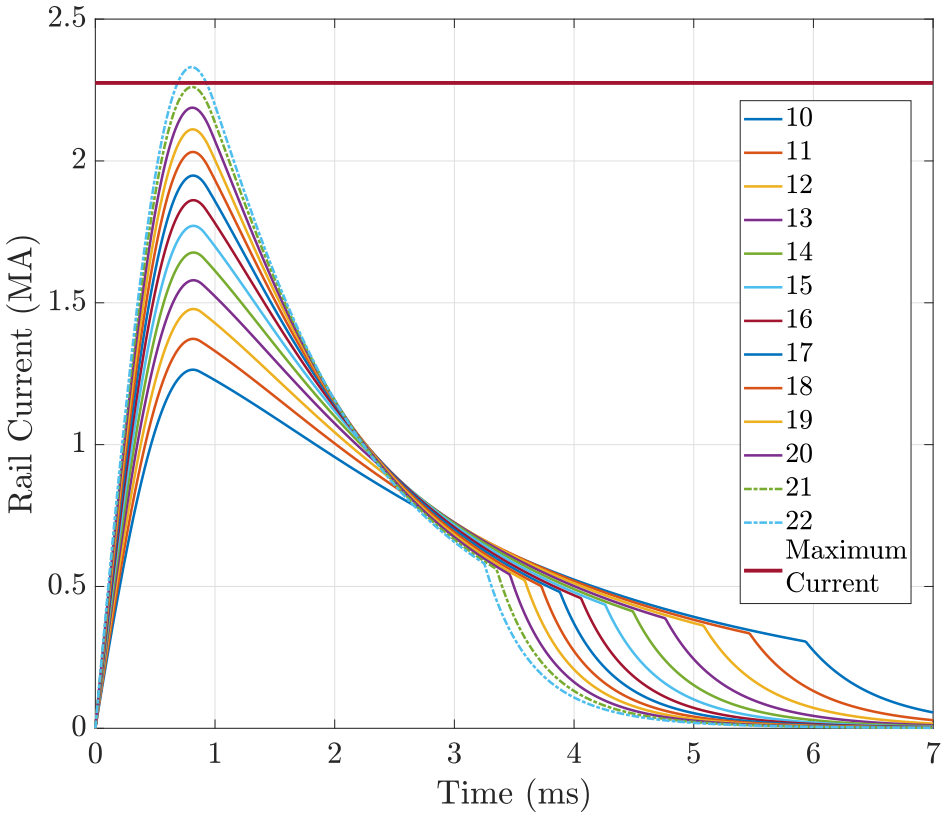

Figure 5.11: Peak current vs. number of modules triggered at t=0 ms. The dashed current lines exceeds the maximum current density in Table 5.1.

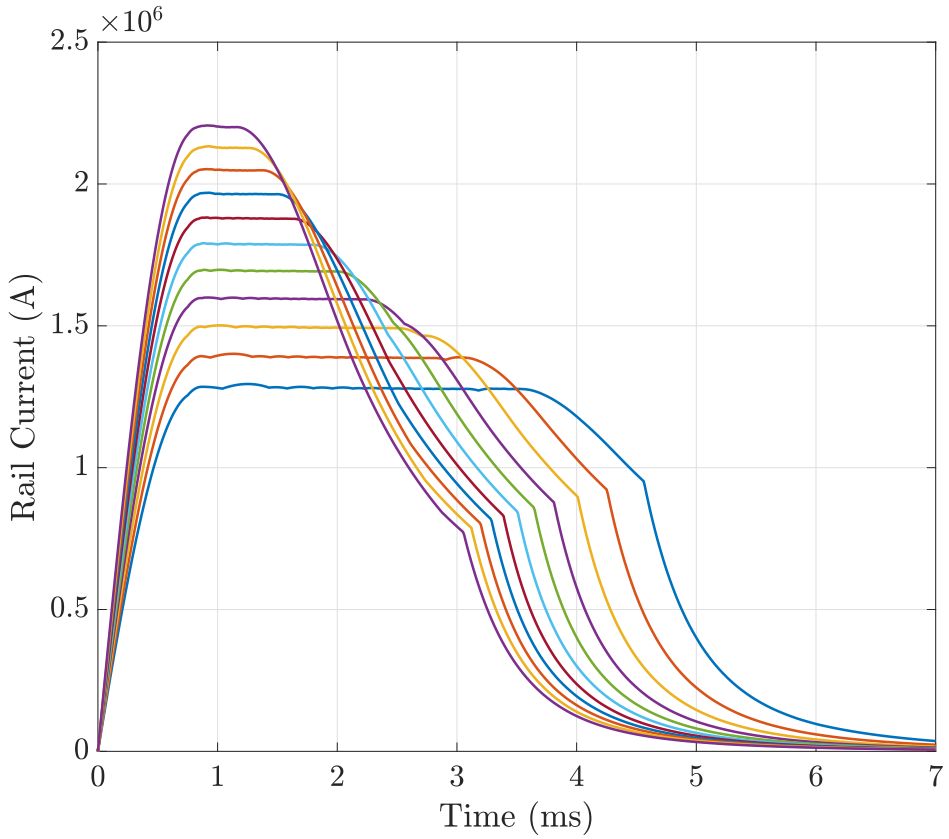

Figure 5.12: The results pulse current algorithm respect to different I_{ref}. N denoted as module number is taken 32. The capacitor voltage of the module are identical at 6500 V.

5.3.2 Determination of the Required I_{ref} for Desired Exit Velocity

The first part of the algorithm generates triggering sequence with given current limit I_{ref}. However, at this stage, the I_{ref} for a unique projectile muzzle velocity is still unknown. For this purpose following theorem is proposed by [44].

Theorem 5.3.1 *There exist a unique I_{ref} for a given exit velocity. Therefore, there exits a unique set of triggering times for every exit velocity value.*

Such a statement is true with the assumption of constant capacitor voltage and constant launch package mass. The effect of these parameters will also be discussed in the next sections. Exit velocity vs. amplitude of pulse current, I_{ref}, is given in Fig. 5.14. It is clear that exit velocity is a one-to-one function of I_{ref}. Moreover, the er-

ror function, which is defined as $I_{ref} - I_{ref}^2$, is a uni-modal function with the given boundaries. Therefore, a line search algorithm can be used for finding proper I_{ref} value. In this study, we used golden section search algorithm for line search method [57]. Some steps of the golden search algorithm is illustrated in Fig. 5.15. The performance of the golden section algorithm is given in Fig. 5.16.

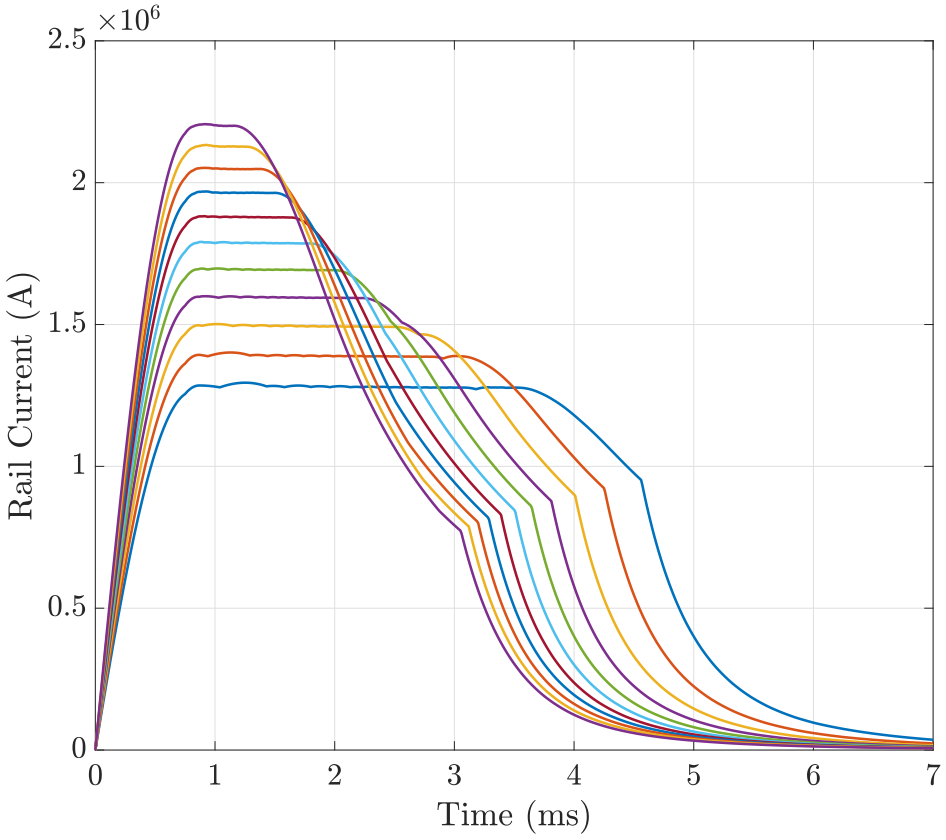

Figure 5.13: The results pulse current algorithm respect to different I_{ref}. N denoted as module number is taken 32. The capacitor voltage of the module are identical at 6500 V.

After a few iterations, the relative error in the exit velocity is reduced down to 0.1%. Considering that one function evaluation, which finds a set of triggering time for a given I_{ref}, takes 10 to 18 circuit simulations (depending on the number of design variable), the proposed algorithm requires a few tens of simulations for 1% relative error and one or two hundred simulations for 0.1% relative error. However, it should be noted that the performance parameter of the algorithm is relative error. Thus, the accuracy of the speed control is still heavily depends on the 1-D simulation accuracy.

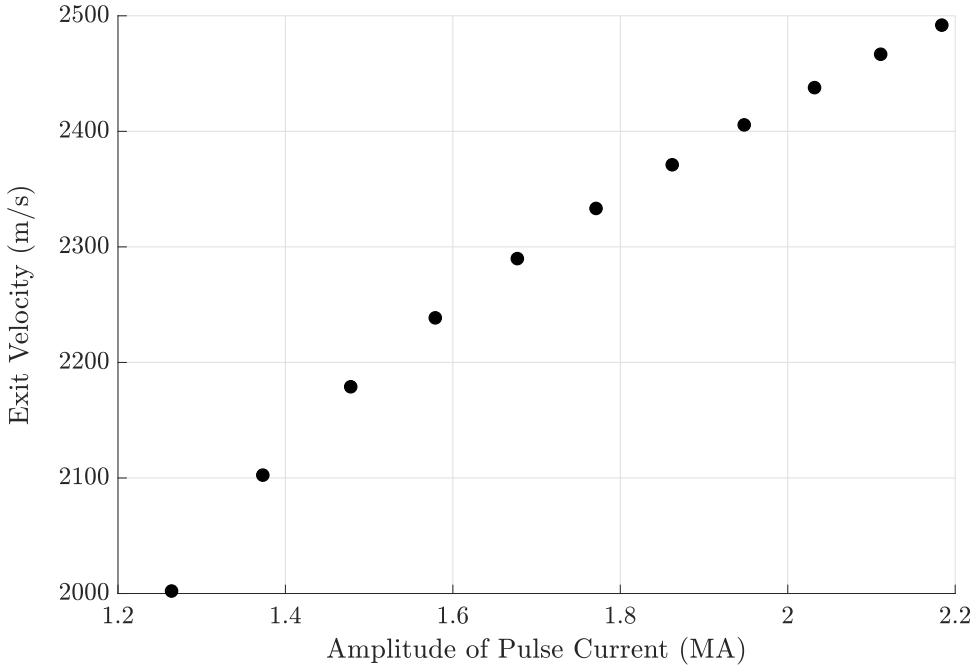

Figure 5.14: Exit velocity vs amplitude of pulse current graph at $V_c = 6500\ V$. This graph indicates that there exist a unique pulse shape current for all exit velocities.

The scope of the study includes a triggering strategy algorithm and exclude the pure performance of the 1-D model. However, enhancements can be made with 1-D model and the proposed triggering algorithm can be applied directly.

5.4 Results

Two EAs are implemented to solve TTOP. These algorithms create not only benchmarks to the MFTTA but also some understandings about the effects of the constraints. The parameters we used in RCGA given as in Table 5.3. The parameters of PSO are given Table 5.4. The hyper-parameter optimization for these algorithms is skipped considering the scope of this study.

Two different optimization studies are conducted with RCGA. These studies differ from their constraints. The I_{max} constraint is relaxed in one of the studies to show the effect. The convergence graphs are shown in Figs. 5.17 and 5.18. The objective of

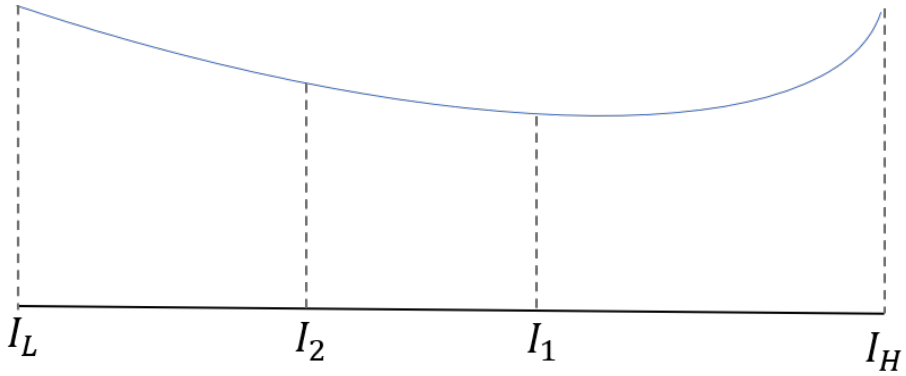

(a) Initialization with the intermediate points.

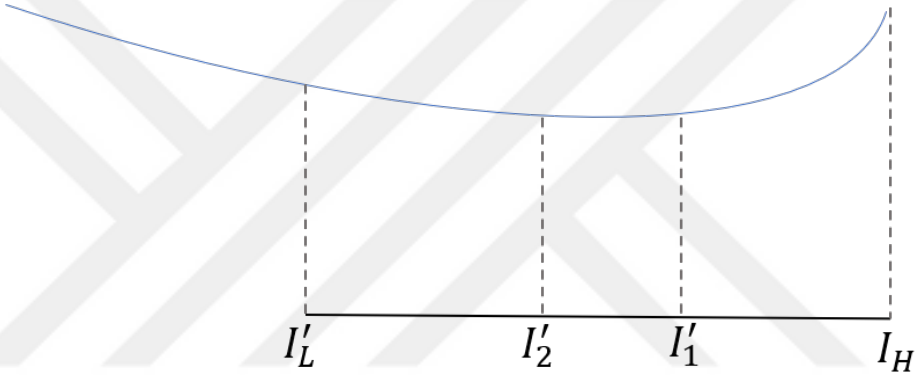

(b) Narrowing the search distance when ($I_1 < I_2$).

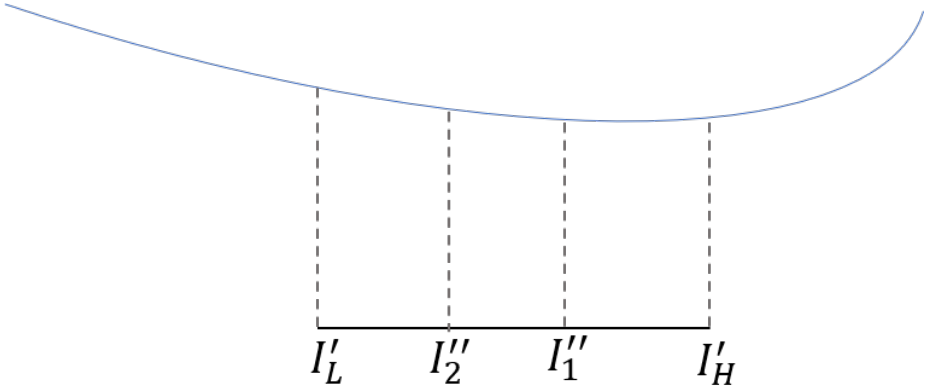

(c) Narrowing the search distance when ($I_2 < I_1$)

Figure 5.15: Same steps of the golden search algorithm.

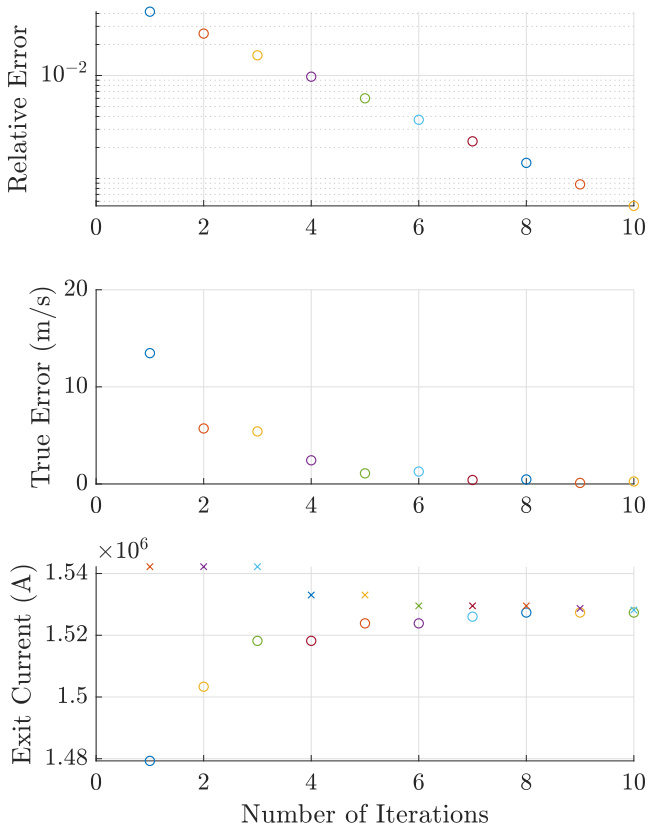

Figure 5.16: The performance of golden section line search algorithm. Noted that the golden section line search algorithm uses only one function evaluation at all iterations except the initial one. Considering that one function evaluation takes 10 to 18 circuit simulations, the proposed algorithm requires a few tens of iterations for 1% relative error and one or two hundred iterations for 0.1% relative error.

Table 5.3: The parameters of RCGA

Population Size	50
Number of Generation	100
The number of design parameters	16
Elite Size	5
Tournament Selection	10
Croosover Rate	0.8
Mutation Rate	0.2

these studies is maximizing v_{max}. The best individuals of the selected iterations are illustrated in Figs. 5.19 and 5.20. I_{rail} and the velocity curves are used for visualiza-

Table 5.4: The parameters of PSO

Population Size	50
Number of Generation	100
The number of design parameters	16
Maximum velocity	0.1 ms
Minimum velocity	-0.1 ms
Inertia	1
Damping Inertial Term	0.99
Social Acceleration Term	1.4962
Personal Acceleration Term	1.4962

tion of the effect triggering times. When the I_{max} constraint is relaxed, the triggering time converges to all zero vector, as in Fig. 5.19. However, when violation of I_{max} is penalized the I_{rail} is nothing but the pulse current that have I_{max} length. This can be understood from Fig. 5.17.

The result of the PSO is demonstrated in Fig. 5.21. Each circle represents an individual/particle, and each color represent a generation. The movement of the particle is shown using an arrow. I_{max} constraint is applied. Therefore, the comparison between RCGA and PSO in terms of convergence should be made between Figs. 5.17 and 5.21. Although both algorithms converge to the same optimum solution, RCGA reaches the optimum solution at the 46th iteration whereas PSO reaches at the 11th. Thus, PSO outperformed RCGA in a TTOP. The comparison of the three algorithms in terms of computational load is represented in Table 5.5.

Table 5.5: The Performance Comparison of the Methods

	GA	**PSO**	**MFTTA**
Objective: $v_{desired}$	2500	950	160
Objective: v_{max}	2300	550	18[2]

[1] Each number represent the number of simulations/function evaluations for the given method.

[2] MFTTA use the information that for maximizing v_{max}, the I_{rail} should be pulse shaped current with the magnitude I_{max}.

The results showed that MFTTA outperformed GA and PSO in terms of computational load. The reason is that MFTTA has the ability to transform multiple input fea-

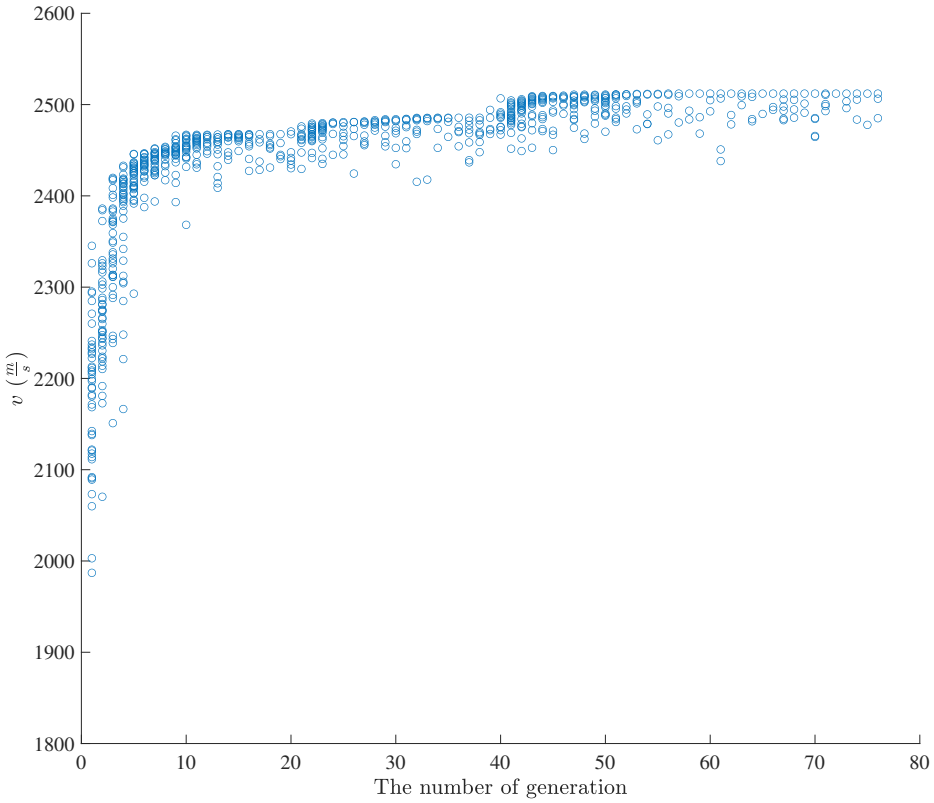

Figure 5.17: Individuals of each generation and their cost values with RCGA with constraints. The population size looks like decrease after generations due to maximum current constraint.

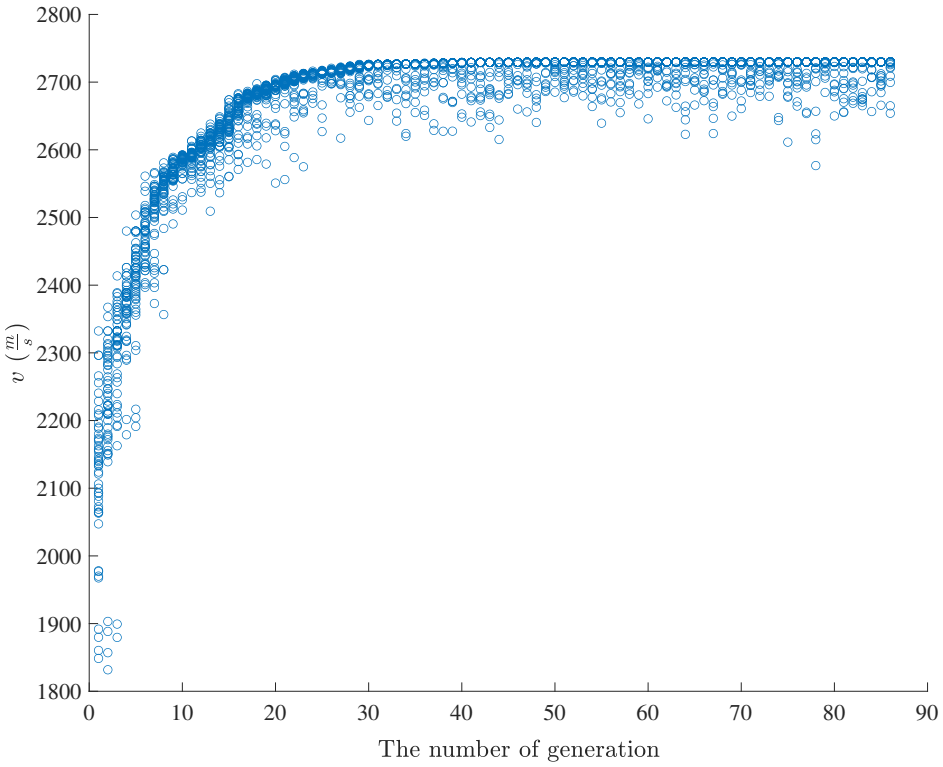

Figure 5.18: Individuals of each generation and their cost values with RCGA. No constraint applied. The purpose of this study is understanding of behaviour of system with respect to triggering times. After various iterations the maximum v_{exit} is 2723 m/s which corresponding to all triggering times are 0 s. However this result violate the maximum rail current constraint.

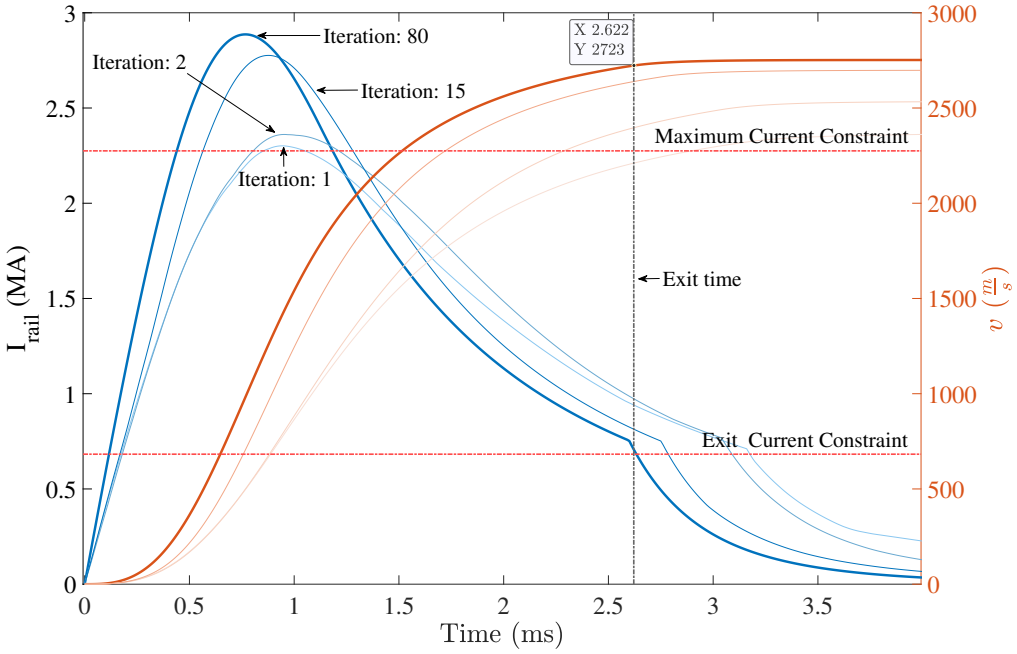

Figure 5.19: Initial intermediate and final steps of RCGA without constraint. It showed that the firing sequence converged to zero vector (indicating that all PPS modules triggered initial time step). However, this condition violate the maximum rail current constraint

tures (triggering times) to one input feature, I_{ref}. Since the search space dimension is reduced to one, and the error function is uni-modal, a simple line search algorithm can minimize the error with a few iterations. In Fig. 5.22, different MFTTA results are illustrated to understand the behavior of various triggering strategies better. For a specified v_{exit}, there are multiple I_{rail} guarantees the v_{exit} and each of them has different PPS voltage denoted as V_c. This situation is illustrated in Fig. 5.23. Six different I_{ref} and their set of triggering times that guarantee 2153 m/s muzzle speed are obtained. The most efficient one is the one that has the lowest V_c. Consequently, this solution also has the lowest I_{exit}. Therefore, there is a trade-off between efficiency and the risk of transition.

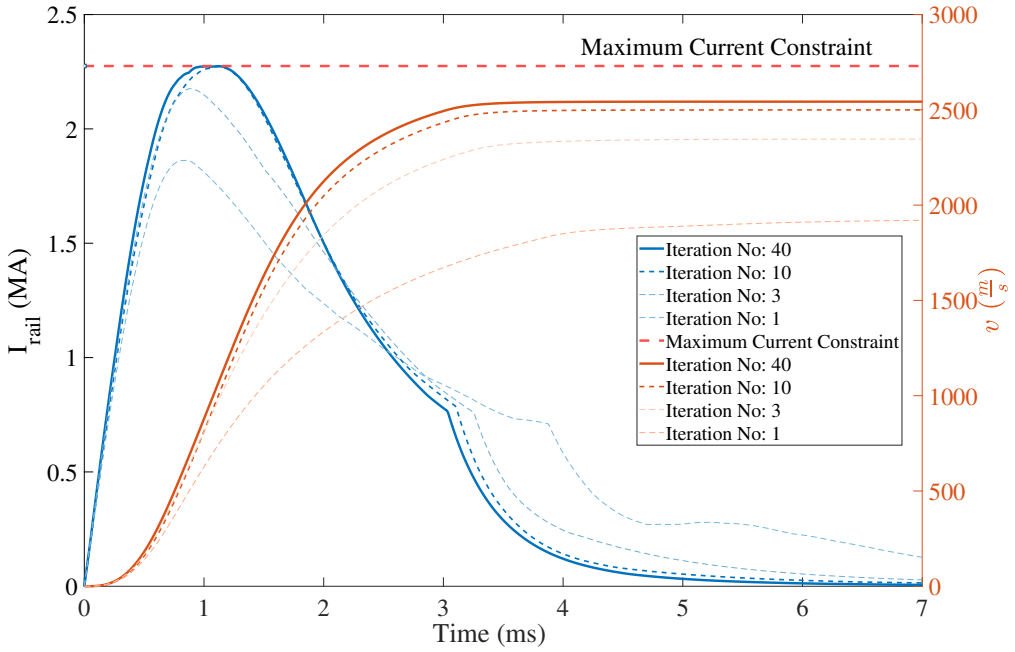

Figure 5.20: Initial intermediate and final steps of RCGA with constraint. The study showed that rail current becomes pulse current that have magnitude I_{max} to have maximum v_{exit} and maximum efficiency η.

5.5 Discussion

This study is conducted with the motivation of searching a triggering strategy under different EML objectives. Although the simulation model's accuracy is sought, the fundamental novelty of the study is the methodology of obtaining triggering times. The methodology can be applied to different 1-D simulation models as well as 3-D FEM simulations.

Hyper-parameter optimization of the benchmark methods (GA and PSO) is skipped. The main goal of adding these methods to the study is to give a figure of merit about the advantages of the iterative methods in TTOP. Moreover, the convergence of these methods gives insights about the behavior of triggering times when the maximum efficiency is targeted.

Although the down-slope transition is linked with I_{exit} between 80-90% of I_{ref} in the literature, there are some reported experiments with lower I_{exit} percentage no-

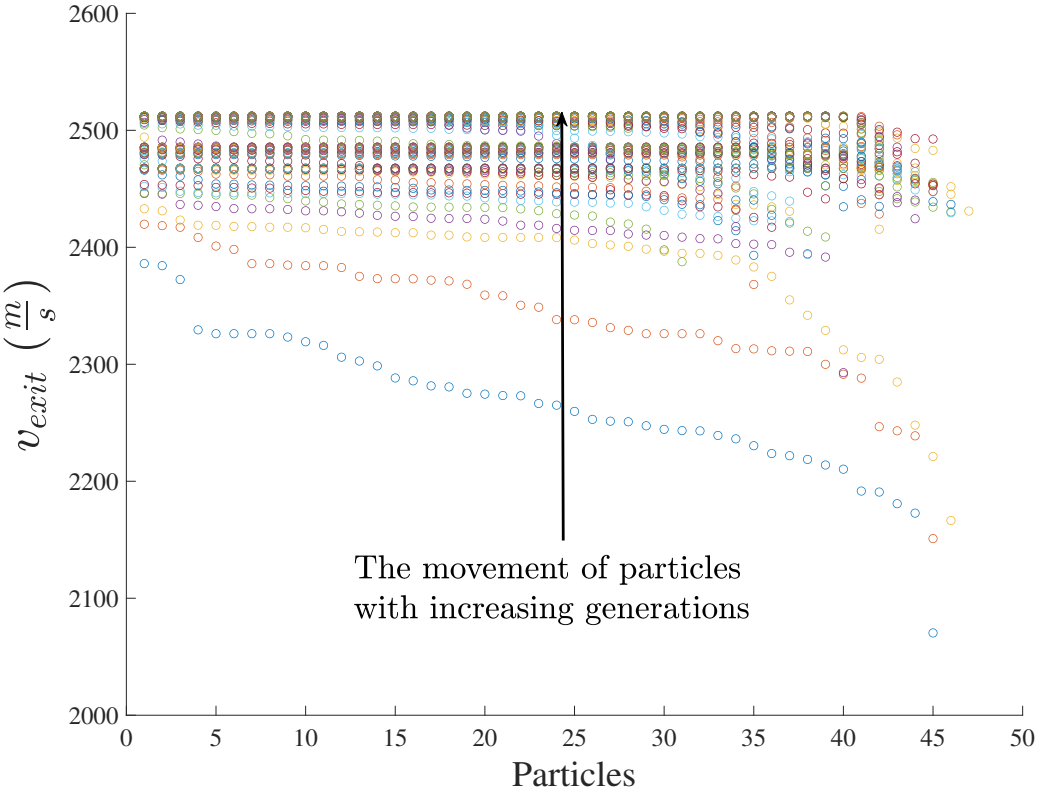

Figure 5.21: The result of Particle Swarm Optimization. The result are consistent with RCGA

transition [56]. Thus, in this study the constraint is settled a lower value 50%. However, this parameter can be re-adjusted considering the new I_{exit} constraint.

5.6 Conclusion

In this study TTOP solved by various algorithms such as RCGA, PSO and the proposed iterative method, MFTTA. In this study not only the comparison of iterative and evolutionary method but also the novelty of 1-D simulation model are introduced. The optimization results are used to show trade offs of different triggering strategies. These remarks are listed as following;

1. Without constraints, the triggering times at TTOP converge to zero vector which

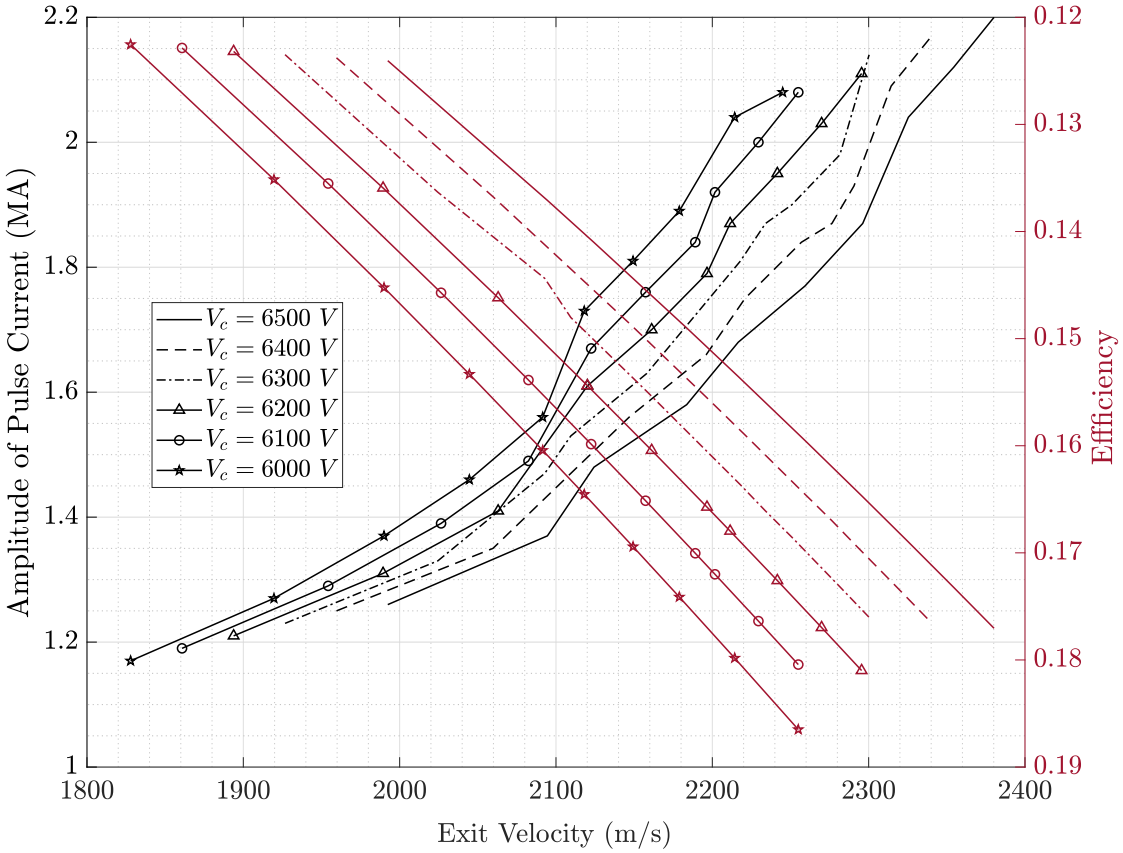

Figure 5.22: Variation of peak current and projectile to input power efficiency vs. projectile speed for different capacitor charge voltages.

indicates all PPS modules triggered at initial time step to have maximum v_{exit}. However, resulting rail current exceeds the maximum rail current limit which has harmful effect on the rails.

2. Considering the current constraints, the rail current converge to pulse shaped current which have magnitude I_{max} when the objective is v_{max}.

3. EAs are slower than iterative based algorithms for triggering time calculation of EML's. With increasing module number of PPS the performance of evolutionary algorithms become even worse due to necessity of increasing the number of individuals and generations. Iterative based computation is more robust to the increase in the module number.

4. The uniqueness of I_{ref} with the given exit velocity is valid if and only if the

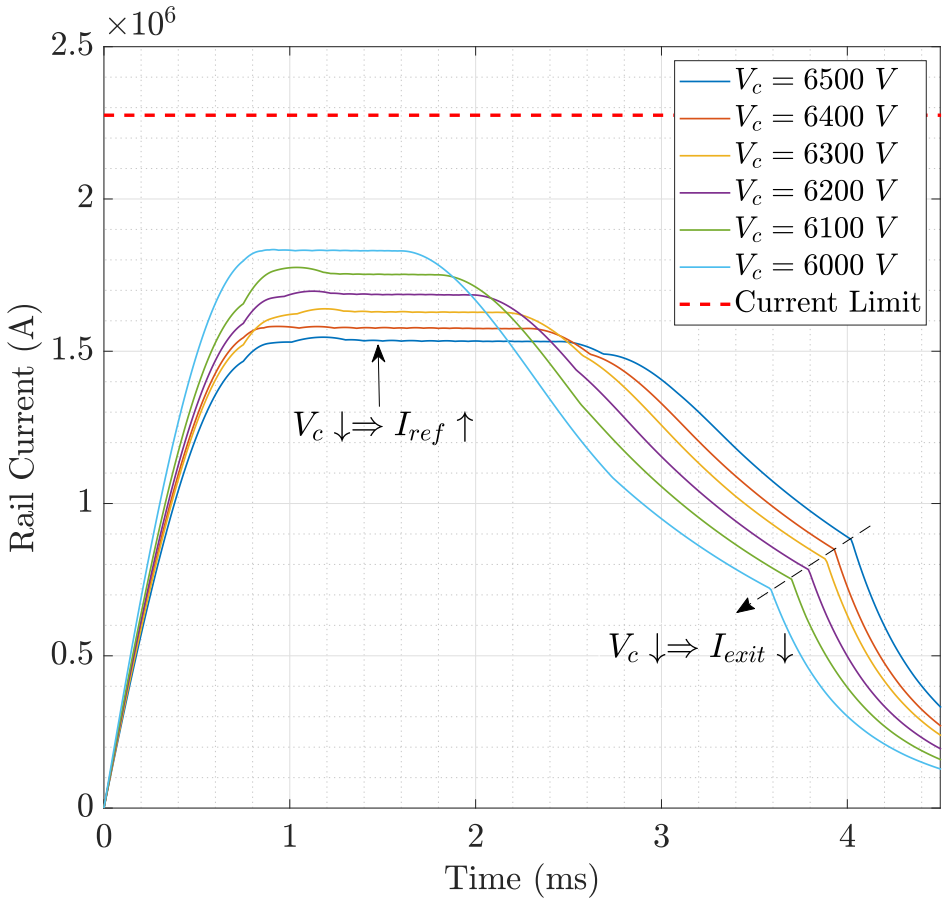

Figure 5.23: Various pulse currents with different capacitor voltages which satisfy desired exit velocity $\nu_{\text{exit}} = 2153\ \text{m/s}$. Decrease in capacitor voltage for fixed exit velocity leads to increase at pulse current magnitude I_{ref} and decrease in exit current I_{exit}. Efficiency increases when the capacitor voltage decreased however increase in I_{ref} and decrease in I_{exit} increase the risk of the transition. [48]

capacitor voltage and launch package mass are fixed. Therefore, there must an optimum I_{ref} that satisfies the desired launch package exit velocity and increases the overall system efficiency and satisfy other transition constraints.

5. For the same desired exit velocity, it is possible to generate multiple current pulse wave-forms as in Fig. 5.23. As the capacitor voltage decreases, the launch efficiency increases, the peak current increases and the exit current decreases. Increasing the peak and decreasing exit current result in transition between armature-rail interface. Therefore, a compromise has to be made during selection of launch triggering sequence and capacitor charge voltages.

CHAPTER 6

CONCLUSION

In this thesis, the aim is the developing more accurate with a reasonable computational burden. As the EML's electrical and mechanical ratings are astronomical regarding other electro-mechanical conversion devices, having precise models is critical. As the EMLs become larger and more powerful, several phenomena become more apparent. Thus, models should be more comprehensive.

Firstly, the modeling strategies and the governing equations are presented. Geometries are reduced, as the EML has a large aspect ratio and has symmetries. The rail portioning is often applied because the stationary armatures are used in the simulation. Analytical formulas are shared, to better understand the influence of EML's geometric parameters on the performance. The assumption and limitations of these models are declared clearly.

Secondly, the accuracy of the launch simulations are increased. To understand the limits of the 2-D assumption in VSE calculation, a 3-D alternative is presented. The Q-T strategy is validated in 2-D first. Then it applied in 3-D models to evaluate VSE resistance. The improved resistance calculation is used in 3-D Hybrid FEM model to show its effectiveness in launch experiments. It seems that the 2-D approximation overestimated VSE resistance up to %40, which influences calculations. The proposed model outperforms the control method, which utilizes a VSE resistance calculated with a 2-D assumption.

Furthermore, the EMF calculation should be revisited. Up to now, only the armature motion is kept responsible for the EMF generation. However, EMLs have large

conductors/rails. Thus, the diffusion process alters the rail current path, which eventually changes the inductance of the EML. To show its importance, a control method which only considers the armature motion for EMF generation is built. The proposed model compared with both the control method and empirical result. The new EMF formulation is more compatible with experimental results.

Lastly, a multi-level fast triggering time optimization algorithm is presented. The proposed algorithm significantly reduces the optimization space with an inner controller. As this controller also guarantees one of the constraints, it does not affect the optimization space. It programs the triggering times much more efficiently than any heuristic algorithm. The proposed algorithm promise a practical way to set the triggering times of the PPSs.

6.1 Summary of Contribution to Literature and Novelties

Contributions to literature and novelties of the proposed methods are explained with the following subsections.

6.1.1 VSE calculations

VSE resistance is calculated in two ways. The first is to use a 2-D assumption, which considers the field distribution in the rail is homogeneous across the rail height. However, this assumption is misleading; the current distribution differs. The second approach uses special FEM formulations, which require complex conditions, and commercial packages have no capability to utilize them. In this study, we proposed an alternative strategy, which is suitable for commercial FEM software. Resistance values are validated emprically.

6.1.2 Back-EMF calculations

In the literature, the armature movement is considered only source for an EMF generation. However, the rail current movement due to the diffusion process can also in-

duce an EMF. This phenomenon is more dominant, as the rail width to rail separation ratio becomes higher. Thus, the proposed model can evaluate inductance variation in the EML more accurately.

6.1.3 Triggering Time Optimization

In the literature, triggering times are determined with the heuristic algorithm as the optimization space has large dimensions and is non-linear. Thus, the optimization procedure is time-consuming and non-practical. However, an inner controller can significantly reduce the optimization space, as the triggering times can be programmable. Thus using a multi-level algorithm can accelerate the triggering time determination process. The study promises a practical tool to control PPS.

6.2 Practical Application Considerations

VSE resistances are calculated regarding EMFY-1 and EMFY-2 launchers' geometries. However, in the design procedure of a new launcher, this resistance should be evaluated for each design candidate. Thus the optimization time becomes astronomical. If the VSE resistance is formulated with EML parameters, the design procedure can be much faster.

Moreover, the VSE calculation assumes a rectangular prism armature geometry. Thus any attempt to decrease VSE with some novel armature geometry can not be investigated with 3-D Q-T strategy. The proposed method can not be utilized in an armature design.

6.3 Possible Improvements

VSE calculation with Q-T strategy is validated in 2-D; however, the same validation is not applied in 3-D. When the capabilities of the electromagnetic FEM package are increased, the Q-T strategy can be investigated further. Moreover, armatures can be more detailed to avoid VSE's unwanted effects.

Moreover, the proposed models discard eddy-brake caused by conductive containment. When continuous velocity measurements are obtained, this phenomenon can be investigated in more detail. This will increase the models' accuracy.

6.4 Comparison with Conventional Guns

An EML will launch a projectile at a speed of 2-3 kilometers per second. To give a perspective, the average 9mm pistol has a velocity of 300 m/s. The projectile of a .338 Lapua Magnum has a velocity of less than 300 m/s. The biggest difference between an EML and a conventional gun is the acceleration curve. EMLs have pulse shape acceleration curves regarding their rail current profile. However, conventional guns have spiky acceleration; after peak acceleration occurred, it decreases exponentially. As long as there is current excitation with sufficient rail length, the acceleration action is constant, which overcomes the bottleneck of the conventional system.

6.5 Future Works

EMFY-1 and EMFY-2 launchers have conductive containment. They are laminated to reduce eddy current losses due to the rail current's magnetic field. However, the lamination structure interferes with the armature's magnetic field, which eventually creates a drag mechanism. This acts like an eddy brake for the armature. Considering the EML geometry, an eddy break is inevitable. The brake's influence depends on the armature velocity as the magnetic field deviation becomes more sudden for lamination plates.

The proposed model should take into account this brake mechanism. However, there is no experimentally verified model in the literature. Continuously velocity measurement is essential to investigate the phenomenon. The brake is velocity-dependent. Nevertheless, EMFY-1 and EMFY-2 launch experiments did not have in-bore velocity measurements; only muzzle velocity is available. In EMFY-3 experiments, a doppler radar is utilized to measure, but the EMFY-3 launcher has non-conductive containment. Thus it has no eddy brake.

However, in the near future EMFY-4 launcher, which has a laminated-conductive containment, will be built by ASELSAN Inc. Utilizing the doppler radar for velocity measurements, the effect of the eddy-brake can be evaluated. These experiments have the potential to verify lamination-included models.

In Chapter 5, the proposed triggering-time determination algorithm can be used as a velocity controller. In ballistic usage, the velocity of the projectile is critical. Any possible muzzle velocity error should be avoided. As the algorithm can be used as a triggering-time controller which aims to ensure the determined muzzle velocity, the algorithm can be embedded to PPS controllers. This is beneficial in the practical usage of the EML. Furthermore, the hysteresis controller can be implemented directly to the PPS controller, even if the muzzle velocity control is not targeted. Pulse current construction is necessary in any case, and the algorithm is suitable as the rail current is continuously measured.

REFERENCES

[1] M. Karagoz, Y. Çevik, E. Tan, A. Civil, O. Cavbozar, U. Gocmen, B. Yildirim, E. Durna, and M.S. Sahin. Aselsan emfy-1 electromagnetic launcher: First experiments. In *2017 IEEE 21st International Conference on Pulsed Power (PPC)*, pages 1–3, 2017.

[2] Fantast. Railgun predecessors. (19-Aug-2021).

[3] I. R. McNab. Early electric gun research. *IEEE Transactions on Magnetics*, 35(1):250–261, 1999.

[4] I. R. McNab. Launch to space with an electromagnetic railgun. *IEEE Transactions on Magnetics*, 39(1):295–304, 2003.

[5] D. Wetz, F. Stefani, D. Motes, J. Parker, and I. McNab. Development of a plasma railgun for affordable and rapid access to space. In *2007 IEEE 34th International Conference on Plasma Science (ICOPS)*, pages 1015–1015, 2007.

[6] F. Stefani, I. R. McNab, J. V. Parker, M. Alonzo, and T. Klatt. A plasma railgun experiment addressing launch-to-space issues. *IEEE Transactions on Magnetics*, 43(1):194–197, 2007.

[7] P. Lehmann, B. Reck, M. D. Vo, and J. Behrens. Acceleration of a suborbital payload using an electromagnetic railgun. *IEEE Transactions on Magnetics*, 43(1):480–485, 2007.

[8] Hong bin Xie, Hui ya Yang, Jian Yu, Ming yu Gao, Jian dong Shou, You tong Fang, Jia bin Liu, and Hong tao Wang. Research progress on advanced rail materials for electromagnetic railgun technology. *Defence Technology*, 17(2):429–439, 2021.

[9] Shoubao Liu, Jiangjun Ruan, Zhiye Du, Dong Wang, and Chun Zhao. Calculation of railgun inductance gradient by 2-d finite element method. In *2008 International Conference on Electrical Machines and Systems*, pages 4057–4060, 2008.

[10] I. R. McNab. Brief history of the eml symposia: 19802018. *IEEE Transactions on Plasma Science*, 47(5):2136–2142, 2019.

[11] A. Egeland. Birkeland's electromagnetic gun: a historical review. *IEEE Transactions on Plasma Science*, 17(2):73–82, 1989.

[12] C. Gong, X. Yu, and X. Liu. Study on the system efficiency of the capacitive pulsed-power supply. *IEEE Transactions on Plasma Science*, 43(5):1441–1447, May 2015.

[13] JF Kerrisk. Current distribution and inductance calculations for rail-gun conductors. 1981.

[14] J. V. Parker and S. Levinson. Loss of propulsive force in railguns with laminated containment. *IEEE Transactions on Magnetics*, 35(1):442–446, 1999.

[15] J. Kerrisk. Electrical and thermal modeling of railguns. *IEEE Transactions on Magnetics*, 20(2):399–402, 1984.

[16] J. Nie, J. Han, Q. Jiao, J. Li, and J. Qin. An analytic expression of inductance gradient for rail-type electromagnetic launcher. *IEEE Transactions on Plasma Science*, 39(3):931–934, 2011.

[17] Frederick W Grover. *Inductance calculations: working formulas and tables*. Courier Corporation, 2004.

[18] Jad H Batteh. Momentum equation for arc-driven rail guns. *Journal of applied physics*, 56(11):3182–3186, 1984.

[19] A. Keshtkar, S. Mozaffari, and A. Keshtkar. Inductance gradient variation with time and armature sliding along the rails. *IEEE Transactions on Plasma Science*, 39(1):75–79, 2011.

[20] S. An, B. Lee, Y. Bae, Y. Lee, and S. Kim. Numerical analysis of the transient inductance gradient of electromagnetic launcher using 2-d and 3-d finite-element methods. *IEEE Transactions on Plasma Science*, 45(7):1635–1638, 2017.

[21] N. Tosun, H. Polat, D. Ceylan, M. Karagoz, B. Yldrm, . Güngen, and O. Keysan. A hybrid simulation model for electromagnetic launchers including the transient inductance and electromotive force. *IEEE Transactions on Plasma Science*, 48(9):3220–3228, 2020.

[22] Y. Lou, G. Wan, Y. Jin, B. Tang, and B. Li. Research on energy loss distribution of an augmented railgun. *IEEE Transactions on Plasma Science*, 44(5):857–861, 2016.

[23] J. Wu, G. Wan, N. Cheng, L. Li, and B. Li. Research on armatures wearing and dynamic interior ballistic of a railgun. *IEEE Transactions on Plasma Science*, 45(7):1202–1207, 2017.

[24] J. V. Parker and S. Levinson. Loss of propulsive force in railguns with laminated containment. *IEEE Transactions on Magnetics*, 35(1):442–446, 1999.

[25] J. Mallick. Phenomenological electromagnetic modeling of laminated-containment launchers. *IEEE Transactions on Magnetics*, 43(1):359–363, 2007.

[26] J. Kerrisk. Electrical and thermal modeling of railguns. *IEEE Transactions on Magnetics*, 20(2):399–402, 1984.

[27] T. G. Engel, J. M. Neri, and M. J. Veracka. Characterization of the velocity skin effect in the surface layer of a railgun sliding contact. *IEEE Transactions on Magnetics*, 44(7):1837–1844, July 2008.

[28] T. G. Engel, J. M. Neri, and M. J. Veracka. The velocity and efficiency limiting effects of magnetic diffusion in railgun sliding contacts. In *2008 14th Symposium on Electromagnetic Launch Technology*, pages 1–5, June 2008.

[29] K. . Hsieh, F. Stefani, and S. J. Levinson. Numerical modeling of the velocity skin effects: an investigation of issues affecting accuracy [in railguns]. *IEEE Transactions on Magnetics*, 37(1):416–420, 2001.

[30] S. Tan, J. Lu, B. Li, Y. Zhang, and Y. Jiang. A new finite-element method to deal with motion problem of electromagnetic rail launcher. *IEEE Transactions on Plasma Science*, 45(7):1374–1379, 2017.

[31] K. Hsieh. A lagrangian formulation for mechanically, thermally coupled electromagnetic diffusive processes with moving conductors. *IEEE Transactions on Magnetics*, 31(1):604–609, Jan 1995.

[32] S. An, B. Lee, Y. Bae, Y. Lee, and S. Kim. Numerical analysis of the transient inductance gradient of electromagnetic launcher using 2-d and 3-d finite-element methods. *IEEE Transactions on Plasma Science*, 45(7):1635–1638, July 2017.

[33] S. An, B. Lee, Y. Bae, Y. Lee, and S. Kim. Numerical analysis on the transient inductance gradient of the resistive overlay rail on the sliding electrical contact. *IEEE Transactions on Plasma Science*, 47(5):2339–2342, 2019.

[34] O. Liebfried, M. Schneider, T. Stankevi, S. Baleviius, and N. urauskien. Velocity-induced current profiles inside the rails of an electric launcher. *IEEE Transactions on Plasma Science*, 41(5):1520–1525, May 2013.

[35] T. Stankevi, M. Schneider, and S. Baleviius. Magnetic diffusion inside the rails of an electromagnetic launcher: Experimental and numerical studies. *IEEE Transactions on Plasma Science*, 41(10):2790–2795, Oct 2013.

[36] S. Hundertmark and M. Roch. Transient 3-d simulation of an experimental railgun using finite element methods. In *2012 16th International Symposium on Electromagnetic Launch Technology*, pages 1–5, 2012.

[37] D. Ceylan, M. Karagöz, Y. Çevik, B. Yldrm, H. Polat, and O. Keysan. Simulations and experiments of emfy-1 electromagnetic launcher. *IEEE Transactions on Plasma Science*, 47(7):3336–3343, July 2019.

[38] M. Karagoz, A. Civil, B. Yildirim, E. B. Yurdakul, E. Durna, E. Tan, O. Cavbozar, U. Gocmen, and Y. Cevik. Aselsan electromagnetic launch laboratory: First shot. *IEEE Trans. Plasma Sci.*, pages 1–6, 2020.

[39] A. J. Ma, B. D. Zhang, C. W. Yuan, R. Yuan, W. Xu, and P. Yan. A method of generating timing for a given target current waveform in electromagnetic launch technology. *IEEE Transactions on Plasma Science*, 45(7):1561–1566, 2017.

[40] S. F. Glover, F. E. White, K. W. Reed, and M. J. Harden. Genetic optimization for pulsed-power system configuration. *IEEE Transactions on Plasma Science*, 37(2):339–346, 2009.

[41] X. Chang, X. Yu, X. Liu, and Z. Li. Armature velocity control strategy and system efficiency optimization of railguns. *IEEE Transactions on Plasma Science*, 46(10):3634–3639, 2018.

[42] S. Zhengjun and Y. Xinjie. Two-objective optimization design for pulsed power supply. *IEEE Transactions on Magnetics*, 45(1):525–530, 2009.

[43] X. Yu and Z. Fan. Simulation and two-objective optimization of the electromagnetic-railgun model considering vsec resistance and contact resistance. *IEEE Transactions on Plasma Science*, 39(1):405–410, 2011.

[44] H. Zhang, G. Cheng, W. Guo, Z. Su, T. Zhang, and Y. Yang. Calculating timing sequence of capacitor-based railgun with given muzzle velocity. *IEEE Transactions on Plasma Science*, 43(9):3298–3303, 2015.

[45] H. Zhang, G. Cheng, W. Guo, Z. Su, and T. Zhang. A lumped parameter model and its code for capacitor-based railgun with arbitrary number of pfus. *IEEE Transactions on Plasma Science*, 42(8):2098–2103, 2014.

[46] J. P. Barber, D. P. Bauer, K. Jamison, J. V. Parker, F. Stefani, and A. Zielinski. A survey of armature transition mechanisms. *IEEE Transactions on Magnetics*, 39(1):47–51, 2003.

[47] Z. Wang, L. Chen, S. Xia, and C. Li. Experiments and analysis of downslope low-voltage transition in c-type solid armature rail gun. *IEEE Transactions on Plasma Science*, 48(7):2601–2607, 2020.

[48] S. Satapathy and H. Vanicek. Down-slope contact transition in railguns. *IEEE Transactions on Magnetics*, 43(1):402–407, 2007.

[49] T. Chao, Y. Yan, P. Ma, M. Yang, and Y. W. Hu. Optimization of electromagnetic railgun based on orthogonal design method and harmony search algorithm. *IEEE Trans. Plasma Sci.*, 43(5):1546–1554, May 2015.

[50] H. Zhang, G. Cheng, W. Guo, Z. Su, T. Zhang, and Y. Yang. Calculating timing sequence of capacitor-based railgun with given muzzle velocity. *IEEE Trans. Plasma Sci.*, 43(9):3298–3303, Sep. 2015.

[51] Xinyue Chang, Xinjie Yu, Xukun Liu, and Zhen Li. Armature Velocity Control Strategy and System Efficiency Optimization of Railguns. *IEEE Trans. Plasma Sci.*, 46(10):3634–3639, 2018.

[52] Shi Zhengjun and Yu Xinjie. Two-objective optimization design for pulsed power supply. *IEEE Trans. Magn.*, 45(1):525–530, 2009.

[53] X. Yu and Z. Fan. Simulation and two-objective optimization of the electromagnetic-railgun model considering vsec resistance and contact resistance. *IEEE Trans. Plasma Sci.*, 39(1):405–410, Jan 2011.

[54] A. J. Ma, B. D. Zhang, C. W. Yuan, R. Yuan, W. Xu, and P. Yan. A method of generating timing for a given target current waveform in electromagnetic launch technology. *IEEE Trans. Plasma Sci.*, 45(7):1561–1566, July 2017.

[55] Doga Ceylan, Mustafa Karagoz, Yasin Cevik, Baran Yildirim, Hakan Polat, and Ozan Keysan. Simulations and Experiments of EMFY-1 Electromagnetic Launcher. *IEEE Trans. Plasma Sci.*, 47(7):3336–3343, 2019.

[56] N. Tosun, H. Polat, D. Ceylan, M. Karagoz, B. Yldrm, . Güngen, and O. Keysan. A hybrid simulation model for electromagnetic launchers including the transient inductance and electromotive force. *IEEE Transactions on Plasma Science*, 48(9):3220–3228, 2020.

[57] Edwin Kah Pin Chong and Stanislaw H. Zak. *An introduction to optimization*. Wiley-Interscience series in discrete mathematics and optimization. Wiley, New York, 2nd ed edition, 2001.